Interfacial and Transport Properties of Nanoconstrained Inorganic and Organic Materials

Lakshmi Suhasini Kocherlakota

A dissertation submitted in partial fulfillment of the
requirements for the degree of

Doctor of Philosophy

University of Washington
2013

Reading Committee:
René M. Overney, Chair
John C. Berg
Shaoyi Jiang

Program Authorized to Offer Degree:
Department of Chemical Engineering

University of Washington

Abstract

Interfacial and Transport Properties of Nanoconstrained Inorganic and Organic Materials

Lakshmi Suhasini Kocherlakota

Chair of the Supervisory Committee:
Professor René M. Overney
Department of Chemical Engineering

Nanoscale constraints impact the material properties of both organic and inorganic systems. The systems specifically studied here are (i) nanoconstrained polymeric systems, poly(l-trimethylsilyl-1-propyne) (PTMSP) and poly(ethylene oxide) (PEO) relevant to gas separation membranes (ii) Zwitterionic polymers poly(sulfobetaine methacrylate)(pSBMA), poly(carboxybetaine acrylamide) (pCBAA), and poly(oligo(ethylene glycol) methyl methacrylate) (PEGMA) brushes critical for reducing bio-fouling (iii) Surface properties of N-layer graphene sheets. Interfacial constraints in ultrathin poly(l-trimethylsilyl-1-propyne) (PTMSP) membranes yielded gas permeabilities and CO_2/helium selectivities that exceed bulk PTMSP membrane transport properties by up to three-fold for membranes of submicrometer thickness. Indicative of a free volume increase, a molecular energetic mobility analysis (involving intrinsic friction analysis) revealed enhanced methyl side group mobilities in thin PTMSP membranes with maximum permeation, compared to bulk films. Aging studies conducted over the timescales relevant to the conducted experiments signify that the free volume states in the thin film membranes are highly unstable in the presence of sorbing gases such as CO_2. To maintain this high free volume configuration of polymer while improving the temporal stability an “inverse” architecture to conventional polymer nanocomposites was investigated, in which the polymer phase of PTMSP and PEO were interfacially and dimensionally constrained in nanoporous anodic aluminum oxide (AAO)

membranes. While with this architecture the benefits of nanocomposite and ultrathin film membranes of PTMSP could be reproduced and improved upon, also the temporal stability could be enhanced substantially. The PEO-AAO nanocomposite membranes also revealed improved gas selectivity properties of CO_2 over helium. In the thermal transition studies of zwitterionic pSBMA brushes a reversible critical transition temperature of 60 ^{o}C in 27 nm films was evidenced, indicating changes in molecular conformations with respect to the temperature. pCBAA and pEGMA brushes displayed no thermal transitions, suggesting that the molecular conformations of these systems were insensitive to temperature in the investigated regime. The surface energy of a dimensionally constrained inorganic system, graphene is studied via local Hamaker constant determination from a single graphene layer to bulk graphite. Intrinsic friction scattering analysis of dipolar fluctuations of the Van der Waals interactions between an atomic force microscopy tip and graphene layers revealed a four-fold reduction in the surface energy from bulk HOPG to graphene. A numerical analysis based on electron energy loss spectroscopy confirms quantitatively the results.

Table of Contents

List of Figures

List of Tables

Acknowledgements

It is with immense gratitude that I acknowledge the support and guidance of my advisor Prof. René M. Overney. I am deeply indebted to him for believing in me and giving me an opportunity to pursue research in his group. His enthusiastic guidance in every aspect of my research enriched me both academically and professionally. He inculcated critical thinking and taught me how to be an independent researcher.

I would like to thank Prof.Shaoyi Jiang for his support and guidance in studies related to zwitterionic polymeric systems. For this dissertation, I would like to express gratitude to my committee members, Prof. John Berg, Prof. Shaoyi Jiang and Prof. Champak Chatterjee for their time, interest, and helpful comments. I am also thankful to Prof.Vipin Kumar for giving me an opportunity to work on development of nanocellular foaming materials. My special regards to Prof. K. S. Gandhi at Indian Institute of Science, whose unparalleled passion for research and guidance motivated me in pursuing research.

I would also like to thank all my fellow students and friends who have helped me in various phases of my research. I would particularly wish to thank Dan Knorr, Jason Killgore, Tiep Pham, Brad Krajina, Monica Ospinal, Hsiang-Chieh Hung and Harihara S Sundaram.

I cannot find words to express my gratitude to my husband Prasanth Saraswatula for his infallible love and support. This thesis would have been impossible without his selfless support and patience. I owe my deepest gratitude to my parents, Mrs. Krishna Kumari, Mr. Subba Rao Kocherlakota and my dear brother Sashi Kanth Kocherlakota for their unconditional love, affection and motivation. I would not have accomplished anything without their continual care and motivation. I would also like to thank my parents in law, Mrs. Lalitha Devi and Dr.S.K.Rao for their moral support and encouragement. Finally I thank God for blessing me with my son Pranav Srinivas whose heavenly smiles add a magical touch and pleasure to my life.

Dedication

For my parents who always stood by me selflessly with all their love and affection.

Chapter 1

Introduction

Interfacial and Transport Properties of Nanoconstrained Inorganic and Organic Materials

Dimensional and interfacial constraints have been found to significantly impact material and transport properties of both organic and inorganic systems. Novel electronic and optical properties are observed in semiconductor nanostructures like quantum dots, nanowires and nanotubes owing to their unique structural dimensionality and quantum confinement effects which find applications in the fabrication of contemporary electronic devices.[1-3] For instance large enhancements in quantum efficiencies were reported in ZnS nanocrystals doped with Mn, as the particle size reduced below 5 nm.[4] Similarly a systematic blue shift from 900 nm to 800 nm in the photoluminescence emission of InP nanowires was observed as the diameter was reduced from 60 nm down to 10 nm.[5,6] Quantum confinement effects on the electronic transport properties have also been observed in interfacially confined polymeric semiconductors below a critical film thickness. The photoconductivity of the optoelectronic assembly based on polyquinolines, well known n-type electron transporting polymers were found to be dependent of the film thickness of the polymers in the critical thickness regime of 25-60 nm.[7]

The exotic properties of nanostructures arise because of their large surface to volume ratio and hence understanding and controlling their surfaces is critical for their applications. Surface reconstruction, a process by which the atoms of the surface attain a structural arrangement different from the bulk, is shown to be responsible for large optical band gap reductions in semiconductor nanocrystals which ensues because of the unbalanced interatomic forces experienced by the surface/interfacial atoms.[8] Unlike the fluid-fluid interfaces, the solid-fluid interfaces are characterized by 'surface stresses' (f_{ij}) which differ from the surface free energy (σ) and is given as follows[9,10] for isotropic cases:

$$f = \sigma + A\frac{d\sigma}{dA} \qquad 1.1$$

In a general frame work:

$$f_{ij} = \delta_{ij}\sigma + \frac{\partial\sigma}{\partial e_{ij}} \qquad 1.2$$

Where δ_{ij} is the Kroniker delta, A is the surface area and e_{ij} is the strain.[9,10] While there are varied reports on the dependence of surface energy of metallic nanoparticles like Ag with particle size[11], major consensus is that the surface energy of nanoclusters is decreasing with decreasing particle size.[12,13] The critical diameter at which bulk-deviations occur in Ag nanoparticles is ~ 1nm. The silver nanoparticles experience a surface stress which depends on the hydrostatic pressure as shown below for a spherical particle:[10]

$$f_{rr} = -\frac{3}{2}\frac{\Delta a}{a}\frac{r}{\kappa} \qquad 1.3$$

Where a is the lattice constant, Δa is the change in the lattice constant, r is the particle radius, κ is the compressibility factor. Similar to the surface energy of nanoconstrained Ag particles, the surface energy of the graphene sheets, the atomic lamellar sheets of graphite, was found to decrease going from bulk graphite to single layer graphene.[14] As discussed further in Chapter 5, this could be attributed to the fact that since graphite is an atomically layered structure, the surface atoms are less disturbed in comparison to surface atoms in nanoclusters/nanospheres. Graphene, one of the allotropes of elemental carbon, is a planar monolayer of carbon atoms arranged into a two dimensional (2D) honeycomb lattice and exhibits intriguing mechanical, thermal and electronic properties.[15] Owing to its exotic structural and electronic properties it is being pursued as composites, in electrodes, transparent coatings, and in other lamellar designs where the surface properties of graphene are of critical importance.[16-18] The surface properties of graphene, such as wettability, hydrophilicity and surface charge, are critical in determining its device performance.[19]

While inorganic materials such as ceramics, metals, oxides exhibit size limitations below 10 nm, interfacial effects in polymers are found to be relatively far reaching over several hundreds of nanometers. Deviations in glass transition properties[20-22], relaxations[23,24] and gas transport properties[25-27] have been reported in polymers subjected to dimensional and interfacial constraints. Specifically polymeric systems relevant to gas transport membranes (Chapter 2&3) and non-fouling zwitterionic coating applications (Chapter 4) are studied in this research project.

Polymeric membranes have been extensively studied for gas separation applications as they involve relatively lower capital and operation costs, possess excellent processibility and ease of operation in comparison to their inorganic counterparts like zeolites and porous carbon sieves.[28,29] The economic feasibility of using a given polymeric membrane is primarily evaluated by its gas permeability coefficient (P_A) and selectivity ($\alpha_{A/B}$). An increase in permeability amounts to a smaller membrane area, and thus, a decrease in operational cost. Higher selectivity results in value added higher purity gas products. Unfortunately, a rather general tradeoff relationship between P_A and $\alpha_{A/B}$ has been recognized for neat polymeric membranes that results in a reduction of the selectivity with increasing permeability. This is illustrated with the "Robeson Plot" in Figure 1.1 for CO_2/N_2 separation. Robeson compiled an exhaustive amount of literature data involving many polymer membranes for a variety of permeation species, and found the membranes to be transport limited, as indicated by the solid lines of Figure 1.1.[30] The transport limitation in neat polymeric membrane systems has been shown to be circumvented with appropriate hybrid polymer composites consisting of dispersed inorganic phases, in which interfacial constraints were shown to push the selectivity and permeability beyond the Robeson line into the attractive region of higher selectivity (Figure 1.1).[31]

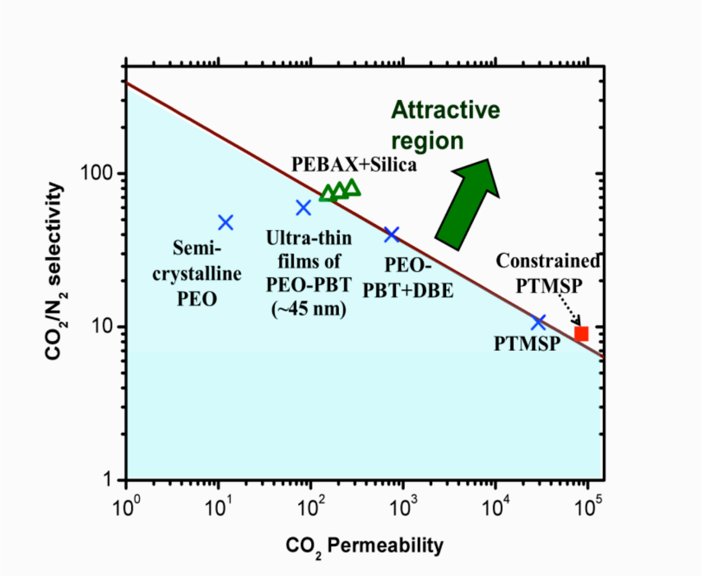

Figure 1.1: Robeson plot of CO_2 permeability and CO_2/N_2 selectivity. Robeson's upper bound line is given by $P_{CO2}=k\alpha_{ij}^{n}$, with the CO_2 permeability P_{CO2}, the α_{ij} selectivity and the fitting constants $k \approx 3.1\times10^{7}$, $n \approx -2.9$ pertinent to CO_2/N_2 separation

In our most recent study, which is discussed in greater detail in Chapter 2 for CO_2/helium separation[32], and CO_2/N_2 separation[33] (Chapter 3), the transport properties for interfacially constrained poly[l-(trimethylsily1)-1-propyne] (PTMSP) membranes could be pushed into the attractive region of the Robeson plot, Figure 1.1.

Novel membranes that involve interfaces (also referred to as mixed matrix membranes) have emerged as an attractive route to enhance the transport properties of polymeric properties.[34] Freeman and Merkel incorporated nonporous fumed silica (FS) nanoparticle filler with trimethylsilyl surface groups into poly(4-methyl-2-pentyne) (PMP)[34], poly[l-(trimethylsily1)-1-

propyne] (PTMSP)[27], which resulted in a remarkable enhancement in gas permeability with increasing FS loading. Polyacytelene based polymers, such as PMP, PTMSP and their analogues[35-38] are microporous, ultra-high free volume, glassy polymers which exhibit very high gas permeabilities. Furthermore, these polymers also exhibit preferential selectivity to large organic vapors over smaller, permanent gases, often termed "reverse selective" membranes. Owing to its extremely high permeabilities, PTMSP exhibits transport properties close to the upper bound performance (Figure 1.1). Another polymeric membrane system which has garnered attention for the CO_2/N_2 separation is poly(ethylene oxide) PEO. Recently extremely high CO_2 permeances were reported in poly(ethylene oxide)-poly(butylene terephthalate) (PEO-PBT) copolymeric systems which were found to increase with a decrease in film thickness.[39]

Surface resistance to non-specific protein adsorption and cell adhesion is critical for the performance of many systems, such as medical implants, marine coatings and drug delivery carriers.[40-42] Zwitterionic polymeric brushes are shown to be extremely effective in inhibiting biofouling by surface hydration mechanism creating a physical and energetic barrier for biomolecular adsorption/adhesion.[40,41,43-45] Interfacial and dimensionally constrained systems such as ultra-thin films and densely packed zwitterionic brushes are shown to exhibit improved anti-fouling properties.[45-47]

Common to all these observations made above for both polymeric and inorganic systems involve nanoconstraints which improve/alter the material properties. Hence it can be seen that elucidation of how exactly the interfaces affect the observed material properties is extremely relevant for the rational design of novel organic and inorganic systems. So the present research work seeks to: (i) establish a fundamental understanding of the origin responsible for the enhancement of transport properties in the interfacial region of confined polymers that have been shown to impact global transport properties of nanocomposites (Chapter 2), and (ii) make the interfacial region the dominant phase by incorporating the polymers into porous systems (inverse nanocomposites), and thus, generate stable "bulk" polymeric hybrid membrane systems (Chapter 3) (iii) investigate the inter/intra-molecular association states of zwitterionic polymers through thermal transition studies (Chapter 4) (iv) determine the surface energy of graphene layers (Chapter 5). Along these lines, the experimental techniques that were used and have been developed for probing the material properties are described in Chapter 6. Finally the conclusions of this work and the future outlook are presented in Chapter 7.

References

(1) Reimann, S. M.; Manninen, M. *Reviews of Modern Physics* **2002**, *74*, 1283-1342.

(2) Law, M.; Goldberger, J.; Yang, P. D. *Annual Review of Materials Research* **2004**, *34*, 83-122.

(3) Smith, A. M.; Nie, S. M. *Accounts of Chemical Research* **2010**, *43*, 190-200.

(4) Bhargava, R. N.; Gallagher, D.; Hong, X.; Nurmikko, A. *Physical Review Letters* **1994**, *72*, 416-419.

(5) Gudiksen, M. S.; Wang, J. F.; Lieber, C. M. *Journal of Physical Chemistry B* **2002**, *106*, 4036-4039.

(6) Yu, H.; Li, J. B.; Loomis, R. A.; Wang, L. W.; Buhro, W. E. *Nature Materials* **2003**, *2*, 517-520.

(7) Zhang, X. J.; Shetty, A. S.; Jenekhe, S. A. *Macromolecules* **1999**, *32*, 7422-7429.

(8) Puzder, A.; Williamson, A. J.; Reboredo, F. A.; Galli, G. *Physical Review Letters* **2003**, *91*.

(9) Shuttleworth, R. *Proceedings of the Physical Society of London Section A* **1950**, *63*, 444-457.

(10) Vermaak, J. S.; Mays, C. W.; Kuhlmann.D *Surface Science* **1968**, *12*, 128-&.

(11) Medasani, B.; Park, Y. H.; Vasiliev, I. *Physical Review B* **2007**, *75*.

(12) Q. Jiang, L. H. L., and D. S. Zhao *The Journal of Physical Chemistry B* **2001**, *105*, 6275-6277.

(13) D.Liu, Z. W., Q.Jiang *Current Nanoscience* **2011**, *7*, 463-470.

(14) Lakshmi S. Kocherlakota, B. A. K., and René M. Overney *Advanced Materials Interfaces* **(Submitted)**.

(15) Singh, V.; Joung, D.; Zhai, L.; Das, S.; Khondaker, S. I.; Seal, S. *Progress in Materials Science* **2011**, *56*, 1178-1271.

(16) Kim, H.; Abdala, A. A.; Macosko, C. W. *Macromolecules* **2010**, *43*, 6515-6530.

(17) Ramanathan, T.; Abdala, A. A.; Stankovich, S.; Dikin, D. A.; Herrera-Alonso, M.; Piner, R. D.; Adamson, D. H.; Schniepp, H. C.; Chen, X.; Ruoff, R. S.;

Nguyen, S. T.; Aksay, I. A.; Prud'Homme, R. K.; Brinson, L. C. *Nature Nanotechnology* **2008**, *327-331*.
(18) Zhang, X.; Wan, S.; Pu, J.; Wang, L.; Liu, X. *J. Mater. Chem.* **2011**, *21*, 12251-12258.
(19) Jia, B.; Zou, L. *Chemical Physics Letters* **2012**, *548*, 23-28.
(20) Forrest, J. A.; Dalnoki-Veress, K. *Advances in Colloid and Interface Science* **2001**, *94*, 167-196.
(21) Keddie, J. L.; Jones, R. A. L.; Cory, R. A. *Europhysics Letters* **1994**, *27*, 59-64.
(22) Sills, S.; Overney, R. M.; Chau, W.; Lee, V. Y.; Miller, R. D.; Frommer, J. *J. Chem. Phys.* **2004**, *120*, 5334-5338.
(23) Huang, Y.; Paul, D. R. *Polymer* **2004**, *45*, 8377-8393.
(24) Rowe, B. W.; Freeman, B. D.; Paul, D. R. *Polymer* **2009**, *50*, 5565-5575.
(25) Killgore, J. P.; Kocherlakota, L. S.; Overney, R. M. *Journal of Polymer Science Part B-Polymer Physics* **2010**, *48*, 434-441.
(26) De Sitter, K.; Andersson, A.; D'Haen, J.; Leysen, R.; Mullens, S.; Maurer, F. H. J.; Vankelecom, I. F. J. *Journal of Membrane Science* **2008**, *321*, 284-292.
(27) Merkel, T. C.; He, Z. J.; Pinnau, I.; Freeman, B. D.; Meakin, P.; Hill, A. J. *Macromolecules* **2003**, *36*, 6844-6855.
(28) Baker, R. W. *Industrial & Engineering Chemistry Research* **2002**, *41*, 1393-1411.
(29) Bernardo, P.; Drioli, E.; Golemme, G. *Industrial & Engineering Chemistry Research* **2009**, *48*, 4638-4663.
(30) Robeson, L. M. *Journal of Membrane Science* **2008**, *320*, 390-400.
(31) Kim, J. H.; Ha, S. Y.; Lee, Y. M. *Journal of Membrane Science* **2001**, *190*, 179-193.
(32) Kocherlakota, L. S.; Knorr, D. B., Jr.; Foster, L.; Overney, R. M. *Polymer* **2012**, *53*, 2394-2401.
(33) Lakshmi S. Kocherlakota, T. P., René M. Overney *Polymer* **2013**, *54*, 5986-5992.
(34) Merkel, T. C.; Freeman, B. D.; Spontak, R. J.; He, Z.; Pinnau, I.; Meakin, P.; Hill, A. J.; *Science* **2002**, *296*, 519-522.
(35) Morisato, A.; Shen, H. C.; Sankar, S. S.; Freeman, B. D.; Pinnau, I.; Casillas, C. G. *Journal of Polymer Science Part B-Polymer Physics* **1996**, *34*, 2209-2222.
(36) Masuda, T.; Isobe, E.; Higashimura, T.; Takada, K. *Journal of the American Chemical Society* **1983**, *105*, 7473-7474.
(37) Pinnau, I.; Toy, L. G. *Journal of Membrane Science* **1996**, *116*, 199-209.
(38) Freeman, B.; Pinnau, I. *Trends in Polymer Science* **1997**, *5*, 167-173.
(39) Yave, W.; Car, A.; Wind, J.; Peinemann, K. V. *Nanotechnology* **2010**, *21*.
(40) Chen, S.; Jiang, S. *Advanced Materials* **2008**, *20*, 335-+.
(41) Jiang, S.; Cao, Z. *Advanced Materials* **2010**, *22*, 920-932.
(42) Shenfu Chen , L. L., Chao Zhao , Jie Zheng *Polymer* **2010**, *51*, 5283-5293.
(43) Chang, Y.; Chen, S. F.; Zhang, Z.; Jiang, S. Y. *Langmuir* **2006**, *22*, 2222-2226.
(44) Huang, C. J.; Brault, N. D.; Li, Y. T.; Yu, Q. M.; Jiang, S. Y. *Advanced Materials* **2012**, *24*, 1834-1837.
(45) Huang, C. J.; Li, Y. T.; Jiang, S. Y. *Analytical Chemistry* **2012**, *84*, 3440-3445.
(46) Huang, C. J.; Li, Y. T.; Krause, J. B.; Brault, N. D.; Jiang, S. Y. *Macromolecular Rapid Communications* **2012**, *33*, 1003-1007.
(47) Yang, W.; Xue, H.; Li, W.; Zhang, J.; Jiang, S. *Langmuir* **2009**, *25*, 11911-11916.

Chapter 2

Enhanced Gas Transport Properties and Molecular Mobilities in Nano-Constrained Poly[1-(trimethylsilyl)-1-propyne] Membranes

2.1. Introduction

Polymeric membranes are gaining wide attention in separation processes owing to their economic viability and operational flexibility.[1,2] Poly(l-trimethylsilyl-1-propyne)(PTMSP), a high free volume glassy polymer, exhibits extraordinarily high gas permeability coefficients and high organic-vapor/permanent-gas selectivities. These unusual transport properties in PTMSP are attributed to its high fractional free volume (FFV) of about 0.34,[3] caused by the inefficient chain packing involving rigid carbon-carbon double bonds, bulky trimethylsilyl and methyl constituent groups, coupled with poor inter-chain cohesion.[4-6] PTMSP has been shown to possess a bimodal distribution of small and large free volume elements with average sizes of 0.4 nm and 1.4 nm,[7] which demands careful attention when choosing a transport model.

In dense polymeric membranes with free volume elements less than ~0.5 nm, molecular transport is driven by the concentration gradient of the penetrant across the membrane and is best described by the *solution diffusion model* [8] which is further discussed in Appendix A. In these membranes, the free volume elements exist as statistical fluctuations, appearing and disappearing at the same timescale, as gas molecule permeation through the membrane. According to this model, the gas permeability coefficient (P) is defined as,

$$P = DS \tag{2.1}$$

where D and S are the gas diffusivity and solubility coefficient, respectively. As the selectivity of the gas component A over B is determined from the permeability ratio,

$$\alpha_{A/B} = \frac{P_A}{P_B} = \left(\frac{D_A}{D_B}\right)\left(\frac{S_A}{S_B}\right) \qquad 2.2$$

the transport is either diffusion or solubility dominated. If a membrane exhibits higher permeability to the larger molecular gas species, due to higher condensability compared to the smaller light gas counterpart, the process is often referred to as 'reverse selective' transport.[9-11] This applies to CO_2/helium transport through PTMSP, where the solubility ratio dominates,[10] as CO_2 possesses a higher sorption coefficient in PTMSP than helium. In contrast, pressure driven *convective pore-like flow* transport mechanisms are found for mass transport systems with free volume elements that exceed ~1 nm in characteristic dimension, and are fixed in size and position relative to the time scale of permeant motion.[8]

Owing to the presence of relatively large free volume elements, PTMSP emerges as a *transitional* polymer, with molecular transport occurring via a combination of Knudsen flow and solution diffusion mechanisms.[5,8,11] Due to its high free volume, PTMSP behaves as an ultramicroporous membrane, with *interconnected microvoids,*[12] resulting in pore flow dominated gas transport.[5] High reverse selectivities towards larger gas components in mixed gas transport were attributed to specific adsorption of the larger permeates within the walls of interconnected free volume elements, thereby creating resistance to transport of smaller, permeate gases.[10] PTMSP possesses a high glass transition temperature (T_g) in excess of 250° C and degrades thermally before it reaches T_g.[13]

Apart from its high gas permeability, PTMSP also exhibits unusual transport properties when subjected to external constraints, as found in the case of nanoparticle based composites.[11,14,15] For instance, Merkel et al. observed that gas permeabilities in PTMSP systematically increased with increased concentration of nanoscale, non-porous, fumed silica (FS) particles.[11] Converse results were obtained for the reverse selectivity. It was concluded that PTMSP's inefficient packing was further enhanced by the incorporation of FS nanoparticles, resulting in *free-phase-transport*, i.e., Knudsen diffusion, which positively impacts permeation but reduces reverse selectivity. Apart from the enhanced free volume, interstitial cavities (mesopores) were also observed to be formed due to particle aggregation in PTMSP nanocomposites leading to a decrease in selectivity.[16] Particle-polymer interaction effects on transport properties of nanocomposites were also investigated in PTMSP nanocomposite studies involving MgO and TiO_2 nanoparticles.[14,17] Both studies reveal increased gas permeabilities compared to bulk PTMSP for higher particle loadings (> 7-10 nominal volume %) due to void generation caused by particle aggregation.

To obtain "particle aggregation free" access to interfacial properties, it has been shown that a planar confinement of thin films yields results quantitatively equivalent to those found in nanocomposites.[18,19] As planar arrangement imposes *uniform* interfacial confinement on the polymer matrix, it provides an interfacial system that can be analyzed more accurately without the complication of particle aggregation. In regards of the material studied here, this approach is well founded, considering the low interfacial interaction (~100 mJ/m) between PTMSP and SiO_2.[20] In the study presented here, we compare the transport properties of free standing thin film PTMSP membranes with the thermo-mechanical properties of SiO_2 supported thin PTMSP films to probe the effect of molecular relaxations on interfacially imposed transport alterations. This involved the systematic analysis of CO_2 and helium permeabilities as a function of the membrane thickness, and measurement of local molecular mobilities that were extracted from nano-thermo-mechanical probing.

2.2. Experimental Section

PTMSP (SSP-070-10gm, lot 9H-15058 Gelest, Inc.) was dissolved in cyclohexane (SSP 4878-02, lot H07623 & G38629, Mallinckrodt Chemicals) at room temperature, producing solutions of concentrations varying from 0.3 to 1.0 wt.% that were subsequently filtered with a 0.2 μm Nylon (Whatman) filter. Anodic aluminum oxide (AAO) membranes (Anodisc 25, 0.2 um, 13 mm Whatman, Inc.), which served as supports for PTMSP films, were attached to aluminum discs with 3 mm holes in the center via an epoxy (5 Minute®, Devcon), exposing the sample area for gas permeation. These membranes were dried for 24 hours before the PTMSP films were spin coated to ensure complete curing of the epoxy, thus preventing any possible contamination of the films. Furthermore, these aluminum discs with the AAO membranes were attached to the silicon substrate during spin-casting to prevent both direct exposure to vacuum on the spin chuck (that holds the sample in place) and possible infiltration of the PTMSP solution into the pores of the AAO membranes. Films of different thicknesses were prepared by spin casting 100 μL of the PTMSP solution at speeds varying from 1000 rpm to 6000 rpm for 1 min on 200 nm pore AAO membranes. Thicker films were fabricated either by solution casting or by spin casting multiple layers of PTMSP to build up the thickness. A cross-sectional view of the spin casted PTMSP membranes for gas permeation measurements is shown in Figure 2.1. For IFA measurements, samples ranging in thickness from 200 nm to 1.4 μm were prepared by spin casting 1.0 and 2.0 wt.% PTMSP solutions on <1,1,1> silicon wafers pre-cleaned by sonication in acetone (10 min) followed by methanol (40 min), and then UV/Ozone cleaning (UV/Ozone Bioforce) for 20 minutes. All the films were dried under ambient conditions. Thin PTMSP films were dried for 18-20 hours, while the thicker films (>1 μm) were dried for about 36 hours.

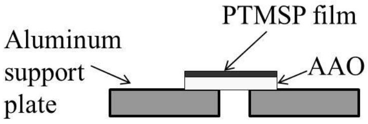

Figure 2.1: Cross sectional view of PTMSP film sample spin casted on AAO over the aluminum support with center hole (diameter 3 mm) for gas permeation.

Permeability measurements were performed using an isobaric permeation system, with regulated gas flow feed to the upstream side of the membrane while the downstream side was maintained at atmospheric pressure. A purge valve was used to vent the gas and remove any contaminant gases present in the line. The downstream permeate gas flow rate (*dV/dt*) was determined using a bubble flow meter. For each upstream gas pressure (p_2), measurements were repeated until a steady state in the permeate gas flow rate was observed, which was then recorded. The observed average time to reach steady state was about 5-10 minutes. The downstream pressure (p_1) was maintained at atmospheric pressure for all the experiments. The gas permeability, P (1 Barrer = 10^{-10} (cm^3(STP) cm)/cm^2 s cmHg) was determined from the flux, J (cm^3(STP)/cm$^2\cdot$s), the membrane cross-sectional area, A (cm^2), the thickness, l (cm), and the externally controlled differential pressure, Δp ($\Delta p = p_2 - p_1$), (cm Hg) as:

$$P = \left(\frac{Jl}{\Delta p} \right) \qquad 2.3$$

Flux was obtained from the following expression [10]

$$J = \left(\frac{273.15 p_{atm}}{76T} \right) \frac{1}{A} \frac{dV}{dt} \qquad 2.4$$

where p_{atm} is the atmospheric pressure in cm Hg, T is the temperature of the gas in Kelvin, (*dV/dt*) is the gas flow rate in cm^3/s. Membrane thicknesses were measured by contact mode scanning force microscopy (SFM) (*Easy Scan 2*, Nanosurf GmbH) of a scratch made on the

PTMSP surface penetrating the thickness of the polymeric film, avoiding perturbing/damaging the supporting AAO membrane after the gas permeabilities had been measured. Gas permeation behaviors were measured in two ways: (i) the initial gas analyzed was CO_2 followed by helium on neat PTMSP films on a series of samples with thicknesses between 200 nm to 4 μm, (ii) the order of the permeates was reversed, i.e., the membranes were exposed first to helium and then to CO_2, and for this measurement a new set of neat membranes were used.

Local energetic investigations were performed on PTMSP thin film samples on silicon wafers with intrinsic friction analysis (IFA) involving contact SFM (*Explorer*, Veeco Inc.) with a custom heating stage. IFA,[21,22] as described in detail in the Experimental Techniques Chapter (Chapter 6) is a spectroscopic contact mode SFM method that is highly surface sensitive. It provides energetic information about the thermally active modes, such as molecular and sub-molecular mobilities.

Lateral force measurements over a 1 μm scan range were performed at temperatures ranging from 30 to 114 ^{o}C. Levers (PPP-CONT, Nanosensors) with nominal and lateral spring constants of ~0.2 N/m and 80 N/m, respectively were used. Prior to the experiment, the levers were conditioned and calibrated. Conditioning of the cantilever tip and calibration of the cantilever torsional spring constant involved pre-scanning on well prepared silicon wafers.[22,25] Tip conditioning involved two steps: (1) chemical-mechanical polishing of the tip on the silicon wafer, and (2) surface passivation of the polished tip surface with the material to be investigated (i.e., PTMSP). In the course of the conditioning process, which eliminates sharp tip asperities, the torsional spring constant is obtained via a blind calibration.[25] All the IFA studies were performed in a glove box with a dry nitrogen atmosphere (<10% humidity).

2.3. Results and Discussion

With 757 nm and 4 μm thick PTMSP films, two representative film thickness regimes are contrasted relative to their CO_2 permeation properties as a function of the pressure drop ($\Delta p = p_2 - p_1$) across the membrane, Figure 2.2.

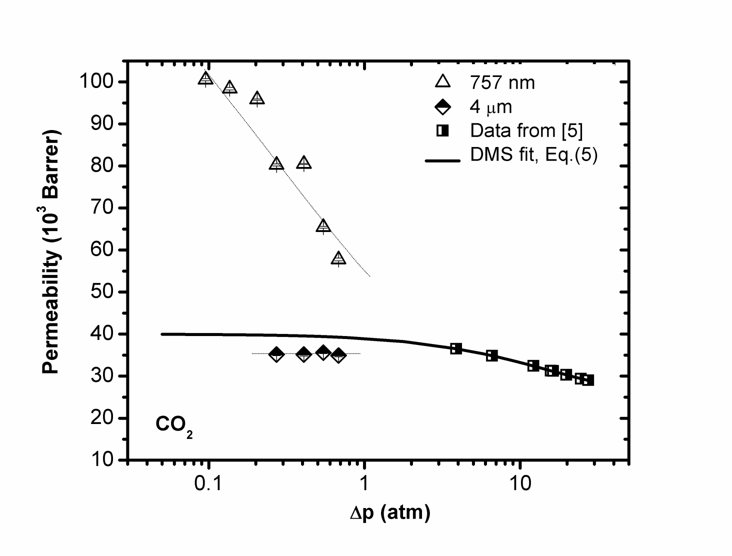

Figure 2.2: Comparison of CO_2 permeability coefficients as function of the pressure drop, Δp, of relatively thick (4 μm) and ultrathin (757 nm) films with bulk (115 μm) membrane data [5], that serve as the basis for the DMS model extrapolation (solid line).

These data are compared to permeability coefficients provided by Srinivasan et al.[5], involving significantly thicker "bulk" PTMSP membranes (~100 mm) that show, as expected, a decrease in the permeability of sorbing gases in glassy polymers with increasing gas pressure, Δp. [5,26] Gas transport in glassy polymeric systems is frequently described in terms of a *dual mode sorption* (DMS) *model*,[26,27] i.e.,

$$P = k_D D_D + \frac{C_H b D_H}{(1 + bp_1)(1 + bp_2)} \qquad 2.5$$

that relates the total permeability P to the membrane's upstream and downstream pressures, p_2 and p_1, respectively. The first term on the right-hand side in Eq.**2.5**, which is reflective of the gas permeation through a densified polymer matrix, represents the product of the Henry's law solubility parameter, k_D, and the penetrant diffusion coefficient, D_D. The second term, containing the Langmuir sorption capacity parameter C_H, the affinity parameter b, and the diffusion coefficient through the Langmuir sites D_H, takes account of the permeation through the excess free volume elements in the polymeric matrix. Applying the DMS model to Srinivasan et al.'s data set, and extrapolating it towards low pressures, Figure 2.2, reveals a reasonable correspondence with our 4 μm data set. The thinner films (represented by the 757 nm film), however, do not conform to the DMS bulk membrane model, neither regarding the permeation magnitude that reveals unexpectedly high permeabilities at low pressure drops, nor its gradient. While we will argue in this paper that the observed enhancement in gas permeation originates from finite size constraints acting on the polymer matrix, the strong dependence of the permeability on pressure will be shown to be caused by accelerated aging of ultrathin PTMSP films when exposed to CO_2.

The impact of aging on the permeation properties of PTMSP for the sorbing gas, CO_2, and the non-sorbing gas, helium, is documented in Figure 2.3 (a,b). Ultrathin polymer membranes are known to exhibit accelerated aging that is caused in part by both the non-equilibrium nature of interfacially constrained systems,[28-30] and the plasticizing effect of sorbing permeates in glassy polymers.[31] We found for relatively thick films (> 1 μm), Figure 2.3(a), the CO_2 permeability coefficient initially increases and then saturates at 36×10^3 Barrer; this corresponds well to the performance of bulk membranes (see Figure 2.2). The increase in permeability of CO_2 in micrometer thick PTMSP membranes, as shown in Figure 2.3(a), originates from plasticization effects caused by strongly sorbing gases like CO_2. Similar time dependent CO_2 permeation behaviors have been widely observed in a variety of glassy polymers.[32,33] Over the time scale of observation, our micrometer thick membranes did not exhibit physical aging, which is apparent from the constant permeability coefficient of ~36 × 10^3 Barrer, which was maintained up to ten hours, a time scale that is relevant for the thin film study presented here. In contrast to CO_2, helium transport, measured through another fresh membrane of similar thickness without prior CO_2 exposure, revealed, over the same time period, a steady permeability coefficient (as anticipated from a non-sorbing gas) of around 6 × 10^3 Barrer, Figure 2.3(a).

For ultrathin films (< 1 μm), Figure 2.3(b), the initial increase (sorption period) in CO_2 permeability is, as expected, much faster than that of thicker films. Extremely high maxima in permeability coefficients of 90 × 10^3 and 19 × 10^3 Barrer for CO_2 and helium, respectively, are observed. These values are almost three times the bulk permeation values, and are indicative of increased free volume in interfacially constrained ultrathin films. The sharp drop in CO_2 permeability is an indication of accelerated aging in thin PTMSP films that dominates the plasticization effect in the polymer caused by the sorbing gas, an argument that has also been made for ultrathin Matrimid™ films, although over a longer time period.[34] It can be assumed that local confinement effects (i.e., thin film confinement) imposed by interfacial constraints in thin PTMSP films are affected much more rapidly by plasticizing effects of CO_2, leading to accelerated aging. Along this line, it has to be noted for future reference that, if physical aging were suppressible, an even higher permeation maximum could have been expected. Helium also revealed a permeability reduction in ultrathin PTMSP films from 19 × 10^3 Barrer to 6 × 10^3 Barrer, Figure 2.3(b), although the rate of aging is significantly lower than that of CO_2. The reduction in helium permeability over time indicates that thin PTMSP films also undergo physical aging without the influence of conditioning effects, such as those caused by the presence of sorbing gases like CO_2.

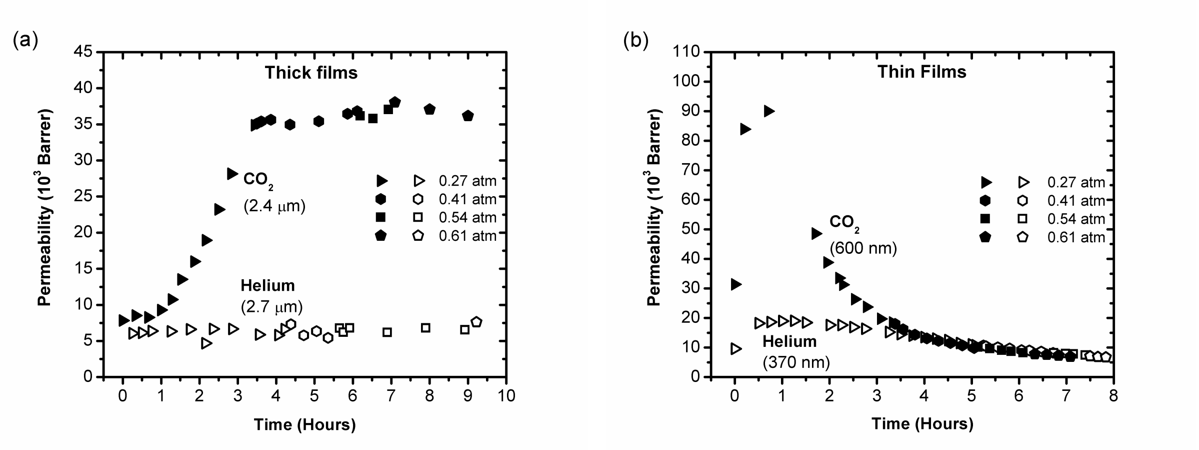

Figure 2.3: Temporal development of CO_2 and helium permeability coefficients in (a) thick PTMSP membranes (2.4 μm and 2.7 μm) and (b) thin films (600 nm and 370 nm) are shown, for differential pressures varying from 0.27 to 0.61 atm. CO_2 permeability coefficients are represented by filled symbols and those of helium with open (unfilled) symbols.

Having addressed the impact of aging, which, for ultrathin films is driven by non-equilibrium free volume relaxation modes, and is further accelerated in the presence of a strongly sorbing gas, we are now ready to present and discuss PTMSP thin film permeation properties. In Figure 2.4(a,b), the CO_2 and helium permeability coefficients are compiled for 240 nm to 4 μm thick PTMSP membranes. The permeability coefficients of CO_2 and helium shown in Figure 2.4(a,b) were all evaluated at low pressure drops ($\Delta p = 0.2$ atm) for consistency, even though the helium permeation was largely independent of the pressure drop applied across the membrane. The plots in Figure 2.4 reveal non-monotonous permeation *vs*. thickness functional behavior for both CO_2 and helium in the sub-micron regime, while films thicker than ~1.5 μm show permeability coefficients coinciding with bulk values of 36×10^3 Barrer and 6×10^3 Barrer for CO_2 and helium respectively. Permeation maxima are observed at around 750 nm. It is important to note that the helium permeation measurements in Figure 2.4(b) involved PTMSP films that have not been previously exposed to CO_2. To warrant time invariant comparisons, it is to be noted that the permeability coefficients of CO_2 for the investigated thick films (> 1 μm) were all recorded three hours after the exposure to CO_2, i.e., when steady state values could be obtained for the permeability coefficients over the time frame of the experiment, as shown in Figure 2.3(a). For thin films, the exposure time was restricted to 15-30 minutes before recording the permeability coefficients to reduce the associated aging effects, as shown in Figure 2.3(b). Furthermore, all the measurements in thin films were completed within two hours. The permeability coefficients of helium were obtained after 30 minutes of gas (helium) permeation for both the thick and thin films, and the measurements were taken within two hours of gas exposure time for consistency. To ensure that the bulk deviating transport properties in the 600-750 nm films were not a consequence of polymeric impregnation into the pores of the supporting AAO membranes, we determined bulk equivalent thicknesses, that *is,* $l_{bulk} = P\Delta p/J$. Thereby, we assumed bulk permeation behavior of CO_2 (i.e., $P = 35 \times 10^3$ Barrer[5]), and substituted for the measured Δp and J (the permeation data of 600-750 nm films shown in Figure 2.4). The resulting equivalent thicknesses, l_{bulk}, significantly underestimate the PTMSP film thicknesses on AAO determined by SFM ($l_{bulk} \approx 260$ nm for $\Delta p = 0.27$ atm and $J = 2.745$ $cm^3(STP)/cm^2\cdot s$ for a SFM determined film thickness of 600-750 nm), confirming no PTMSP impregnation into AAO.

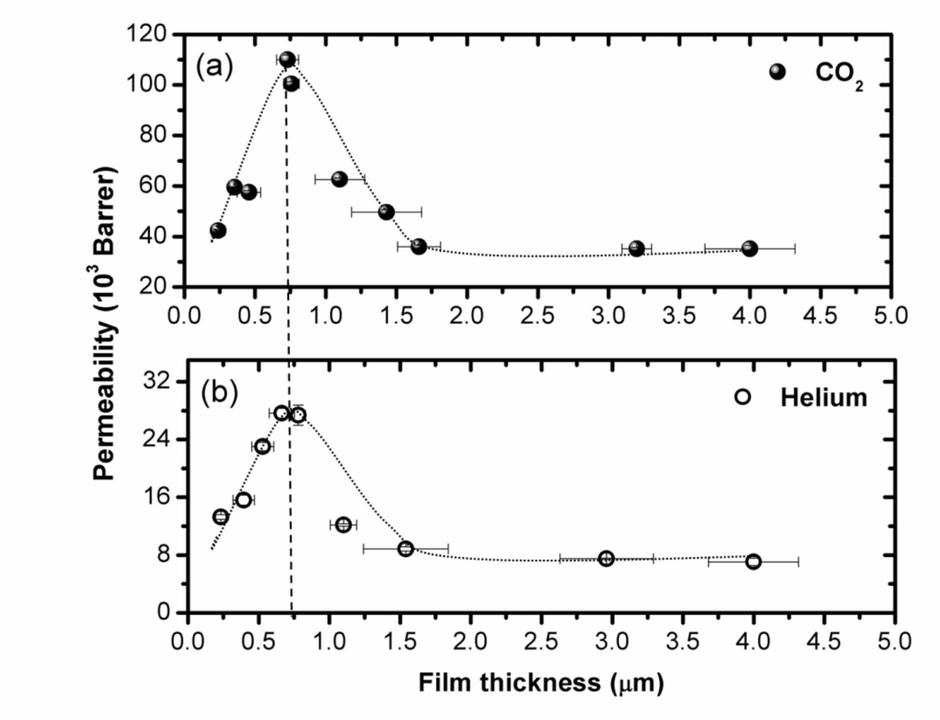

Figure 2.4: Permeability coefficients of (a) CO$_2$ and (b) helium, as function of film thickness. A maximum in the permeation behavior is observed at film thicknesses of 600 to750 nm for both gases.

To provide an explanation for the non-monotonous permeation behavior of PTMSP in the thin film region, we conducted an energetic molecular relaxation mobility analysis based on intrinsic friction analysis (IFA). [21,22,35,36] The IFA methodology, as described in the experimental section, has been shown to be a reliable spectroscopic method to extract energetic molecular mobility information from thin polymer systems. It is important to note that the activation energies obtained by IFA are not diffusion activation energies, but activation energies related to molecular relaxation. In Figure 2.5(a), a representative IFA friction-velocity master curve for an 860 nm thick PTMSP film on silicon oxide is shown, revealing in the inset of Figure 2.5(a) an activation energy of 5.6 ± 0.2 kcal/mol. From similar friction-velocity data sets, activation energies from 200 to 1400 nm thick PTMSP films could be determined, as compiled in Figure 2.5 (b). The activation energies were found to vary from 4 to 7 kcal/mol, depending on the film thickness. In the thick film regime (> 1 μm) the activation energies are 5.4±0.3 kcal/mol, which were attributed to the rotation of the methyl groups on the PTMSP backbone, [37] the only mode that is thermally active, as per molecular conformational calculations.[37] Changes in the activation energies associated to the thermally active modes allow us to draw inferences about how the confinement affects the state of the polymer. The minimum in the activation energy of 4.0 kcal/mol at 600-650 nm in (b) signifies a maximum in the local rotational mobility of the methyl groups. Further, this coincides with the CO_2 and helium permeation maxima observed in thin film membranes, as shown in Figure 2.4. The link made here between molecular mobility and gas transport involving glassy polymers finds support in other studies, such as the quasi-elastic neutron scattering study by Kanaya et al., in which a linear relationship was observed between the oxygen diffusion coefficient and local side-chain molecular mobilities in polyacetylenes.[38]

The three IFA identified thickness (*t*) regimes can be interpreted as follows:

- *t < 300 nm*: In the ultrathin film regime, the observed higher activation energies indicate restricted molecular mobilities, representative of interfacial molecular alignment with increased packing densities, as reported, for instance, by van der Lee et al. for thin PMMA films,[39] although it should be noted that these observations occurred in thinner films. This is not surprising as PMMA is much more flexible than the highly rigid PTMSP molecules.

- *t > 800 nm*: In the thick (bulk-like) film regime, the activation energy saturates to a constant value, indicative of bulk like polymeric structural properties.

- *300 nm < t < 800 nm*: The local and temporal anisotropy of polymer packing and relaxation acts as the driving force for "autodiffusion" [40,41], i.e., interdiffusion of the polymeric chains during the naturally occurring temporal annealing process, when the solvent is driven out. Paired with the inflexibility of PTMSP's rigid backbone, a loosely packed polymeric phase is established within the intermediate film thickness region. Thus, the observed minimum activation energies in Figure 2.5(b) at 600-650 nm, which reveal maximum molecular side-chain mobilities, originate from higher free volume in the polymer phase. This is in agreement with permeation and free volume studies involving SiO_x/PTMSP nanocomposites that report enhanced free volume within the polymer phase, and suggest the presence of interconnected channels.[11] The observed maximum in gas permeabilities (Figure 2.4) for film thicknesses of ~750 nm also supports the argument of high free volume in the polymeric phase. The apparent delay to reach bulk permeation properties at ~1.5 µm compared to the mobility analysis at ~800 nm film thickness is due to the integral effect of permeation measurements.

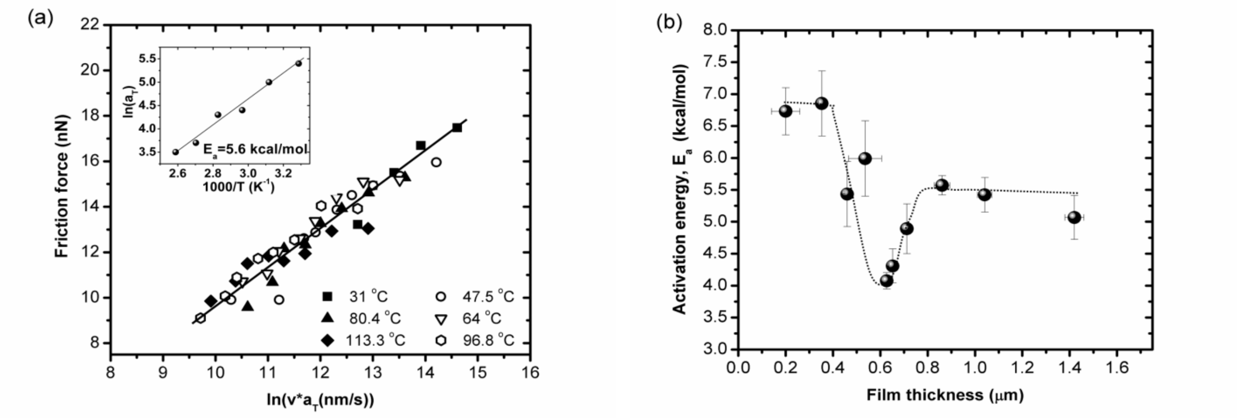

Figure 2.5: Activation energies in PTMSP obtained from IFA. (a) Representative IFA master curve for 860 nm thick PTMSP film over a temperature range from 31°C to 113 °C, revealing an activation energy of E_a = 5.6 kcal/mol (inset), attributed to the methyl side group rotation. (b) Enthalpic (activation) energies of the methyl side group rotation for film thicknesses between 200 and 1400 nm.

Although the large length scales over which interfacial constraints affect the polymer matrix are at first sight astonishing, they have been observed in the literature for rigid polymeric systems, such as conjugated polymers.[42] Polymer chain flexibility and inter-chain cohesive energies were found to have strong influence on the free volume and transport properties in glassy polymers.[4,6]

Since this study addresses only single component gas transport, we have to differentiate the order in which gases flow through the membrane. For this purpose, we present in Figure 2.6, CO_2 and helium permeability coefficient data involving ultrathin (663 and 757 nm) and thick (1.43 and 1.54 μm) membranes that were exposed to both gases in different orders. One film of each mentioned film thickness pair was first exposed to helium, i.e., 663 nm and 1.54 μm thick films (filled symbols), followed by CO_2 permeation. The order was reversed for films of thickness 757 nm and 1.43 μm (open symbols), wherein the films were exposed to CO_2 first. It can be seen from Figure 2.6 (a), that the CO_2 transport is essentially unaffected by any preceding helium exposure, regardless of the film thickness. This is expected, as helium, a light permeate gas, has low condensability in PTMSP and hence does not alter the polymeric matrix. A corresponding result was also found for helium; that is, helium permeation through thick films did not depend on prior CO_2 transport, Figure 2.6 (b). The findings are different, however for helium permeation in the ultrathin film regime, where the permeation coefficients depend on the membrane CO_2 history, Figure 2.6(b). In the ultrathin film regime, i.e., the 663 nm thick PTMSP membrane, which was first purged with helium, ultra-high helium permeabilities around 28×10^3 to 30×10^3 Barrer were found. These values differ significantly from the helium permeation after CO_2 exposure, which was around 9×10^3 to 10×10^3 Barrer, as found for the 757 nm film in Figure 2.6(b). This indicates that CO_2 permeation results in accelerated aging for ultrathin films, an aspect we addressed earlier, Figure 2.3(b), and discussed in terms of a reduction in the overall free volume. Once again the total timeframe of exposure to CO_2 in the case of thin films was restricted to less than 2 hours, while the thick film data were collected after steady state values were achieved, as discussed above in the context of Figure 2.3 and Figure 2.4. Helium permeation data was also collected in the same timeframe as discussed above for both thick and thin films.

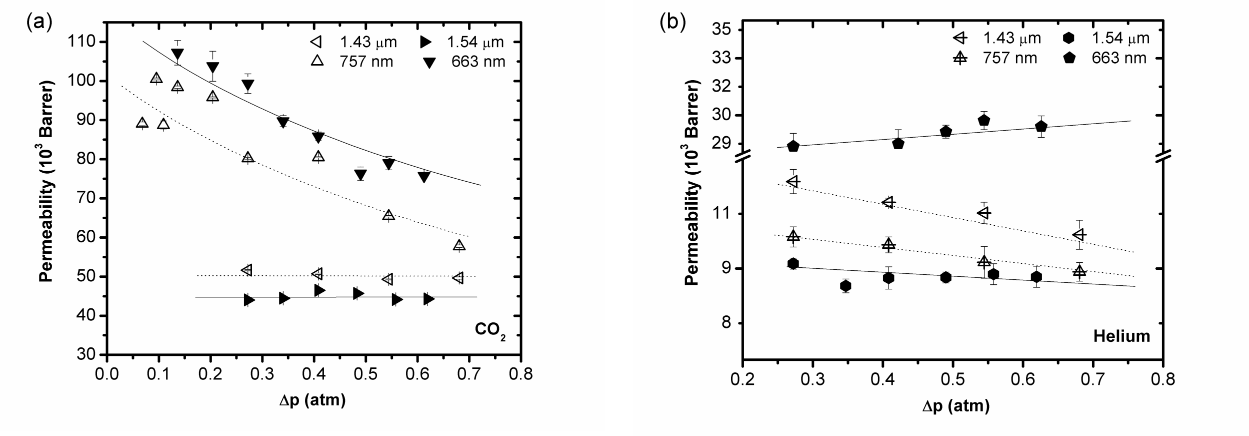

Figure 2.6: Comparison of (a) CO_2 and (b) helium permeability coefficients of ultrathin (663 and 757 nm) and thick (1.43 and 1.54 μm) PTMSP membranes, exposed initially either to helium (663 nm and 1.54 μm) or CO_2 (757 nm or 1.43 μm). Filled symbols and solid guiding lines in Figure 2.6 (a) and (b) represent films that were exposed to helium first. Open symbol data points and dotted guiding lines represent films exposed to CO_2 first.

The impact of CO_2 permeation and interfacial constraints on physical aging in PTMSP and helium permeation is illustrated in Figure 2.7(a,b) for thick and thin film systems. The schematic represents a simplified visualization of the interplay between the pore distribution and transport properties of PTMSP before and after CO_2 exposure. Bulk PTMSP films possess a distribution of small and large pores (cavity sizes of about 0.4 to 0.5 nm and 0.75 to 1.4 nm, respectively [7,43]). Our results indicate that, in thin films (< 1 μm) prior to CO_2 exposure, helium experiences less resistance to flow, evidenced as higher gas permeabilities, suggesting enhanced free volume.

However, when exposed to CO_2, which yields an accelerated physical aging effect in thin films, the free volume elements shrink (collapse) resulting in a decrease of the helium flux, as shown on the right of Figure 2.7(a). On the other hand, in thicker PTMSP films, where interfacial effects are lost, and thus, the free volume elements are smaller than those in ultrathin films, aging effects over the same (short) time scale of ~10 hours are significantly less prominent, leaving the helium transport indifferent to the membrane CO_2 history, Figure 2.7(b). It is to be noted that the schematic in Figure 2.7 is only a simplified depiction of a possible impact of CO_2 permeation on the polymer matrix, and does not capture all the probable scenarios that can affect the free volume distribution in the polymeric matrix or the transport properties. For instance, CO_2 plasticization can induce physical aging leading to pore collapse of larger pores, and thus, a decrease in the number of pores, as well as a decrease in the size of the small pores.[43]

Finally, we turn our attention to the resulting CO_2/helium selectivity of thin PTMSP membranes, based on data presented above. The "reverse selectivity" of CO_2 over helium, i.e., ($\alpha_{CO_2/He} = P_{CO_2} / P_{He}$) is presented in Figure 2.8, for both gas flow order scenarios. Monotonous enhancement in reverse selectivity was observed with decreasing film thickness in films exposed to CO_2 first. Thicker films (> 1 µm) exhibit $\alpha_{CO_2/He}$ values between 5 to 6, corresponding well to the literature.[5,10] Thin films, such as the 240 nm films, however, reveal remarkably high values of up to 17. Note that the aging effect caused by CO_2 in thin films (discussed with Figure 2.3 and Figure 2.6(b)) is also pertinent to mixed gas permeabilities, and is overemphasized in this study by exposing the membrane to a 100 % CO_2 gas stream before exposing it to helium.

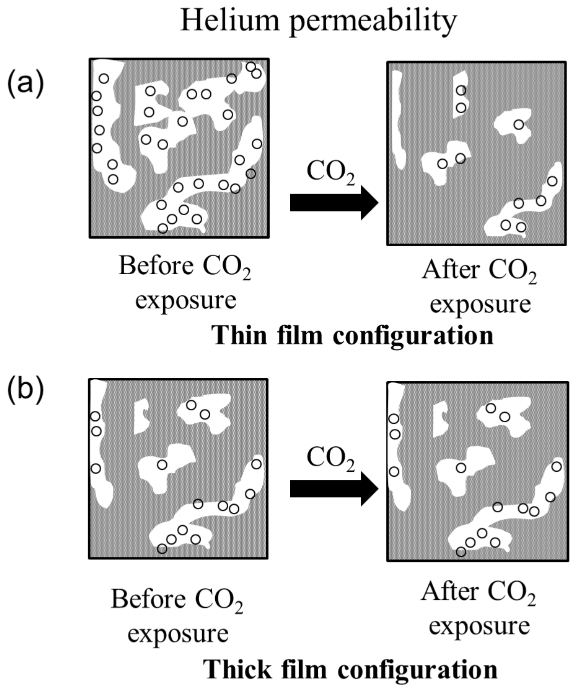

Figure 2.7: Schematic representation of the impact of CO_2 permeation and interfacial constraints on physical aging of PTMSP and helium permeation (a) for thin/interfacially impacted, and (b) thick/bulk-like membranes.

Enhanced selectivities of condensable gases over light gases through thick PTMSP membranes were already reported earlier, in the case of mixed gas permeation.[10] Selectivity enhancements were attributed to the partial blocking of the free volume elements by the condensable gas component, causing a hindrance to the flow of the light gas component in the gas mixture. It is important to note that, in mixed gas studies,[10] the light gas component permeabilities were considerably lower in comparison to single component gas permeation values, but, the condensable gas component permeabilities remained unaltered. Similar behavior was also evident here for CO_2 in both thick and ultra-thin films, Figure 2.6(a). Based on our single gas permeation results presented here, we argue that mixed gas studies of CO_2/helium involving ultra-thin films would result in a further enhancement of the CO_2/helium selectivity. This argument is based on (i) the simultaneous blocking effect towards helium permeation due to the co-permeation of strongly sorbing gas like CO_2, as well as, (ii) the strong plasticization effects of CO_2 found in confined ultrathin films. An opposite trend in selectivity is observed for ultra-thin film systems if purged first with helium, also shown in Figure 2.8, as expected from the high permeation values of helium in the ultrathin film region, Figure 2.6(b).

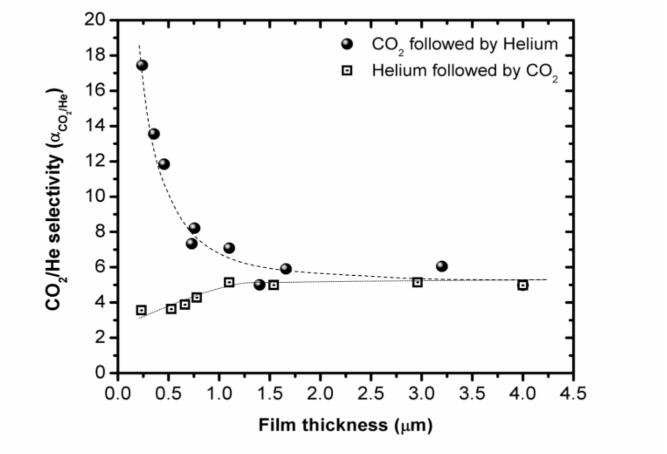

Figure 2.8: CO_2/helium selectivity in PTMSP as function of film thickness reported in two different orders: (i) Films purged first with CO_2 followed by helium. (ii) Films purged first with helium followed by CO_2. The reverse selectivities shown in both the scenarios were obtained at Δp=0.2 atm.

2.4. Conclusions and Summary

Interfacial constraints in ultrathin PTMSP membranes resulted in structural adaptations in the polymer matrix that gave rise to enhanced gas permeabilities and bulk deviating CO_2/helium selectivities. Gas transport properties of PTMSP, analyzed as function of the membrane thickness, revealed a non-monotonous gas permeation behavior of CO_2 and helium, with an approximate three-fold enhancement than bulk values for thin film membranes of ~750 nm thickness. Based on the molecular energetic mobility analysis (IFA) of the thermally active modes in PTMSP, we can conclude that the interfacially induced structural adaptations in PTMSP lead to an increase in free volume for films of 400 to 800 nm thickness. This termination is based on the mobility enhancement found in the methyl side groups within this film thickness regime. However, our aging analysis revealed that these "free-standing" ultra-thin membrane films physically age within hours due to the plasticizing effect of the sorbing gas component that causes a free-volume collapse.

It is important to note that the membranes discussed here possess merely air-polymer interfaces. Thus, it could be argued that, in the presence of solid interfaces (as in nanocomposites), the polymer high-free volume phase could be stabilized by stronger interfacial constraints. This would, however, require an appropriately high loading density of nanoparticles, to confine the polymer to regions of critical length scales. As discussed for PTMSP, the length scale is around 400 to 800 nm. The problem for PTMSP is that it is notoriously difficult to blend with nanoparticles such as silicon oxides due to particle aggregation, resulting in void generation for high particle loadings.[14,17] The formation of voids in nanocomposite membranes give rise to alternate gas transport modes such as Knudsen flow, masking diffusive transport properties.[14]

Considering that interfacial effects were found to impact material and transport properties for many polymer systems, such as the glass transition,[40,44,45] relaxation[28,29] and gas transport properties,[46] the findings presented here have wider implications. For PTMSP nanocomposites, solutions have to be found to capitalize on the interfacial polymer region surrounding the particles without jeopardizing the permeation properties by particle aggregation at high particle loading density. Furthermore, other materials with less impressive gas transport properties than PTMSP might provide comparable properties to bulk PTMSP but with high temporal stability, if interfacially constrained. That said, our on-going research focuses on IFA screening of thin film membrane materials on functionalized and unfunctionalized inorganic surfaces, the establishment of critical length scales that lead to increased free volume, and its translation to nanocomposite membranes.

2.5. References

(1) Bernardo, P.; Drioli, E.; Golemme, G. *Industrial & Engineering Chemistry Research* **2009**, *48*, 4638-4663.

(2) Shao, L.; Low, B. T.; Chung, T. S.; Greenberg, A. R. *Journal of Membrane Science* **2009**, *327*, 18-31.

(3) Morisato, A.; Shen, H. C.; Sankar, S. S.; Freeman, B. D.; Pinnau, I.; Casillas, C. G. *Journal of Polymer Science Part B-Polymer Physics* **1996**, *34*, 2209-2222.

(4) Nagai, K.; Masuda, T.; Nakagawa, T.; Freeman, B. D.; Pinnau, I. *Prog. Polym. Sci.* **2001**, *26*, 721-798.

(5) Srinivasan, R.; Auvil, S. R.; Burban, P. M. *Journal of Membrane Science* **1994**, *86*, 67-86.

(6) Savoca, A. C.; Surnamer, A. D.; Tien, C. F. *Macromolecules* **1993**, *26*, 6211-6216.

(7) Hill, A. J.; Freeman, B. D.; Jaffe, M.; Merkel, T. C.; Pinnau, I. *Journal of Molecular Structure* **2005**, *739*, 173-178.

(8) Wijmans, J. G.; Baker, R. W. *Journal of Membrane Science* **1995**, *107*, 1-21.

(9) Merkel, T. C.; Freeman, B. D.; Spontak, R. J.; He, Z.; Pinnau, I.; Meakin, P.; Hill, A. J. *Science* **2002**, *296*, 519-522.

(10) Pinnau, I.; Toy, L. G. *Journal of Membrane Science* **1996**, *116*, 199-209.

(11) Merkel, T. C.; He, Z. J.; Pinnau, I.; Freeman, B. D.; Meakin, P.; Hill, A. J. *Macromolecules* **2003**, *36*, 6844-6855.

(12) Hofmann, D.; Fritz, L.; Ulbrich, J.; Paul, D. *Polymer* **1997**, *38*, 6145-6155.

(13) Ichiraku, Y.; Stern, S. A.; Nakagawa, T. *Journal of Membrane Science* **1987**, *34*, 5-18.

(14) Matteucci, S.; Kusuma, V. A.; Sanders, D.; Swinnea, S.; Freeman, B. D. *Journal of Membrane Science* **2008**, *307*, 196-217.

(15) Winberg, P.; Desitter, K.; Dotremont, C.; Mullens, S.; Vankelecom, I. F. J.; Maurer, F. H. J. *Macromolecules* **2005**, *38*, 3776-3782.

(16) De Sitter, K.; Winberg, P.; D'Haen, J.; Dotremont, C.; Leysen, R.; Martens, J. A.; Mullens, S.; Maurer, F. H. J.; Vankelecom, I. F. J. *Journal of Membrane Science* **2006**, *278*, 83-91.

(17) Matteucci, S.; Kusuma, V. A.; Kelman, S. D.; Freeman, B. D. *Polymer* **2008**, *49*, 1659-1675.

(18) Bansal, A.; Yang, H. C.; Li, C. Z.; Cho, K. W.; Benicewicz, B. C.; Kumar, S. K.; Schadler, L. S. *Nature Materials* **2005**, *4*, 693-698.

(19) Sen, S.; Xie, Y.; Bansal, A.; Yang, H.; Cho, K.; Schadler, L. S.; Kumar, S. K. *European Physical Journal-Special Topics* **2007**, *141*, 161-165.

(20) Killgore, J. P.; Overney, R. M. *Langmuir* **2008**, *24*, 3446-3451.

(21) Knorr, D. B.; Gray, T. O.; Overney, R. M. *J. Chem. Phys.* **2008**, *129*, 074504.

(22) Knorr, D. B.; Gray, T. O.; Overney, R. M. *Ultramicroscopy* **2009**, *109*, 991-1000.

(23) Ward, I. M. *Mechanical Properties of Solid Polymers*; Wiley-Interscience, London, 1971.

(24) J.D.Ferry *Viscoelastic Properties of Polymers*; John Wiley &Sons, 1980.

(25) C. K. Buenviaje, S. R. G., M. H. Rafailovich, and R. M. Overney In *Materials Research Society Symposium Proceedings*, 1998; Vol. 552, pp 187-192.

(26) Merkel, T. C.; Bondar, V.; Nagai, K.; Freeman, B. D. *Journal of Polymer Science Part B-Polymer Physics* **2000**, *38*, 273-296.

(27) Koros, W. J.; Chan, A. H.; Paul, D. R. *Journal of Membrane Science* **1977**, *2*, 165-190.

(28) Rowe, B. W.; Freeman, B. D.; Paul, D. R. *Polymer* **2009**, *50*, 5565-5575.

(29) Huang, Y.; Paul, D. R. *Polymer* **2004**, *45*, 8377-8393.

(30) Dorkenoo, K. D.; Pfromm, P. H. *Macromolecules* **2000**, *33*, 3747-3751.

(31) Horn, N. R.; Paul, D. R. *Polymer* **2011**, *52*, 1619-1627.

(32) Bos, A.; Punt, I. G. M.; Wessling, M.; Strathmann, H. *Journal of Polymer Science Part B-Polymer Physics* **1998**, *36*, 1547-1556.

(33) Kanehashi, S.; Nakagawa, T.; Nagai, K.; Duthie, X.; Kentish, S.; Stevens, G. *Journal of Membrane Science* **2007**, *298*, 147-155.

(34) Horn, N. R.; Paul, D. R. *Polymer* **2011**, *52*, 5587-5594.

(35) Sills, S.; Overney, R. M. *Physical Review Letters* **2003**, *91*.

(36) Sills, S.; Gray, T.; Overney, R. M. *J. Chem. Phys.* **2005**, *123*.

(37) Knorr, D. B., Jr.; Kocherlakota, L. S.; Overney, R. M. *Journal of Membrane Science* **2010**, *346*, 302-309.

(38) Kanaya, T.; Tsukushi, I.; Kaji, K.; Sakaguchi, T.; Kwak, G.; Masuda, T. *Macromolecules* **2002**, *35*, 5559-5564.

(39) van der Lee, A.; Hamon, L.; Holl, Y.; Grohens, Y. *Langmuir* **2001**, *17*, 7664-7669.

(40) Sills, S.; Overney, R. M.; Chau, W.; Lee, V. Y.; Miller, R. D.; Frommer, J. *J. Chem. Phys.* **2004**, *120*, 5334-5338.

(41) Buenviaje, C.; Ge, S. R.; Rafailovich, M.; Sokolov, J.; Drake, J. M.; Overney, R. M. *Langmuir* **1999**, *15*, 6446-6450.

(42) Campoy-Quiles, M.; Sims, M.; Etchegoin, P. G.; Bradley, D. D. C. *Macromolecules* **2006**, *39*, 7673-7680.

(43) Consolati, G.; Genco, I.; Pegoraro, M.; Zanderighi, L. *Journal of Polymer Science Part B-Polymer Physics* **1996**, *34*, 357-367.

(44) Forrest, J. A.; Dalnoki-Veress, K. *Advances in Colloid and Interface Science* **2001**, *94*, 167-196.

(45) Keddie, J. L.; Jones, R. A. L.; Cory, R. A. *Europhysics Letters* **1994**, *27*, 59-64.

(46) Killgore, J. P.; Kocherlakota, L. S.; Overney, R. M. *Journal of Polymer Science Part B-Polymer Physics* **2010**, *48*, 434-441.

Chapter 3

Transport and Stability Enhancement in Interfacially and Dimensionally Constrained CO_2 Selective Polymers Embedded in Nanoporous Sieve Membranes

3.1 Introduction

Separation limitations in the gas permeability and selectivity of pristine polymeric membranes have recently been shown to be circumvented by selected organic-inorganic nanocomposite membranes.[1,2] With the incorporation of nanoparticles in polymer matrices, such as nonporous fumed silica (FS) into poly(4-methyl-2-pentyne) (PMP)[3,4] or poly[l-(trimethylsily1)-1-propyne] (PTMSP)[5] multifold enhancements in the gas permeability relative to their neat counterparts were achieved. Similar observations as for FS particles were made involving MgO and TiO_2 nanoparticle filled PTMSP composites.[6,7] It was hypothesized that adding nanoparticles to rigid bulky substituted polyacytelene systems, such as PTMSP and PMP, disrupt molecular packing, thus, resulting in an increase in the polymeric free-volume.[3,5] An increase in free-volume could be experimentally confirmed in PTMSP/FS nanocomposites via positron annihilation lifetime spectroscopy (PALS) and attributed to inefficient chain packing, owing to the rigid and twisted conformation of PTMSP chains.[5,8] In search for reverse selective polymers for CO_2 extraction a system that has garnered increased attention recently is poly(ethylene oxide) PEO. The high affinity of CO_2 to ether oxygens in ethylene oxide, is responsible for the CO_2/light gas separation properties.[9,10] However the strong tendency of PEO to crystallize is detrimental for gas permeability, and thus, current efforts are focused towards designing PEO based membranes with reduced crystallinity.[10] Methodologies for mitigating crystallinity in PEO include, for instance, the use of low molecular weight PEO (also referred to as poly(ethylene glycol)(PEG) for molecular mass below 20,000 g/mol). Other approaches involve microphase separated block copolymers with PEO and polyamides[11,12] or polyimides[13] segments, revealing amorphous PEO phases within a rigid mechanically supportive matrix, or highly branched, crosslinked PEO containing systems.[14] Poly(amide-6-b-ethylene oxide)(PEBAX)–silica hybrid membranes were shown to exhibit improved gas transport properties over the neat polymer.[2] Blends of poly(ethylene oxide)-poly(butylene terephthalate) (PEO-PBT) copolymer and polyethylene glycol-dibutyl ether (PEG-DBE) were shown to exhibit outstanding CO_2 permeabilities of ~750 Barrer with CO_2/N_2 reverse selectivity of ~40,[15] placing it at the Robeson limit.

Interfacial and dimensional constraining effects on the polymer matrix could also be observed in planar thin film configurations.[16-18] An energetic analysis of the methyl side group rotation in PTMSP thin films on SiO_x showed a prominent increase in the methyl mobility supporting the assumption of free-volume enhancements in constrained planar films.[17] The CO_2 and helium gas permeation in free standing thin PTMSP films of corresponding thicknesses also surpassed the bulk polymeric properties. Similarly further higher CO_2 permeances than those found in PEO-PBT+PEG-DBE were reported in ultra-thin films of PEO-PBT copolymeric membranes.[19] The permeances were found to increase from 0.8 m^3(STP) m^{-2} h^{-1} bar^{-1} to 5 m^3(STP) m^{-2} h^{-1} bar^{-1}, as the film thickness reduced from 170 nm to 45 nm, the highest permeance values for CO_2 through PEO based polymers. The CO_2/N_2 selectivity in the ultra-thin films (~45 nm) was found to be 60. Yave et al. proposed that interfacial confinement of the polymer could be causing altered molecular relaxations/mobilities, which influence the transport properties of the polymer.[19]

That indeed thin planar films can be compared to nanocomposites has been shown earlier in a study of planar free standing polystyrene films that showed analogous changes in a free-volume critical property, the glass transition temperature, as found in polystyrene-silica nanocomposites.[16,18] Thus, the findings from planar thin film studies support the assumption of free-volume enhancements in polymer nanocomposite membranes for particle loading densities that yield a critical polymer dimensional confinement, as illustrated in Figure 3.1(a) with the parameter ξ. However accelerated physical aging of thin films[20-22] and particles aggregation with consequential interstitial transport in nanocomposites[8] pose challenges in their practical applications.

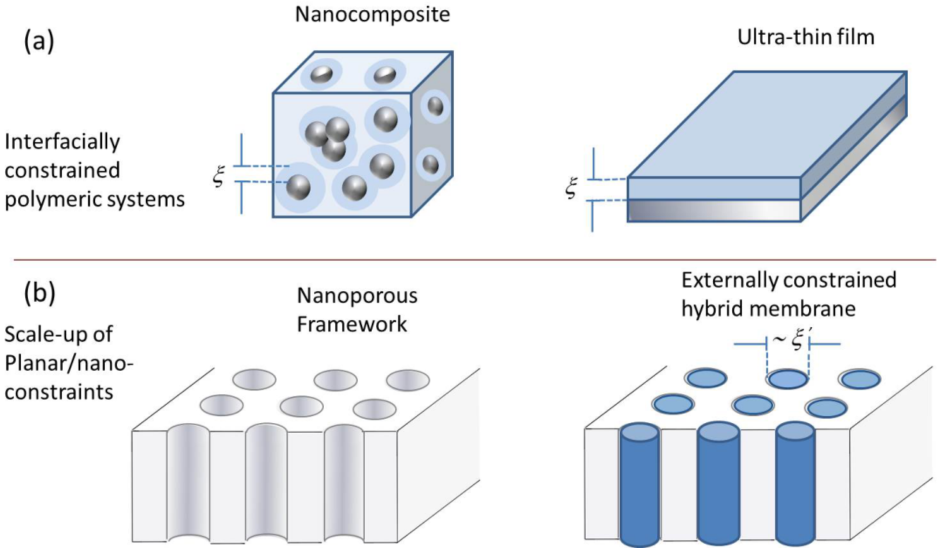

Figure 3.1: Interfacial dimensional constraints identified by the dimensional parameter ξ are transposed from (a) nanoparticle-based composites and ultra-thin films to (b) systems within which the polymer is incorporated in nanoporous membranes.

It is the critical dimensional parameter ξ, obtained from thin-film studies, and shortcomings addressed in nanocomposites and thin films that are of particular interest in this study. We report on imposing comparable dimensional constraints on PTMSP and PEO as found in earlier thin-film studies, by incorporating them into straight cylindrical, sieve-like, inorganic nanoporous membranes, Figure 3.1(b). The PTMSP-AAO hybrid membrane study will show that such organic-inorganic hybrid membranes not only yield improved permeation and selectivity properties over pristine bulk PTMSP, but also a twenty-fold reduction in physical aging, if compared to thin PTMSP films, which have been found to be particularly susceptible to free-volume collapse in the presence of sorbing gases.[17,20,21] PEO-AAO hybrid membranes on the other hand reveal improved CO_2 selectivity, while the gas permeation fluxes were controlled by the top bulk PEO layer.

The porous membranes of choice for this study were anodic aluminum oxide (AAO) membranes due to their straight and well dimensioned pore sizes. The AAO membranes are being extensively employed as templates to grow organic nanostructures owing to their uniform, highly dense nanoscale porous configuration.[23-26] They have also been investigated as a property altering confining support system for polymer membranes.[27] A recent study of poly(tert butyl acrylate) (PtBA) impregnated into the pores of AAO membranes (pore size ~200 nm) resulted in a CO_2 permeability transport enhancement that was found to exceed the virgin bulk polymer membrane property fifteen-fold.[27] The increase was attributed to the constraint-induced-structural alterations of the polymer matrix, causing enhanced free-volume, i.e., molecular mobility, in PtBA, as supported by the observed reduction in the glass transition of ~20 ^{o}C from the bulk PtBA value.

3.2 Experimental Section

The PTMSP (Gelest, Inc.) was dissolved in cyclohexane (Mallinckrodt Chemicals) at room temperature, producing 1.0 wt.% solution that was subsequently filtered with a 0.2 μm Nylon (Whatman) filter. The AAO membranes (Anodisc 25, 0.2 μm, 13 mm Whatman, Inc.) were functionalized with octyltrichlorosilane (Acros Organics) prior to the impregnation of PTMSP, following a well-established silanization procedure[28] to render the pores hydrophobic. The procedure involves a pretreatment of the AAO membranes by heating them to 300 °C for 4 hours, then soaking them in 30 % hydrogen peroxide solution at room temperature, followed by boiling in water for 30 min and then drying them at ~80 °C for 1 hour. Silanization of AAO membranes was accomplished by immersing the pretreated membranes in octyltrichlorosilane/toluene solution (volume ratio 5mL:150 mL) under an inert nitrogen atmosphere for three hours. The functionalized membranes were then washed in toluene, ethanol and water to remove any unreacted silane from the membrane surface. The PTMSP was impregnated into the pores of the silanized AAO membrane of thickness L_c via vacuum suction at the bottom of AAO and pipetting 1% PTMSP solution on the top (Figure 3.2). Full impregnation is indicated by wetting/bubbling of the polymer solution at the outlet (bottom surface) of the AAO membrane. Filled hybrid membranes were dried in ambient conditions for two days to ensure solvent evaporation. The vacuum assisted solution impregnation method, leaves a remnant top layer of PTMSP at the membrane inlet side, as illustrated in Figure 3.2, and shown in Figure 3.4. The accumulated top bulk PTMSP layer is thinned down to a thickness (L_b) of 3 to 5 μm via chemical-mechanical etching using cyclohexane. After additional 36 hours of drying in ambient conditions and for an hour under vacuum, the hybrid membranes are glued with an epoxy (5 Minute®, Devcon) to aluminum support plates that possess 3 mm holes in the center for gas permeation. The transport properties of the hybrid PTMSP-AAO membranes are compared to unconfined micrometer-thick pristine bulk PTMSP membranes that were fabricated by multilayer spin casting of PTMSP on AAO membranes. Thereby AAO served only as support, revealing no measurable polymer impregnation.[17] Scanning electron microscopy (SEM) was used to image the cross-section of the membranes. The samples were sputter-coated with gold-palladium using a SPI Sputter™ Coater (Structure Probe, Inc.; West Chester, PA) and were analyzed with a JEOL 7000 SEM with a beam voltage of 10 kV (Electron Microscopy Center, University of Washington). Energy dispersive Spectroscopy (EDS) was used to characterize the chemical compositions of the membranes.

PEO-AAO membranes were fabricated by initially dissolving PEO (Molecular weight: 4×10^6 g/mol, PolySciences, Inc. Lot # 587082) in acetonitrile producing 2 wt.% solution and drop casting ~100 μl of the solution on the surface of AAO membrane (Anodisc 25, 0.2 μm, 13 mm Whatman, Inc.). The membranes were dried under ambient conditions for 24 hours followed by annealing in vaccum oven for 5 min at 70 °C. The hybrid membranes are glued with an epoxy (5 Minute®, Devcon) to aluminum support plates that possess 3 mm holes in the center for gas permeation. Bulk unconfined PEO membranes were prepared by drop casting 2% PEO solution on AAO supported unconfined spin cast PTMSP membranes prepared via the procedure described above. There by any PEO impregnation into the AAO membrane could be prevented and these membranes could be used as bench-mark for assessing the performance of bulk unconfined PEO films and comparing them to hybrid PEO-AAO membranes.

Permeability measurements were performed by the constant volume variable pressure method which is further elaborated in Chapter 6.[10] Gas permeability (1 Barrer= 10^{-10} cm^3 (STP) cm/cm^2 s cm Hg) was calculated from the steady-state rate of pressure increase in a fixed downstream volume:

$$(P)_i = \frac{V_d L}{p_2 A R T}\left[\left(\frac{dp_1}{dt}\right)_{SS} - \left(\frac{dp_1}{dt}\right)_{leak}\right] \qquad 3.1$$

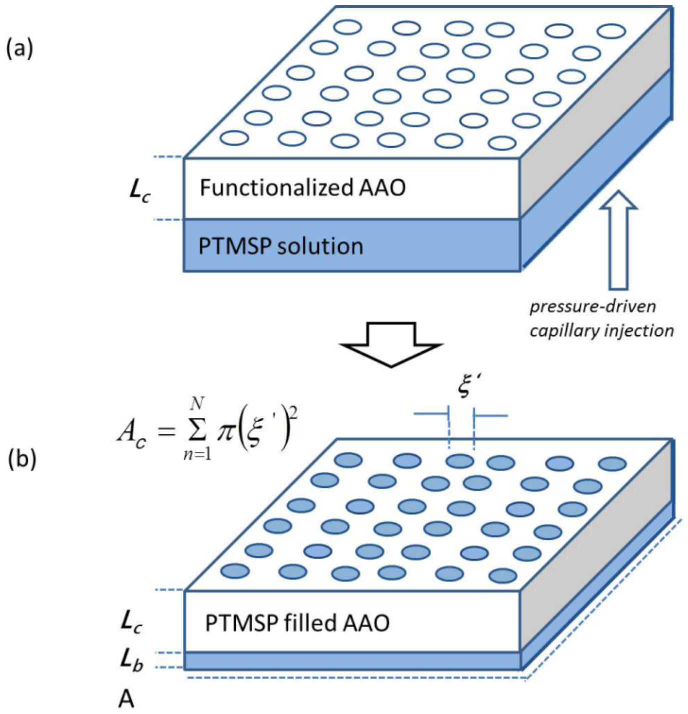

Figure 3.2: Schematic of hybrid polymer-AAO membrane, (a) before polymeric impregnation and (b) after impregnation, defining the relevant system parameters, A_c, L_c, L_b and the pore diameter ξ'. The total projected area A is consistent with the area of the ad-layer.

where V_d is the downstream volume (cm^3), $L = L_c + L_b$ is the overall hybrid membrane thickness, p_2 is the upstream absolute pressure (cm Hg), R is the gas constant (0.278 cm Hg cm^3/cm^3(STP) K), T is the absolute temperature (K), $(dp_1/dt)_{ss}$ and $(dp_1/dt)_{leak}$ are the steady-state rates of pressure rise (cm Hg/s) in the downstream volume at a fixed upstream pressure and under vacuum, respectively. The $(dp_1/dt)_{leak}$ was less than 1% of $(dp_1/dt)_{ss}$. The thickness of the bulk layer (L_b) on the top of AAO membranes (Figure 3.2) was measured by contact mode scanning force microscopy (SFM) (*Easy Scan 2*, Nanosurf GmbH), after the gas permeabilities have been measured, from a scratch made through the polymeric ad-layer, avoiding damaging the supporting AAO membrane. The stability performance of the confined PTMSP membranes was evaluated by tracking the permeabilities of helium and nitrogen at pressure drop (Δp) of 0.54 atm for 15 days through an impregnated PTMSP membrane, freshly prepared via the same procedure as described above. A similar aging study was performed on thick PTMSP film, to compare their aging performance with that of constrained PTMSP in the AAO pores.

3.3 Results and Discussion

3.3.1 PTMSP-AAO hybrid membranes

The SEM image and EDS spectrum of the cross section of a silanized AAO membrane are shown in Figure 3.3(a) and (b), respectively. Peaks of aluminum, oxygen, gold and palladium corresponding to the elemental composition of AAO and the sputter coated Pd-Au layer were evidenced in the EDS spectrum. The low intensity silicon peak is indicative of an ultrathin silane coating. In Figure 3.3(c) helium permeability is compared for neat, silanized, and silane functionalized PTMSP impregnated AAO membranes. A 16 % helium permeation reduction was observed for silanized AAO compared to the neat AAO, indicating that functionalization of AAO did not result in pore clogging. The drastic reduction in the gas permeation by four orders of magnitude is a first indication of successful PTMSP incorporation into AAO.

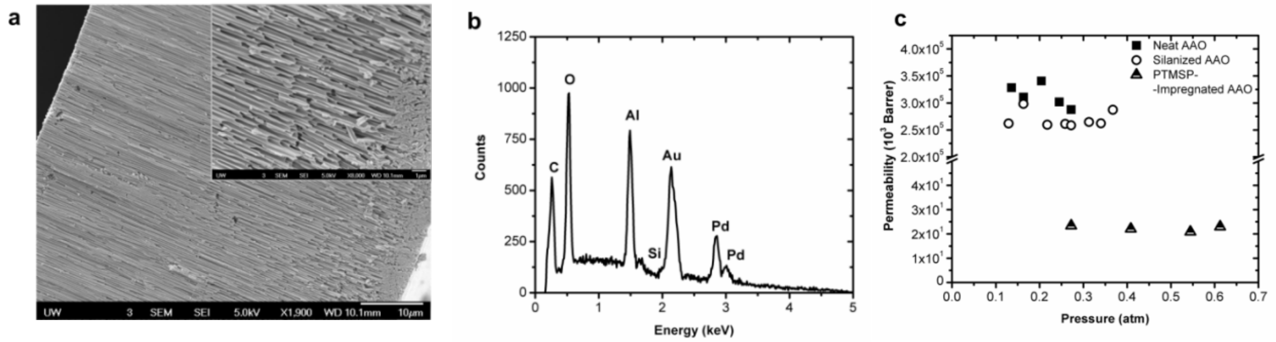

Figure 3.3: (a) SEM cross-sectional view of a silane functionalized AAO membrane. (b) EDS elemental composition spectrum of silanized AAO pore walls (c) Comparison of helium permeabilities of a neat AAO membrane with that of silanized and PTMSP impregnated AAO membranes.

SEM cross-sectional analysis of the AAO membrane, Figure 3.4 (a), documents with polymeric rods that stretch through the entire length of the AAO membrane, the quality of PTMSP impregnation. A close-up view of the rods is provided with the inset of Figure 3.4 (a). The EDS spectra on PTMSP wires reveal prominent silicon and carbon peaks corresponding to the silicon and carbon atoms in PTMSP, Figure 3.4 (b). The EDS spectra taken on the pore walls of AAO expose, as expected, a relatively low carbon peak and a vanishing silicon signal, Figure 3.4 (c). Peaks of aluminum, oxygen, palladium and gold were also observed in the EDS spectra that correspond well to the elemental composition of AAO and the sputter coated Pd-Au layer, respectively. The SEM cross-sectional analysis in Figure 3.4 (a) also shows the surface ad-layer.

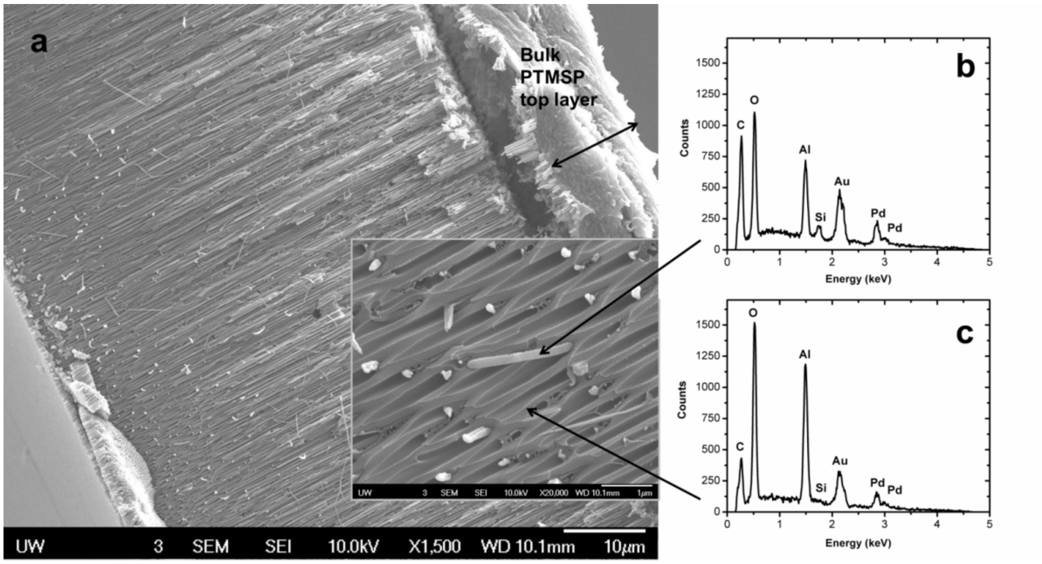

Figure 3.4(a) SEM cross-sectional view of functionalized AAO membrane impregnated with PTMSP (before chemical-mechanical etching). The inset of Figure 3.4 reveals a close-up view of the polymer rods. The elemental composition of (b) polymer rods is contrasted to (c) AAO walls as revealed by the EDS spectra.

The permeation properties of the AAO confined PTMSP phase are evaluated with a resistance model,[29,30] in which the total permeation flux, $Q_{t,i}$ of the composite membrane is given by the resistances of the confined polymeric phase in the AAO pores, $R_{c,i}$, the surface ad-layer, $R_{b,i}$, and that of an effective interfacial resistance, $R_{int,i}$, capturing the transition from the confined polymeric phase in the AAO pores to the bulk phase in the surface-ad-layer, i.e.,

$$\frac{Q_{t,i}}{\Delta p_{t,i}} = \left(R_{c,i} + R_{b,i} + R_{int,i}\right)^{-1} \tag{3.2}$$

Thereby, i, represents the permeate gas, and $\Delta p_{t,i}$ stands for the pressure drop across the entire membrane. The permeation resistance within the confined PTMSP phase and the ad-layer are provided by

$$R_{c,i} = \frac{L_c}{P_{c,i} A_c}, \quad A_c = \rho A \tag{3.3 (a)}$$

$$R_{b,i} = \frac{L_b}{P_{b,i} A} \tag{3.3 (b)}$$

where L_c and L_b, $P_{c,i}$ and $P_{b,i}$, and A_c and A represent the thicknesses, permeabilities and cross-sectional areas of the confined phase and the surface ad-layer, respectively, as illustrated in Figure 3.2 (b). The area of gas permeation in the confined phase depends on the porosity 'ρ'of the cylindrically porous AAO membrane, i.e., $A_c = \rho A$. The average porosity of the AAO membranes was determined by SEM to be 0.41(±0.08). In the current model, any gas permeation through the solid walls of AAO membrane is neglected.

PTMSP bulk permeability values, $P_{b,i}$,, were obtained from free-standing film membranes that were prepared on top of unimpregnated porous AAO substrates (see details elsewhere[17]) according to

$$\frac{Q_{t,i}^{bulk}}{\Delta p_t} = \left(\frac{L_b}{P_{b,i} A}\right)^{-1} \tag{3.4}$$

where $Q_{t,i}^{bulk}$ stands for the bulk permeation flux. It was argued that for a high-permeability polymer like PTMSP, the effective area of permeability for porous membrane supported ultrathin polymeric films is limited to the open conduits (pores) of the supporting membrane, i.e., an effective surface permeation area of ρA.[17,30] The same argument can be made here too for the PTMSP ad-layer, as illustrated in Figure 3.5.

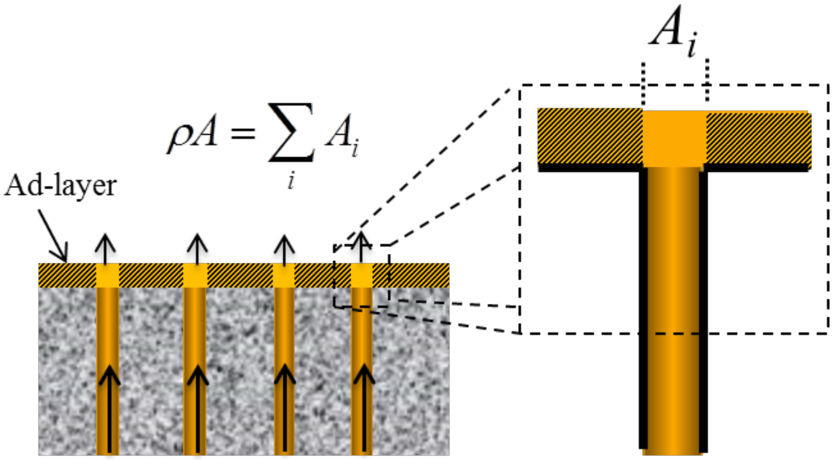

Figure 3.5: Schematic of the gas permeation through hybrid PTMSP-AAO polymeric membranes. For ultrathin polymeric films (or ad-layers as indicated) of high free volume, it can be assumed that the effective transport area is congruent to the area of the porous AAO sieve membrane, ρA, due to limited transport dispersion laterally.

Bulk permeability values for CO_2, He, N_2 of 28×10^3 Barrer, 5.9×10^3 Barrer and 5.8×10^3 Barrer, respectively, were deduced at 0.6 atm from the flux data (Figure 3.6), and found to be in good agreement with the widely reported literature values.[31-33] For the determination of permeability of the constrained polymeric phase in the AAO pores, $P_{c,i}$, the interfacial resistance R_{int} in Eq. (3.2) can be ignored, as PTMSP, extruded through the AAO pores into the ad-layer, forms a continuous material phase at the interface (Figure 3.5).

Figure 3.7 shows the flux data for CO_2, He, N_2 through the hybrid PTMSP-AAO membrane from which $P_{c,i}$ was determined, according to the appropriately adjusted Eq. (3.2), i.e.,

$$\frac{Q_{t,i}}{\Delta p_t} = \rho A \left(\frac{L_b}{P_{b,i}} + \frac{L_c}{P_{c,i}} \right)^{-1} \qquad 3.5$$

with $L_b = 2.90 \pm 1$ µm and $L_c = 60$ µm (thickness of the AAO membranes). Permeabilities of PTMSP in the confined phase ($P_{c,i}$) deduced from the flux data (Figure 3.7) are provided in Figure 3.8. The source for the large error bars in the permeability (P_c) determination (Figure 3.8 (a) and (b)) is due the thickness variation of the PTMSP remnant top ad-layer.

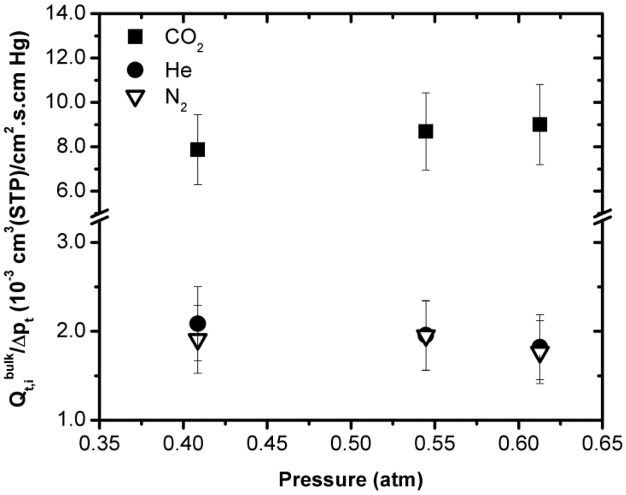

Figure 3.6: Pressure-difference normalized flux data, $Q_{t,i}^{bulk}/\Delta p_t$ for a thick (3.1±0.5 µm) unimpregnated PTMSP membrane as a function of the upstream gas pressure (gauge).

Based on Figure 3.8 (a), CO_2, He, and N_2 permeabilities in PTMSP's confined phase (P_c) are found to be independent of the gas pressure over the current range of measurements. They exceed the bulk values (P_b) four- to seven-fold. While comparably high permeability values were found in ultrathin (< 1 µm) PTMSP membranes, they showed strong pressure dependence that originated from CO_2- induced plasticization.[17]

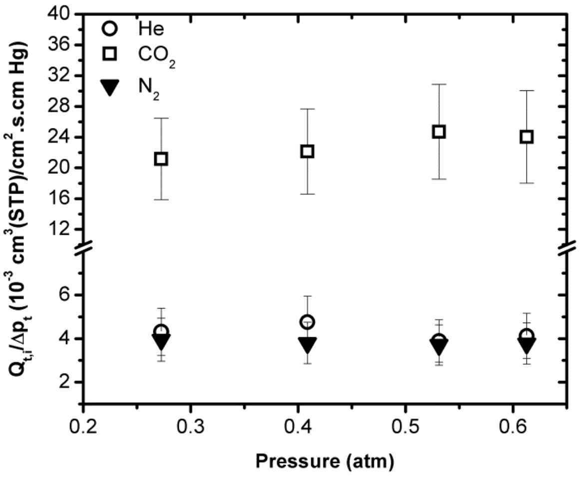

Figure 3.7: Pressure difference normalized flux data, $Q_{t,i}/\Delta p_t$ of a hybrid PTMSP-AAO membrane as a function of the upstream gas pressure (gauge).

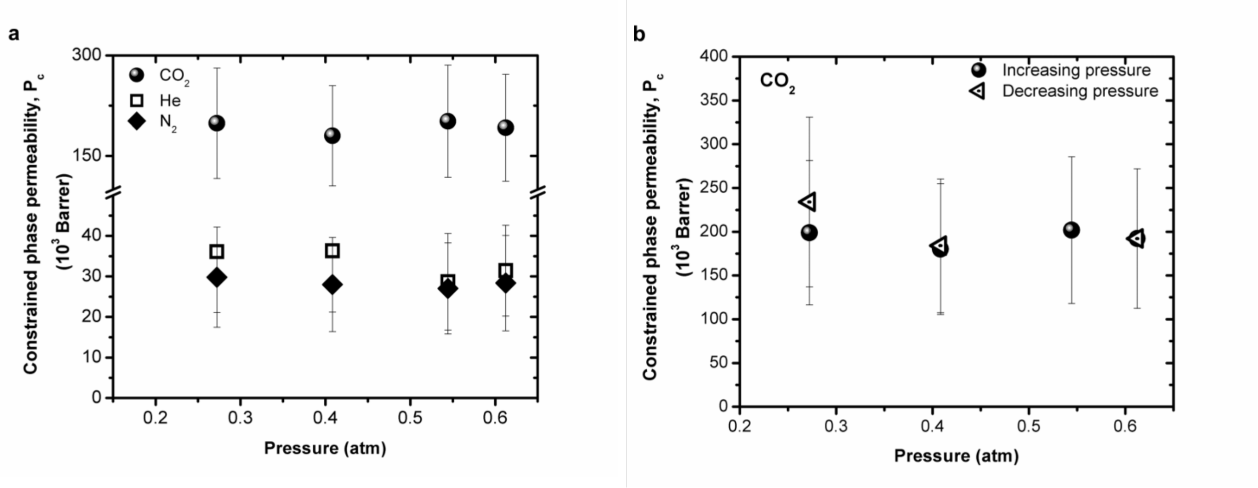

Figure 3.8: (a) Constrained phase permeabilities (P_C) of CO_2, helium, and nitrogen as function of upstream gas pressures. (b) Constrained phase permeabilities (P_c) of CO_2 measured in a cycle of increasing and decreasing upstream pressures.

Typically, sorbing gases like CO_2 exhibit pressure-dependent permeabilities in glassy polymeric bulk membranes at high gas pressures ($\Delta p > 1$ atm) that is usually described by the dual mode sorption (DMS) model.[31,33] The here found pressure independence of permeability in the low-pressure regime for CO_2 is in good agreement with the DMS model. The absence of any significant pressure-permeation hysteresis of CO_2 within the time frame of the experiment,

Figure 3.8 (b), indicates that AAO embedded PTMSP membranes are stable, i.e., do not show severe plasticization induced aging as found for ultra-thin film PTMSP membranes.[17]

From the permeabilities of single gas components, we deduced the membrane selectivities, i.e., $\alpha_{CO_2/He} = P_{CO_2} / P_{He}$ and $\alpha_{CO_2/N_2} = P_{CO_2} / P_{N_2}$. The average values are provided in Table **3-1** together with the permeability values. Table **3-1** reveals an increase in the CO_2/He selectivity from 4.7 in bulk membranes to that of 6.7 in the AAO confined PTMSP phase. A similar improvement over bulk values is also found for CO_2/N_2 selectivity from 4.8 to 6.9. The enhancement in the gas selectivity of CO_2 with respect to helium or nitrogen suggests that the free-volume elements are providing increased sorption sites for CO_2, benefiting CO_2 transport over the non-sorbing gases He and N_2. The selectivity values in the confined PTMSP phase are also improved over the free-standing thin film PTMSP membranes.

	Gas Permeability (10^3 Barrer)			**Relative Permeability (*P/P_b*)**			**Selectivity**	
	CO_2	**He**	**N_2**	**CO_2**	**He**	**N_2**	**CO_2/He**	**CO_2/N_2**
Bulk PTMSP	28 ± 5.5	5.9 ± 1.1	5.8 ± 1.1	1	1	1	4.7 ± 0.3	4.8 ± 0.3
Constrained PTMSP in AAO pores	187 ± 18	28 ± 1.7	27 ± 0.8	6.7	4.8	4.7	6.7 ± 0.2	6.9 ± 0.3
Planar confined PTMSP *750 nm film*[17]	117	27	-	4.2	4.6	-	4.3	-
Planar confined PTMSP *250 nm film*[17]	42.4	13.3	-	1.5	2.3	-	3.2	-

Table 3-1: Permeabilities, selectivities and relative permeabilities of CO_2, helium and nitrogen through interfacially and dimensionally constrained PTMSP, and bulk PTMSP membranes. Free-standing thin film values were obtained after 24 hours of drying, as described elsewhere.[17]

The data compilation in Table **3-1** shows for PTMSP comparable helium permeation values around 27,000 Barrer for both the 200 nm radially confined polymeric phase within AAO, and a free-standing 750 nm thin-film membrane. The four-fold permeability improvement in both confined systems over bulk PTMSP can be attributed to enhancements in the molecular mobilities of the polymeric phases that result from altered densities due to the confinement effects on the chain conformations.[34] The molecular mobility increase in PTMSP if interfacially confined was confirmed in thin-film studies and attributed to a free-volume increase.[17] Similar enhancements in free-volume have also been reported in AAO-constrained PTBA membranes [27], and nanoparticle-based composites of PTMSP.[5,8]

Looking back at Figure 3.1, it was argued for a comparable dimensional parameter ξ between thin-film and nanoporous confined membrane systems, which is in contrast to the 750 nm and 200 nm confinements of PTMSP respectively. However one has also to weigh in, besides the dimensional constraints, the history of the material, i.e., the solvent residence (evaporation) time during the annealing process. The structure of the solid condensed phase of PTMSP with its bulky side-groups and rigid conjugated backbones can be expected to be strongly dependent on how fast the solvent evaporates. The thin free-standing PTMSP film possesses an evaporation area/thickness ratio that exceeds the one of the AAO confined phase by about two orders of magnitude. Thus we conclude that the AAO confined phase had more time to anneal towards its bulk equilibrium structure, than the thin film, yielding a confining dimensional parameter ξ that can only be matched by thicker free-standing films.

Temporal stability of the membranes is a critical parameter to evaluate the performance of the membranes. We have evaluated the aging performance of an AAO-confined PTMSP membrane by measuring the gas permeabilities of helium and nitrogen over 15 days and compared it with the aging behavior of a thick unconfined PTMSP film (Figure 3.9). Figure 3.9(a) contrasts the helium permeability of an AAO-confined PTMSP phase, P_c, to that of an unconfined thick membrane and of an ultrathin PTMSP film. In the initial phase, (first measurement taken after 24 hours of membrane preparation), the permeabilities of both AAO-confined PTMSP and free-standing thin film PTMSP exceed the bulk PTMPS value four-fold. Over the first 24 hours, the thin film membrane aged dramatically, loosing all its initial transport advantages over the bulk system. The origin for the fast aging process in thin-film PTMSP was attributed to free-volume collapse.[17] A continued study over 15 days showed a significantly extended high-permeation lifespan for the cylindrically confined AAO system. From slopes of the aging data, one can infer an approximate twenty-fold temporal stability improvement of the AAO cylindrical arrangement over thin-film membranes for PTMSP. We can conclude that both the limited free surface exposure and the stability provided by the AAO interface are the cause for a significantly delayed free-volume collapse in AAO confined PTMSP. The temporal stability of AAO confined and bulk PTMSP towards N_2 permeation was also analyzed, Figure 3.9 (b). While again a reduction in permeability is more prominent for N_2 through the dimensionally confined system, the rate of aging is faster compared to helium. A similar observation was made by Dorkenoo et al [35], who found an accelerated reduction in nitrogen permeabilities in comparison to helium in 1 µm-thick PTMSP films. It was proposed that the retardation/collapse of free-volume elements in thin films impact nitrogen permeation more than that of helium.

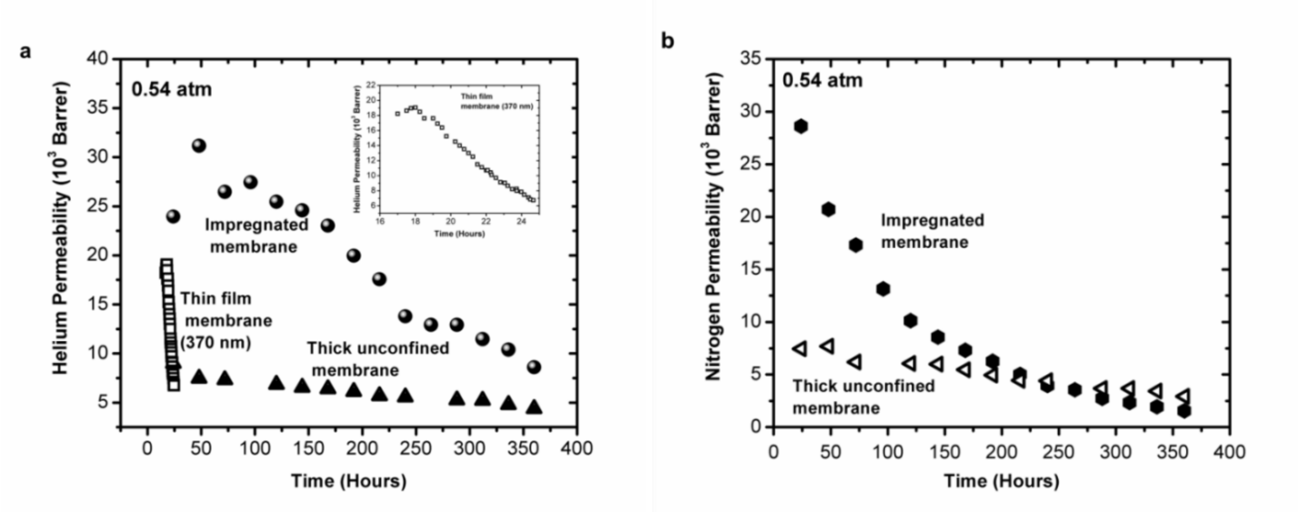

Figure 3.9: Gas permeability coefficients of (a) helium and (b) nitrogen through the constrained polymeric phase of AAO confined PTMSP evaluated as a function of aging time. The aging behavior of thin PTMSP (370 nm) membranes is shown in the inset of Figure 3.9 (a)[17]. The aging behavior of these membranes is contrasted to that of bulk-unconfined membranes.

3.3.2 PEO-AAO hybrid membranes

The SEM image of the cross section of AAO membrane impregnated with PEO is shown in Figure 3.10. Cylindrical nanostructures of PEO that stretch through the entire length of the AAO membrane were evident. The solution impregnation method leaves a remnant bulk PEO layer which can also be seen on the top of AAO membrane (Figure 3.10). The transport properties of unconfined micrometer-thick pristine bulk PEO membranes were investigated for comparative studies to the PEO-AAO hybrid membranes. The bulk membranes were fabricated by drop casting PEO films on spin casted PTMSP films on AAO membranes (as described in the experimental section). Thereby, AAO served as support, revealing no measurable polymer impregnation.

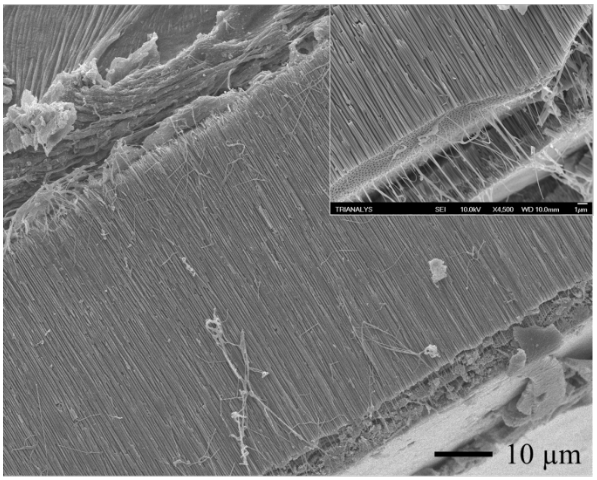

Figure 3.10: SEM image of the cross-section of PEO-AAO hybrid membrane. A top remnant bulk PEO layer can be seen on the top surface of AAO membrane. The inset reveals the close-up view of the PEO cylindrical nanostructures.

As mentioned in the experimental section, the constant volume variable pressure method[10] was used to measure the gas permeation rates. The gas flux was measured from the rate of permeating gas pressure rise in the downstream chamber of the membrane housing due to the applied pressure gradient across the membrane. The rate of increase in the penetrant gas pressure of helium and CO_2 through a bulk PEO membrane is shown in Figure 3.11(a). The gas permeabilities were obtained from the rate of pressure rise utilizing equation (3.1). The thickness of PEO film on AAO membrane support was 1.6 μm.

The permeability of helium and CO_2 through thick unimpregnated PEO membranes were found to be 1.8 Barrer and 12 Barrer respectively which are in good agreement with the literature values.[10] The selectivity of CO_2/He is 6.67 (Table 3-2). The gas permeation rate through impregnated PEO-AAO hybrid membrane is shown in Figure 3.11(b). The hybrid membrane had a top remnant PEO bulk layer (3.0 μm) resulting from the impregnation process. Comparable gas fluxes of helium and CO_2 between the impregnated and unconfined PEO films (Figure 3.11 (a) & (b)) represented by the slopes, indicate that the AAO pores were not fully filled with PEO. If the

AAO membrane were fully filled with PEO, the gas flux is expected to be around 60 times lower than the flux of the unconfined membrane, since the thickness of the PEO phase would then be equivalent to the thickness of AAO membrane (~60 μm thick). This suggests that up on impregnation, PEO forms nanotubes instead of solid rods inside the pores of the AAO membrane as illustrated in Figure 3.12. Formation PEO nanorods in AAO templates has been widely reported [36,37].

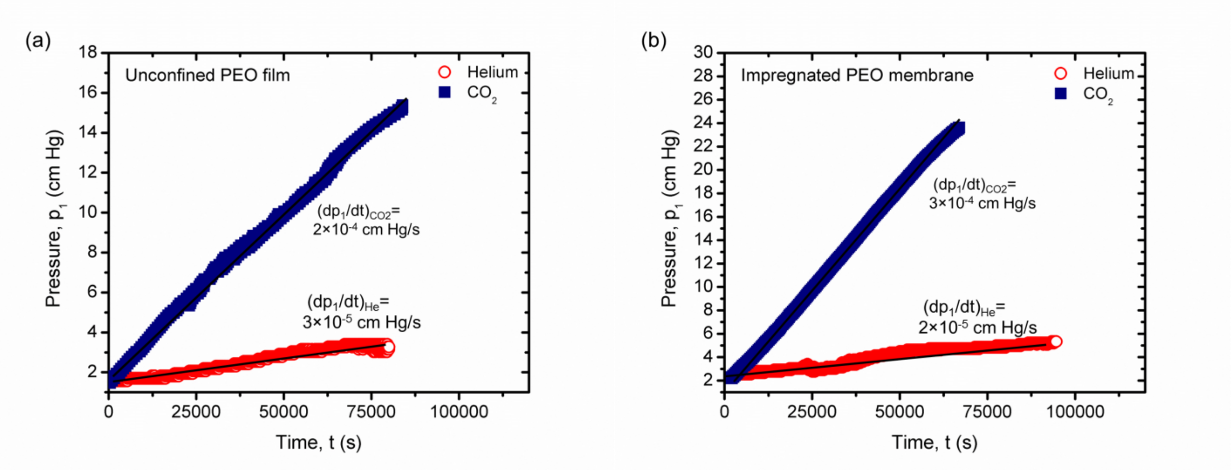

Figure 3.11: Gas permeation rates of CO_2 and helium through (a) Unconfined PEO membrane (b) Impregnated PEO membrane

The permeability through the PEO-AAO hybrid membrane was obtained from Figure 3.11(b) utilizing equation (3.1). The film thickness of gas permeation (L) is assumed to be equivalent to the thickness of the top remnant PEO layer since this layer offers major resistance to gas transport. The comparison of the permeabilities between the bulk unconfined PEO membrane and that of the AAO-hybrid membrane are shown in Table 3-2. It can be seen that while the apparent permeability of helium in impregnated PEO membrane is lower than the bulk film by ~34%, the CO_2 permeation is 45% higher. Subsequently the reverse selectivity is enhanced from 6.7 to 15 in the hybrid membranes.

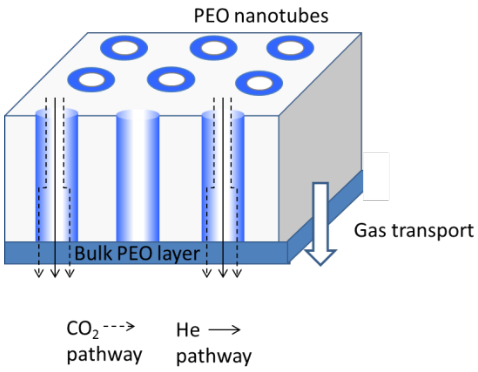

Figure 3.12: Schematic of gas transport through hybrid PEO-AAO membrane

This enhanced permeability of CO_2 over helium in PEO-AAO hybrid membrane indicates that though the gas transport is primarily influenced by the top layer, the PEO nanotubes impact the transport of a strongly sorbing gas like CO_2, which could preferentially adsorb on to the PEO coated pore walls and be transported by a complimentary surface diffusion mechanism in addition to the flow through the open conduits (Figure 3.12). On the other hand helium transport is not influenced by the PEO coated walls owing to its non-sorbing behavior. Thus it can be seen that this PEO-AAO hybrid membrane configuration facilitates enhanced gas selective transport of CO_2 over helium.

	Top bulk layer thickness (µm)	**Permeability (Barrer)**		**Reverse selectivity ($\alpha_{CO2/He}$)**
		Helium	CO_2	
Bulk PEO film	1.6	1.8	11.9	6.67
PEO-AAO hybrid membrane	3.0	1.15	17.4	15

Table 3-2: Gas permeabilities of helium and CO_2 through bulk and impregnated PEO membrane.

3.4 Conclusions

The initial superior gas permeation properties for CO_2 and helium observed in free-standing ultrathin PTMSP membranes could be translated successfully into hybrid AAO-PTMSP membranes. The constrained AAO impregnated PTMSP phase exhibited a four-fold permeability increase for CO_2, helium and nitrogen, and a 40% improvement of the reverse selectivity of CO_2 over non- sorbing gases (CO_2/He, CO_2/N_2) in comparison to bulk PTMSP membranes. Furthermore, the temporal stability in AAO embedded PTMSP was found to be improved substantially by a factor of 20 over its thin-film counterparts. The increase in the transport and separation properties were attributed, in accordance to prior film studies, to interfacially and dimensionally induced enhancement of the free-volume in the confined phase of PTMSP. A dimensional comparison of equally effective transport properties in thin film vs. AAO confined PTMSP yielded a ~750 nm thin film to perform similarly as a 200 nm AAO confined PTMSP phase. The difference in size of the confining dimensional parameter was attributed to the sluggish relaxation of PTMSP, and the solvent residence time (evaporation time), which if scaled by the free surface is by two orders of magnitude larger in thin films as compared to AAO embedded PTMSP. An enhanced gas selectivity of CO_2/He was observed in AAO-PEO nanohybrid membranes though the gas permeabilities were comparable to bulk PEO membranes indicating that the gas transport is controlled by the top bulk PEO layer but the CO_2 permeation took place through a parallel surface sorption and diffusion mechanism through the PEO coated pore walls.

Overall, the incorporation of polymer into nanoporous membranes provides similar interfacial constraints, and with it enhancement in transport properties, as found in interfacially constrained systems of thin films or particle embedded nanocomposites. The benefits of polymer hybrid systems include enhanced mechanical and temporal stability, and avoidance of undesired interstitial transport caused by particle aggregation, as found in nanocomposites [6,8]. In our on-going studies our focus is on the appropriate functionalization of alternative nanoporous templates for polymer injection, and the effective removal of ad-layers at the outside of the porous membranes.

3.5 References

(1) Chung, T. S.; Jiang, L. Y.; Li, Y.; Kulprathipanja, S. *Prog. Polym. Sci.* **2007**, *32*, 483-507.
(2) Kim, J. H.; Lee, Y. M. *Journal of Membrane Science* **2001**, *193*, 209-225.
(3) Merkel, T. C.; Freeman, B. D.; Spontak, R. J.; He, Z.; Pinnau, I.; Meakin, P.; Hill, A. J. *Science* **2002**, *296*, 519-522.
(4) He, Z. J.; Pinnau, I.; Morisato, A. *Desalination* **2002**, *146*, 11-15.
(5) Merkel, T. C.; He, Z. J.; Pinnau, I.; Freeman, B. D.; Meakin, P.; Hill, A. J. *Macromolecules* **2003**, *36*, 6844-6855.
(6) Matteucci, S.; Kusuma, V. A.; Sanders, D.; Swinnea, S.; Freeman, B. D. *Journal of Membrane Science* **2008**, *307*, 196-217.
(7) Matteucci, S.; Kusuma, V. A.; Kelman, S. D.; Freeman, B. D. *Polymer* **2008**, *49*, 1659-1675.
(8) De Sitter, K.; Winberg, P.; D'Haen, J.; Dotremont, C.; Leysen, R.; Martens, J. A.; Mullens, S.; Maurer, F. H. J.; Vankelecom, I. F. J. *Journal of Membrane Science* **2006**, *278*, 83-91.
(9) Brunetti, A.; Scura, F.; Barbieri, G.; Drioli, E. *Journal of Membrane Science*, *359*, 115-125.
(10) Lin, H.; Freeman, B. D. *Journal of Membrane Science* **2004**, *239*, 105-117.
(11) Bondar, V. I.; Freeman, B. D.; Pinnau, I. *Journal of Polymer Science Part B-Polymer Physics* **2000**, *38*, 2051-2062.
(12) Bondar, V. I.; Freeman, B. D.; Pinnau, I. *Journal of Polymer Science Part B-Polymer Physics* **1999**, *37*, 2463-2475.
(13) Okamoto, K.; Fujii, M.; Okamyo, S.; Suzuki, H.; Tanaka, K.; Kita, H. *Macromolecules* **1995**, *28*, 6950-6956.
(14) Baschetti, M. G.; Ghisellini, M.; Quinzi, M.; Doghieri, F.; Stagnaro, P.; Costa, G.; Sarti, G. C. *Journal of Molecular Structure* **2005**, *739*, 75-86.
(15) Yave, W.; Car, A.; Funari, S. S.; Nunes, S. P.; Peinemann, K. V. *Macromolecules* **2010**, *43*, 326-333.
(16) Bansal, A.; Yang, H. C.; Li, C. Z.; Cho, K. W.; Benicewicz, B. C.; Kumar, S. K.; Schadler, L. S. *Nature Materials* **2005**, *4*, 693-698.
(17) Kocherlakota, L. S.; Knorr, D. B.; Foster, L.; Overney, R. M. *Polymer* **2012**, *53*, 2394-2401.

(18) Sen, S.; Xie, Y.; Bansal, A.; Yang, H.; Cho, K.; Schadler, L. S.; Kumar, S. K. *European Physical Journal-Special Topics* **2007**, *141*, 161-165.
(19) Yave, W.; Car, A.; Wind, J.; Peinemann, K. V. *Nanotechnology* **2010**, *21*.
(20) Horn, N. R.; Paul, D. R. *Polymer* **2011**, *52*, 1619-1627.
(21) Horn, N. R.; Paul, D. R. *Polymer* **2011**, *52*, 5587-5594.
(22) Xia, J. Z.; Chung, T. S.; Li, P.; Horn, N. R.; Paul, D. R. *Polymer* **2012**, *53*, 2099-2108.
(23) Steinhart, M.; Wendorff, J. H.; Greiner, A.; Wehrspohn, R. B.; Nielsch, K.; Schilling, J.; Choi, J.; Gosele, U. *Science* **2002**, *296*, 1997-1997.
(24) Martin, J.; Mijangos, C. *Langmuir* **2009**, *25*, 1181-1187.
(25) Feng, X. D.; Jin, Z. X. *Macromolecules* **2009**, *42*, 569-572.
(26) Zhang, M. F.; Dobriyal, P.; Chen, J. T.; Russell, T. P.; Olmo, J.; Merry, A. *Nano Letters* **2006**, *6*, 1075-1079.
(27) Killgore, J. P.; Kocherlakota, L. S.; Overney, R. M. *Journal of Polymer Science Part B-Polymer Physics* **2010**, *48*, 434-441.
(28) Ku, A. Y.; Ruud, J. A.; Early, T. A.; Corderman, R. R. *Langmuir* **2006**, *22*, 8277-8280.
(29) Pinnau, I.; Wijmans, J. G.; Blume, I.; Kuroda, T.; Peinemann, K. V. *Journal of Membrane Science* **1988**, *37*, 81-88.
(30) Kimmerle, K.; Hofmann, T.; Strathmann, H. *Journal of Membrane Science* **1991**, *61*, 1-17.
(31) Merkel, T. C.; Bondar, V.; Nagai, K.; Freeman, B. D. *Journal of Polymer Science Part B-Polymer Physics* **2000**, *38*, 273-296.
(32) Pinnau, I.; Toy, L. G. *Journal of Membrane Science* **1996**, *116*, 199-209.
(33) Srinivasan, R.; Auvil, S. R.; Burban, P. M. *Journal of Membrane Science* **1994**, *86*, 67-86.
(34) Shin, K.; Obukhov, S.; Chen, J. T.; Huh, J.; Hwang, Y.; Mok, S.; Dobriyal, P.; Thiyagarajan, P.; Russell, T. P. *Nature Materials* **2007**, *6*, 961-965.
(35) Dorkenoo, K. D.; Pfromm, P. H. *Macromolecules* **2000**, *33*, 3747-3751.
(36) Maiz, J.; Martin, J.; Mijangos, C. *Langmuir* **2012**, *28*, 12296-12303.
(37) Michell, R. M.; Blaszczyk-Lezak, I.; Mijangos, C.; Muller, A. J. *Polymer* **2013**, *54*, 4059-4077.

Chapter 4

Investigation of Molecular Conformations in Zwitterionic Polymer Brushes

4.1 Introduction

Non-specific protein and biomolecular adsorption is a major challenge in several biological applications ranging from medical implants,[1] biomedical devices,[2] drug delivery carriers[3] to marine applications.[4] Even small amounts of proteins on surfaces are sufficient to cause propagation of unwanted fouling. For instance, as little as 7 ng/cm^2 fibrinogen was found to induce full-scale blood platelet adhesion.[5] Typical non-fouling coatings aim to minimize the intermolecular forces of interaction between the biomolecules like proteins and the surface of interest. The interfacial energy between the surface and water is found to be critical in conferring non-fouling properties to the surface.[6] Hydrophobic surfaces possess high interfacial energy with respect to water, and consequentially amphiphillic molecules like proteins adsorb on their surface to minimize the interfacial energy. On the other hand, hydrophilic surfaces with low interfacial energy with water, are not thermodynamically favored for the adsorption of proteins as the interfacial energy of the surfaces are already sufficiently low.[6]

Poly(ethylene glycol) (PEG)[7] and oligo(ethylene glycol) (OEG)[8] based coatings are widely used for the prevention of non-specific protein adsorption. Studies on self-assembled monolayers of oligo(ethylene glycol) (OEG) reveal that surface hydration[9-11] due to bound water layer around the OEG chains as well as the conformational flexibility of the ethylene glycol chains are responsible for the prevention of protein adsorption.[8] PEG and other hydrophilic materials like tetraglyme, dextran and mannitol achieve surface hydration due to hydrogen bonding.[12] Zwitterionic polymers represent another special class of materials that have been shown to exhibit ultra-low fouling properties in several biomedical applications.[13-16] Random distribution of positive and negative charge residues on proteins lead to a higher susceptibility of their adsorption on both positive and negatively charged surfaces. Polyzwitterionic coatings are effective in preventing the adsorption of proteins due to their nanoscale homogeneous mixture of balanced charge groups.[17,18]

Polyampholytes are macromolecular entities which bear, at the same time, positive and negative charges on distinct monomers.[19] Polyzwitterions are a special class of polyampholytes where each monomer carries both the positive and negative charges (Figure 4.1). Sulfonate-betaines (SB), carboxylate betaines (CB) and phosphonate betaines (PB) are some examples of polyzwitterions which are extensively studied for non-fouling coatings. These molecules bind water very strongly due to electrostatically induced hydration, which forms a physical and energetic barrier to prevent protein adsorption on the surface.[13,14] The strength of surface hydration is primarily determined by physico-chemical properties of these materials like molecular weight, surface chemistry and their surface packing, i.e film thickness, packing density[16] and chain conformations.

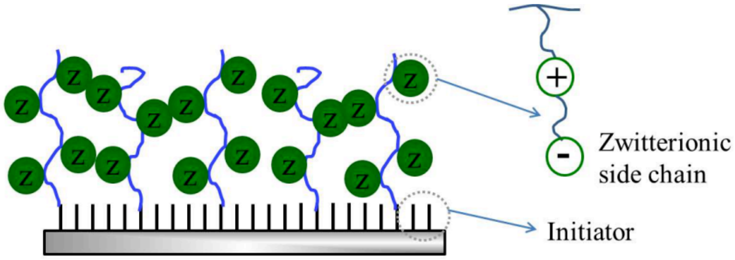

Figure 4.1: Schematic of polyzwitterionic brushes grafted on to a substrate

In the pursuit of developing "zero" protein adsorption surfaces in complex biological media such as undiluted blood serum and plasma, Jiang et al found that surface resistance to protein adsorption was dependent on the film thickness of the polyzwitterionic brushes, pSB [20] and pCB[21]. A minimum in protein adsorption from 100% blood serum was evident in films of optimum thickness around 62 and 20 nm of pSB and pCB respectively. It was suggested that while thinner zwitterionic brushes might not form dense enough brushes to resist protein adsorption from complex media like blood serum, thicker brushes could self-associate due to inter-chain or intra-chain molecular interactions and weaken surface hydration leading to high protein adsorption.

Dry film refractive index which is proportional to the polymer density was shown to be another engineering parameter analogous to the film thickness for controlling the protein adsorption.[22] Furthermore it has been shown that the packing density of polymer chains is directly related to the swelling ratios of the swollen to the collapsed film thickness in the relevant solution media.[16] From a fundamental perspective, the surface hydration and subsequently the non-fouling properties of the zwitterionic polymeric brushes are related to the molecular conformations which depend on the intricate interplay of the inter and intramolecular dipole interactions. It has been shown that the extremely high dipole moment of the zwitterionic groups (around 23 D for pSB brushes) gives rise to self-association of polymer chains owing to strong inter and intra-molecular associations.[23,24]

The objective of the present study was to investigate the thermal relaxations via a transition analysis of pSB, pCB brushes to gain insights into the molecular conformation of the polymeric brushes. Specifically, we present transition analyses conducted on poly(sulfobetaine methacrylate)(pSBMA), poly(carboxybetaine acrylamide) (pCBAA), and compare the results to poly(oligo(ethylene glycol) methyl methacrylate) (PEGMA) brushes.

4.2 Experimental

Polymeric brushes of pSBMA, pCBAA and PEGMA were surface grafted on silicon wafers by surface initiated-atom transfer radical polymerization (SI-ATRP) following the procedures described in detail elsewhere.[22,25,26] The chemical structures of the brushes are shown in Figure 4.2. The thermo-mechanical analysis of the pSBMA, pCBAA and PEGMA brushes was performed by Shear Modulation-Force Microscopy (SM-FM)[27] which is discussed in detail in the Experimental Techniques Chapter (Chapter 6). SM-FM provides critical temperature values that are indicative of possible phase changes or more subtle mobilities within the material phase. In polymers, critical temperature values pinpoint to transitions caused, for instance, by side-chain relaxations or backbone relaxations (glass transition). This method has been employed, for instance, to reveal structural transitions in Nafion, a polyelectrolyte membrane material.[28] Similarly the phase transitions in poly(NIPAM) brushes were evidenced by the SMFM measurement which coincided with the lower critical solution temperature (LCST).[29]

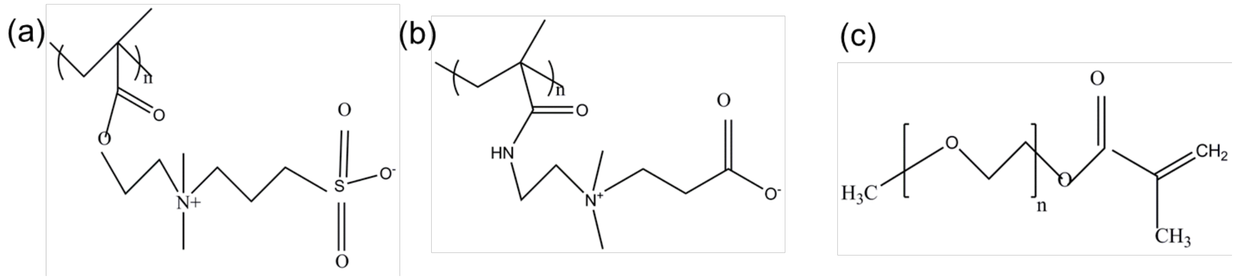

Figure 4.2: Chemical structures of (a) pSBMA (b) pCBAA (c) PEGMA

4.3 Results and Discussion

Figure 4.3 (a) shows the contact stiffness of 16 nm thick pSBMA sample measured as a function of temperature. Reversible critical transition temperatures around 74 °C evidenced as a kink in the contact stiffness were found in two subsequent runs (Run 1 & 2). Transition temperature measurement of another fresh sample of similar thickness (sample 2), which was heated in vaccum oven for three hours at 90 °C, revealed an elevation of the transition point of 85 °C. For a thicker pSBMA sample of 27 nm the transition temperature was found to be shifted to 60 °C and this difference could be attributed to the differences in the molecular weight of the polymer manifested as film thickness.

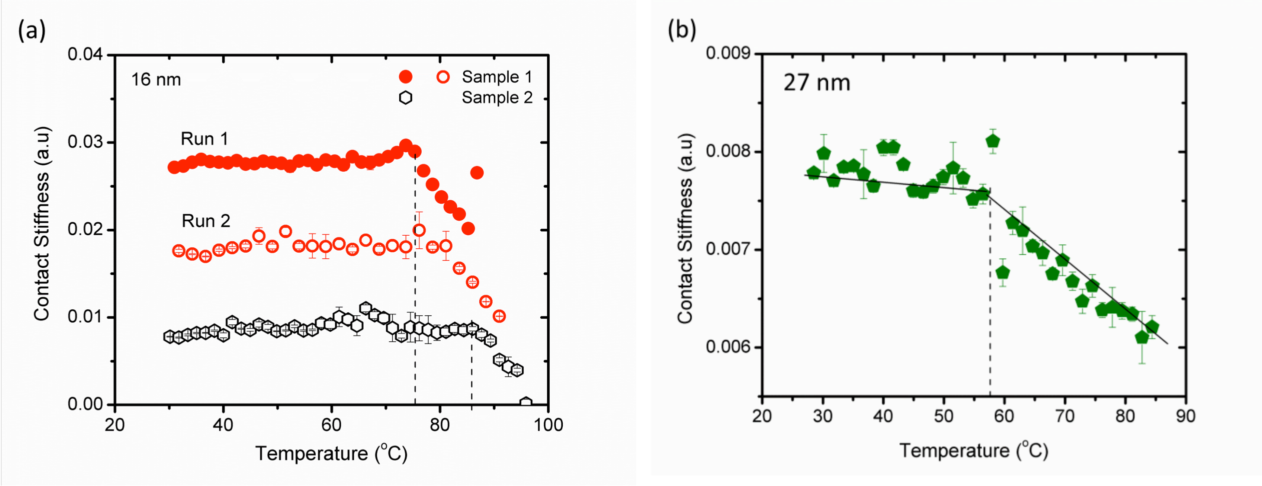

Figure 4.3 (a) Transition temperature of 16 nm thick pSBMA brushes (Sample 1) measured in two repeated runs (Run 1 & 2). Transition temperature of the another fresh sample of same thickness (Sample 2) after it is heated under vaccum at 90°C for three hours. (b) Transition temperature of 27 nm thick pSBMA brush sample. All measurements were performed at low humidity (<10%)

Extremely high dipole moment of zwitterionic groups (around 23 D [23,24]) in sulfobetaines was shown to give rise to reversible self-association molecular states, as a consequence of strong inter and intramolecular dipolar interactions which are sensitive to temperature.[30] The schematic of different possible molecular associations of zwitterionic brushes are shown in Figure 4.4. In a solution, sulfobetaines are shown to exhibit both an upper critical solution temperature (UCST) as well as an 'apparent inverted' lower critical solution temperature (LCST).[31] UCST is the highest temperature above which the inter and intra-molecular dipolar interactions are broken to yield isolated polymer chains that are highly solvated and thus miscible in solution. In aqueous solution this would mean that the polymeric chains are in extended state with reduced intra-chain associations.

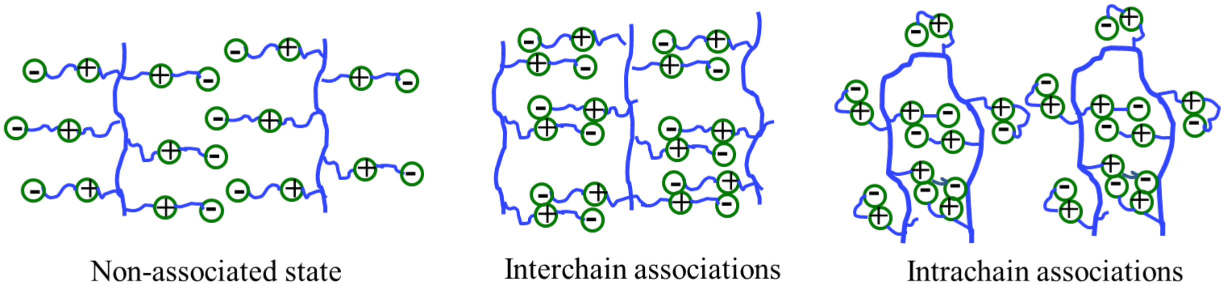

Figure 4.4: Schematic of different possible conformational states of polyzwitterionic brushes.

Analogous thermal transitions have also been observed in polysulfobetaine brushes grown on silicon and gold. An intriguing transition thickness was evidenced in poly[2-(methacryloyloxyl)ethyl]dimethyl(3-sulfopropyl)ammonium hydroxide (poly MEDSAH), a sulfobetaine polymeric brush, which transitioned from hydrophilic to hydrophobic state.[30] It was suggested that beyond a critical thickness, the polymeric brushes collapse from a non-associated and hydrophilic state to a super-collapsed hydrophobic state owing to the inter and intra chain associations. Furthermore thick poly(MEDSAH) (~200 nm) brushes showed a reversible wetting transition at 60^{o}C, where the films transitioned between relatively hydrophobic (advancing contact angle θ=60^{o}C), dehydrated state at room temperatures to a hydrated, hydrophilic (contact angle θ=20^{o}C) state, analogous to the UCST behavior.[30] The magnitude of the contact angle change was found to depend strongly on the grafting density.[32] However in the present study, the pSBMA samples were initially hydrophilic with the contact angles between 5-10^{o}. This indicates that in their initial state the polymeric brushes are in an extended state with very little intra molecular interactions. This configuration is expected, since at higher graft densities, the chances for brushes to fold back and have contact within its components are low thus restricting intramolecular associations.

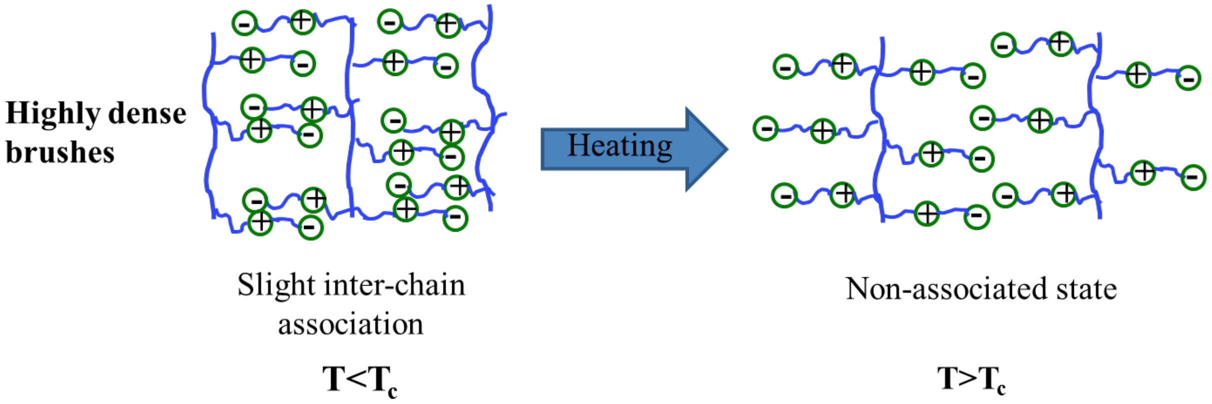

Figure 4.5: Schematic of molecular conformation of pSBMA brushes before and after critical transition temperature

Upon heating, the molecular mobility of the polymeric chains increases conforming from an inter-molecular associated state into a 'non-associated' hydrophilic state as shown in Figure 4.5. This behavior would be similar to the UCST transition reported for polysulfobetaines in solution.[31] The observed changes in molecular conformations indicate that the anti-fouling properties of pSBMA would be dependent on the temperature. Furthermore pSBMA could potentially be used as a thermo-responsive material utilizing its reversible thermal transitions in the molecular conformations.

The thermal transition behavior of pCBAA and PEGMA brushes of comparable thickness as the pSBMA brushes investigated is shown in Figure 4.6. No apparent transition behavior was found in the pCBAA films in the temperature range investigated (Figure 4.6). These brushes were hydrophilic to begin with and from the absence of any thermal transitions, it can be concluded that these films do not undergo any conformational changes and continue to remain hydrophilic in the temperature regime of 30 °C to 80 °C. No clear transition behavior was seen in PEGMA films as well (Figure 4.6(b)). Previous studies on solution properties of PEGMA revealed LCST at 90 °C.[33] There is a possibility that in the present case the PEGMA brushes could exhibit transition behavior changing from 'hydrophilic' state to a collapsed 'hydrophobic state' at temperatures greater than the range we have investigated (>100°C).

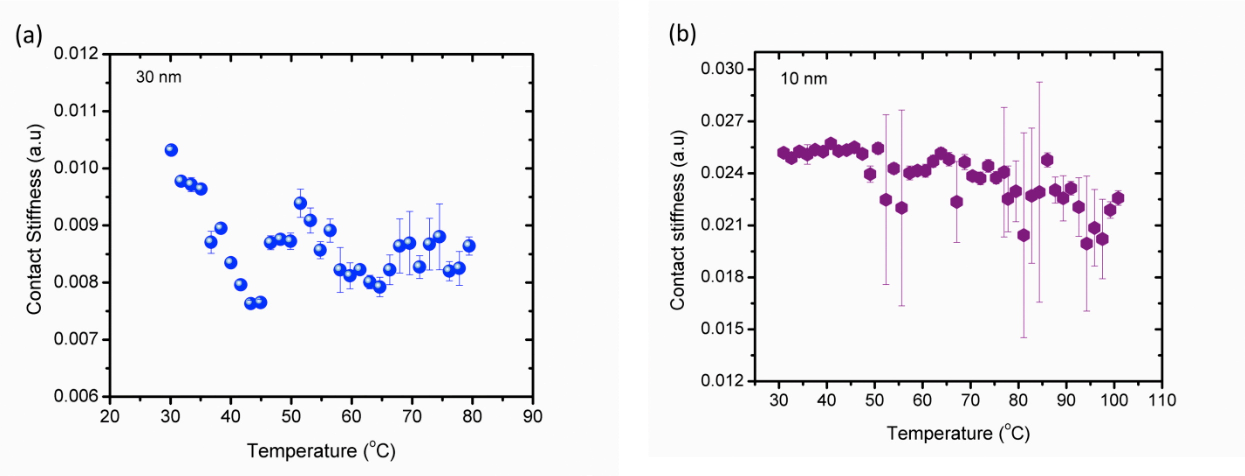

Figure 4.6: Thermal transition analysis of (a) pCBAA brushes and (b) PEGMA brushes grown on silicon substrate.

4.4 Conclusions

In this work the thermal transitions of pSBMA, pCBAA and pEGMA brushes were investigated to gain insights into their molecular conformations. pSBMA brushes showed a critical transition temperature of 60-75°C in 27 and 16 nm films respectively analogous to the critical solution temperature behavior of the sulfobetaines. We hypothesized that upon heating the polymeric brushes, which are initially in slightly extended state due to intermolecular associations, transition into a 'non associated state'. Owing to the reversible nature of the transition behavior observed, these brushes could be potentially used as thermo-sensitive materials. No changes were observed in the molecular conformations of pCBAA films in the same temperature regime, indicating that pCBAA is stable over this temperature change and hence no changes in their ultra-low fouling properties would be expected. Similarly no thermal transitions were evidenced in PEGMA films in the present range of temperature.

4.5 References

(1) Ratner, B. D.; Bryant, S. J. *Annual Review of Biomedical Engineering* **2004**, *6*, 41-75.
(2) Prime, K. L.; Whitesides, G. M. *Science* **1991**, *252*, 1164-1167.
(3) Langer, R. *Science* **2001**, *293*, 58-59.
(4) Callow, J. A.; Callow, M. E. *Nat. Commun.* **2011**, *2*.
(5) Tsai, W. B.; Grunkemeier, J. M.; Horbett, T. A. *Journal of Biomedical Materials Research* **1999**, *44*, 130-139.
(6) Krishnan, S.; Weinman, C. J.; Ober, C. K. *Journal of Materials Chemistry* **2008**, *18*, 3405-3413.
(7) McPherson, T.; Kidane, A.; Szleifer, I.; Park, K. *Langmuir* **1998**, *14*, 176-186.
(8) Li, L. Y.; Chen, S. F.; Zheng, J.; Ratner, B. D.; Jiang, S. Y. *Journal of Physical Chemistry B* **2005**, *109*, 2934-2941.
(9) He, Y.; Chang, Y.; Hower, J. C.; Zheng, J.; Chen, S.; Jiang, S. *Physical Chemistry Chemical Physics* **2008**, *10*, 5539-5544.
(10) Zheng, J.; Li, L. Y.; Chen, S. F.; Jiang, S. Y. *Langmuir* **2004**, *20*, 8931-8938.
(11) Zheng, J.; Li, L. Y.; Tsao, H. K.; Sheng, Y. J.; Chen, S. F.; Jiang, S. Y. *Biophysical Journal* **2005**, *89*, 158-166.
(12) Jiang, S.; Cao, Z. *Advanced Materials* **2010**, *22*, 920-932.
(13) Chen, S. F.; Zheng, J.; Li, L. Y.; Jiang, S. Y. *Journal of the American Chemical Society* **2005**, *127*, 14473-14478.
(14) He, Y.; Hower, J.; Chen, S.; Bernards, M. T.; Chang, Y.; Jiang, S. *Langmuir* **2008**, *24*, 10358-10364.
(15) Huang, C. J.; Li, Y. T.; Jiang, S. Y. *Analytical Chemistry* **2012**, *84*, 3440-3445.
(16) Huang, C. J.; Li, Y. T.; Krause, J. B.; Brault, N. D.; Jiang, S. Y. *Macromolecular Rapid Communications* **2012**, *33*, 1003-1007.
(17) Chen, S.; Li, L.; Zhao, C.; Zheng, J. *Polymer* **2010**, *51*, 5283-5293.
(18) Chen, Y.; Thayumanavan, S. *Langmuir* **2009**, *25*, 13795-13799.
(19) Ladenheim, H.; Morawetz, H. *Journal of Polymer Science* **1957**, *26*, 251-254.
(20) Liu, X.; Yang, J. W.; Lynn, D. M. *Biomacromolecules* **2008**, *9*, 2063-2071.
(21) Yang, W.; Zhang, L.; Wang, S.; White, A. D.; Jiang, S. *Biomaterials* **2009**, *30*, 5617-5621.
(22) Brault, N. D.; Sundaram, H. S.; Li, Y.; Huang, C.-J.; Yu, Q.; Jiang, S. *Biomacromolecules* **2012**, *13*, 589-593.
(23) Bredas, J. L.; Chance, R. R.; Silbey, R. *Macromolecules* **1988**, *21*, 1633-1639.

(24) Galin, M.; Chapoton, A.; Galin, J. C. *Journal of the Chemical Society-Perkin Transactions 2* **1993**, 545-553.

(25) Yang, W.; Chen, S.; Cheng, G.; Vaisocherova, H.; Xue, H.; Li, W.; Zhang, J.; Jiang, S. *Langmuir* **2008**, *24*, 9211-9214.

(26) Ma, H. W.; Li, D. J.; Sheng, X.; Zhao, B.; Chilkoti, A. *Langmuir* **2006**, *22*, 3751-3756.

(27) Sills, S.; Overney, R. M.; Chau, W.; Lee, V. Y.; Miller, R. D.; Frommer, J. *J. Chem. Phys.* **2004**, *120*, 5334-5338.

(28) Wei, J. H.; He, M. Y.; Overney, R. M. *Journal of Membrane Science* **2006**, *279*, 608-614.

(29) Overney, R. M.; Buenviaje, C.; Luginbuhl, R.; Dinelli, F. *Journal of Thermal Analysis and Calorimetry* **2000**, *59*, 205-225.

(30) Azzaroni, O.; Brown, A. A.; Huck, W. T. S. *Angew. Chem.-Int. Edit.* **2006**, *45*, 1770-1774.

(31) Schulz, D. N.; Peiffer, D. G.; Agarwal, P. K.; Larabee, J.; Kaladas, J. J.; Soni, L.; Handwerker, B.; Garner, R. T. *Polymer* **1986**, *27*, 1734-1742.

(32) Cheng, N.; Brown, A. A.; Azzaroni, O.; Huck, W. T. S. *Macromolecules* **2008**, *41*, 6317-6321.

(33) Lutz, J. F.; Hoth, A. *Macromolecules* **2006**, *39*, 893-896.

Chapter 5

Local Energetic Analysis of the Surface Energies for Graphene from the Single Layer to Graphite

5.1 Introduction

Graphene, the atomic lamellar building block of graphite, excites scientific interest, owing to its exceptional electronic and mechanical properties, its exotic nature as a two-dimensional atomic crystal, and diverse applications in electronic, photonic, photovoltaic, electrochemical, and sensing devices.[1] Being employed in composites, in electrodes, transparent coatings, and in other lamellar designs [2-11], the surface properties of graphene are of critical importance. Chemical treatments and surface functionalization in the many routes of production for graphene and its derivatives have been found to exert a profound effect on the surface energy of graphene, thereby opening up multifarious opportunities for surface engineering of graphene-based devices.[12-16]

Thus, while the surface energy of graphene is regarded pivotal in the design of novel functional materials, its determination is still eluding us. Current efforts in determining the surface energy of graphene remain disputed.[17,18] To this end, we herein employ a microscopic technique that provides direct access to the surface energy, i.e., more precisely, the Hamaker constant. The aim of this work is to investigate the surface energy of graphene as a function of the layer number, from the monolayer up to bulk graphite. This involves a local energetic analysis, specifically an atomic force microscope (AFM), where AFM tip scattering on active modes specific to the materials involved, is Arrhenius analyzed. This methodology, known as Intrinsic Friction Analysis (IFA), has been prior to this study successfully utilized in the analysis of the energetics of thermally active rotational and translational modes in organic systems.[19-21]

IFA is here for the first time employed to analyze dipolar fluctuation modes that are responsible for the van der Waals dispersion interaction.

5.2 Experimental

IFA experiments were performed with an AFM (*Explorer*, Veeco Inc., CA) with an integrated custom heating stage using a contact mode silicon lever (PPT-CONT, Nanosensors, nominal and lateral spring constants of ~ 0.2 N/m and 80 N/m, respectively) at atmospheric pressure. The SFM tip was preconditioned by chemical-mechanical polishing including a spring constants calibration.[19] IFA technique is further elaborated in Experimental Techniques Chapter (Chapter 6). All measurements were performed under dry nitrogen atmosphere with relative humidity below 10%. Temperature was controlled with a heating stage using a programmable temperature controller. All SFM friction measurements were performed on 0.5 μm to 1 μm sized atomically smooth sample domains. The load was maintained constant for all velocities and temperatures. Across all graphene films, average applied load was 55 ± 7 nN. IFA experiments were performed in random order with respect to film thickness to avoid systematic errors.

Graphene films were prepared by micromechanical cleavage of HOPG (Nanosurf, ZHY quality) onto a Si/SiO_2 substrate (300 nm oxide, Silicon Valley Microelectronics).[22] IFA measurements on CaF_2 were conducted on a surface freshly exposed by mechanical cleavage along the <111> crystallographic plane, which serves as the natural cleavage plane.[23]

5.3 Results and Discussion

Figure 5.1 (a) provides the IFA result obtained from highly ordered pyrolytic graphite (HOPG). In accordance with the IFA methodology, friction-velocity isotherms were collected at multiple temperatures, exhibiting each a log-linear dependence of sliding friction on scanning velocity. Following the principle of time-temperature superposition,[19-21] these friction-velocity isotherms were superimposed to a single friction-velocity master curve, resulting in horizontal velocity shift factors, a_T. According to an Arrhenius analysis of the shift factors at constant pressure P, i.e

$$E_a = k_B \left(\frac{\partial \ln(a_T)}{\partial \left(\frac{1}{T} \right)} \right)_P \tag{5.1}$$

where T and k_B are the absolute temperature, concerning the isotherms, and the Boltzmann constant, respectively, the process specific activation energy E_a can be deduced from the slope in the inset of Figure 5.1(a). The analysis unveiled an activation energy of $(1.35 \pm 0.14) \times 10^{-19}$ J for HOPG employing a silicon dioxide (SiO_2) AFM tip.

The IFA value was compared to the van der Waals interaction energy between HOPG and native SiO_2, using Lipkin et al.'s simplified version of the Lifshitz theory of van der Waals interactions for an isotropic Drude conductor (*c*) and a dielectric (*d*) across vacuum or air,[27] i.e.,

$$A_{cd} \approx \frac{3h}{8} \frac{c_1 v_{e,c} v_{e,d}}{\sqrt{2c_2(c_2 v_{e,d} + v_{e,c})}} \tag{5.2}$$

with the Planck constant h, $c_1 \equiv n_d{}^2 - 1$ and $c_2 \equiv n_d{}^2 + 1$. The expression yields with a conductor plasma frequency $v_{e.c}$ of 3.4×10^{15} s^{-1} for HOPG,[28] a dielectric electronic absorption frequency $v_{e.d}$ of 3.2×10^{15} s^{-1} for SiO_2,[29] and the dielectric index of refraction n_d of 1.448 for SiO_2,[29] a Hamaker interaction energy of 1.31×10^{-19} J, which is in remarkably good agreement with the activation energy obtained from the IFA experiment. The correspondence is notable, as

HOPG is not an isotropic conductor, owing to its layered structure; an aspect we explore in greater detail below.

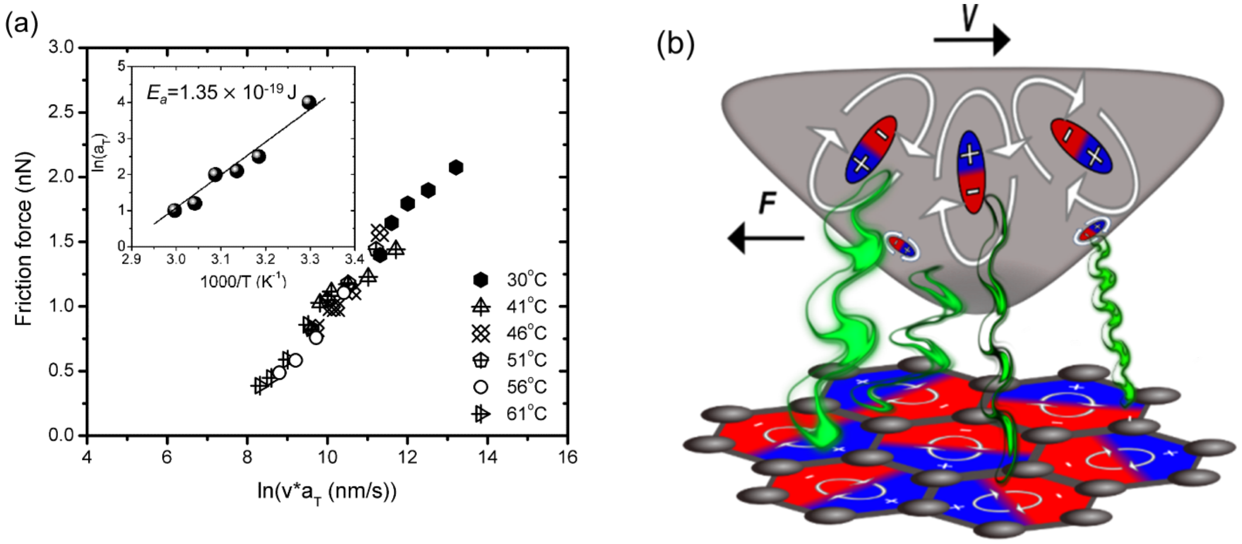

Figure 5.1 (a) Friction-velocity master curve of SiO_2 AFM tip on HOPG. Inset: Arrhenius analysis of thermal shift factors revealing activation energy, E_a of 1.35×10^{-19} J. (b) Sketch of IFA coupling process: The one-dimensional motion with velocity v of the AFM tip in contact with the sample surface scatters with the spontaneous, quantum electrodynamic, dipolar fluctuations in the interface, imprinting the energy signature of the van der Waals dispersion interaction in the frictional response F.

To gain further confirmation of the sensitivity of IFA towards dispersion interactions, we investigated a freshly cleaved atomically smooth surface of calcium fluoride (CaF_2). IFA revealed an activation energy of $(0.68 \pm .09) \times 10^{-19}$ J that we found in excellent agreement with the Hamaker constant of 0.67×10^{-19} J for CaF_2-SiO_2[30] (c.f. experimental data and further discussion in Appendix B). As sketched in Figure 5.1 (b), the energetic data confirm that the moving AFM tip scatters with the quantum electrodynamics originating bonding-debonding fluctuations that form spontaneously at the interface between the tip and sample. During the coupling process of the one-dimensional sliding motion and the interfacial bonding-debonding events, the energy signature of the dispersion interaction is imprinted in the frictional response signal and retrieved by IFA via the Hamaker constant. It is important to note that IFA provides the energetics of the perturbation of the friction signal caused by dispersion interactions in the contact zone between tip and sample. It may not be confused with the tribological energy dissipation that has been studied elsewhere for HOPG and graphene.[31,32]

With this confirmation in hand, we investigated by way of IFA the Hamaker constant dependence between the probing SiO_2 tip and graphene films of multiple thicknesses from the graphene monolayer to the onset of bulk graphite. To this end, graphene films with thicknesses ranging from 1 to 13 atomic layers were prepared by micromechanical cleavage [22] of HOPG deposited onto 300 nm SiO_2 coated silicon substrates. Raman spectroscopy confirmed the unique electronic structure of the graphene samples (c.f. Appendix B). IFA of the graphene monolayer ($n = 1$) and multilayers ($n = 3$, 4, 6 and 13), Figure 5.2(a-d), revealed a graphene–SiO_2 Hamaker constant $A_{Gr-SiO2}$ of $(0.71 \pm 0.14) \times 10^{-19}$ J, i.e., an approximate two-fold reduction of the dispersion interaction compared to HOPG. The graphene layers were identified via their specific heights from the silicon substrate and relative height difference to each other. The monolayer, Figure 5.2(c) was identified according to its 1.0 ± 0.2 nm step height from the substrate, which has been well established as the graphene SiO_2 contact distance,[33] and the multilayer numbers were assigned consistent with multiples of the graphene sheet distance of 0.34 nm.[34] The interaction values in between the two limiting Hamaker constants of monolayer graphene and HOPG, $A_{Gr-SiO2}$ and $A_{HOPG-SiO2}$, respectively, exhibit a sigmoidal behavior of the form

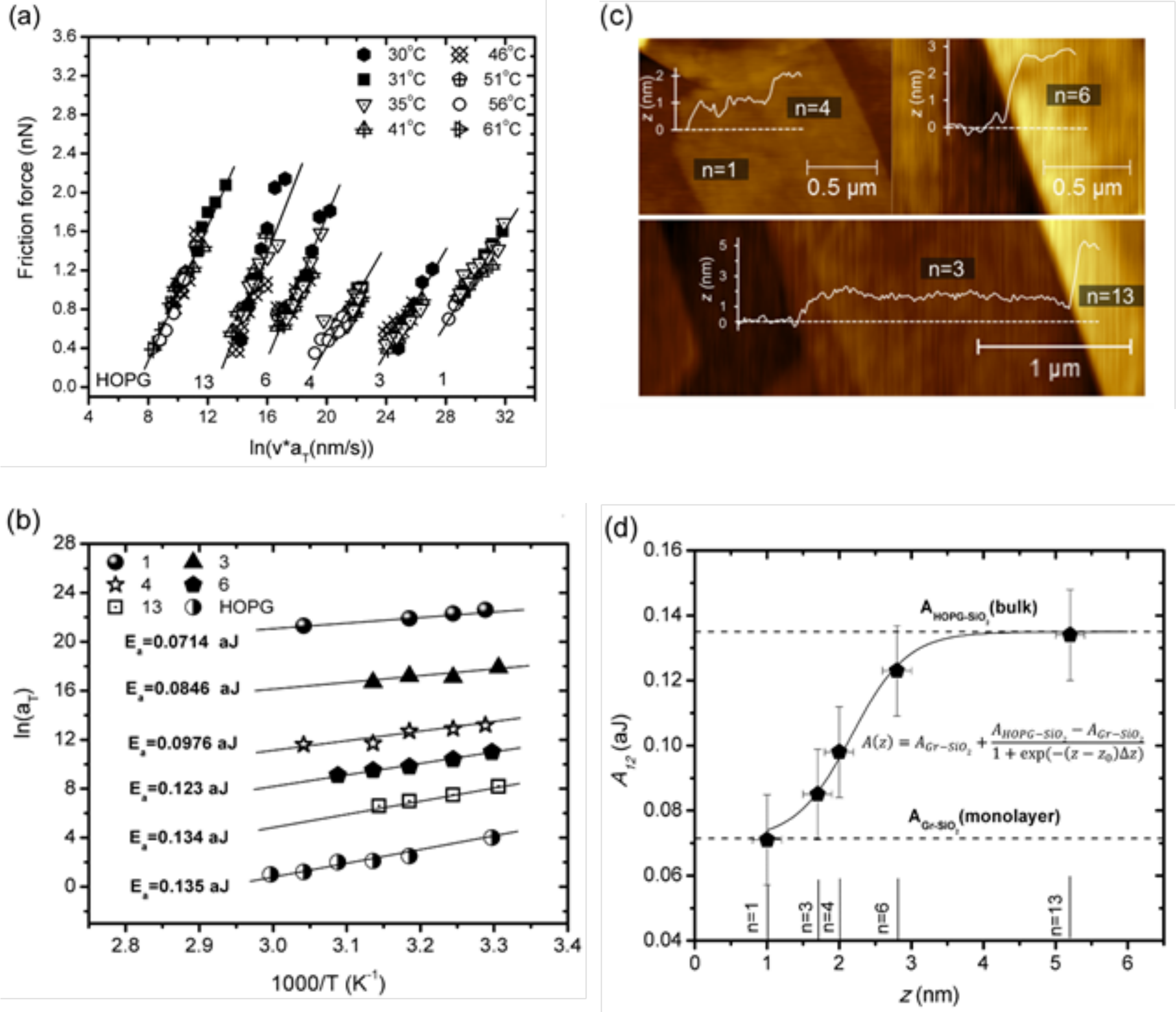

Figure 5.2: (a) Friction-velocity spectra for monolayer ($n = 1$) and multilayer ($n = 3, 4, 6,$ and 13) graphene films. (b) Arrhenius analysis of thermal shift factors a_T (aJ = 10^{-18} J) revealing the activation energies, E_a. (c) AFM topography images of graphene films with line profiles showing step heights measured from substrate. (d) Thickness dependence of IFA-determined Hamaker constant A_{12} for graphene (1) interacting with SiO_2 (2) across air with sigmoid fit curve parameters: $z_0 = 2.17$ nm and $\Delta z = 2.58$ nm^{-1}.

$$A(z) = A_{Gr-SiO2} + \frac{A_{HOPG-SiO2} - A_{Gr-SiO2}}{1 + \exp(-(z - z_o)\Delta z} \qquad 5.3$$

with the fit parameters z_o = 2.17 nm and Δz = 2.58 nm^{-1}, Figure 5.2(d). Notable is the convergence of the Hamaker constant values of graphene multilayers to bulk HOPG at around 7 to 8 atomic layers. The non-retarded Hamaker constant A_{12} between media 1 and media 2 through vacuum (dry air), can be expressed by its respective *single component* Hamaker constants A_{kk} (k = 1, 2) via *combining relations,* [29] as

$$A_{12} \approx \sqrt{A_{11}A_{22}} \qquad 5.4$$

Applying this approximation to the IFA data presented above, and employing the literature value for $A_{SiO2\text{-}SiO2}$ of 0.65 × 10^{-19} J,[30] single component specific Hamaker constants of $A_{CaF2\text{-}CaF2}$ = 0.71 × 10^{-19} J, $A_{HOPG\text{-}HOPG}$ = 2.8 × 10^{-19} J, and $A_{Gr\text{-}Gr}$ = 0.78 × 10^{-19} J for CaF_2, HOPG, and the graphene monolayer (Gr) could be determined, respectively. The value for CaF_2 is in excellent agreement with literature values that converge around 0.70×10^{-19} J.[29] The Hamaker constant of HOPG compares also well to recent computational calculations based on electron energy loss spectroscopic data that yielded a value of 2.5 × 10^{-19} J.[35] Our computational calculations (see below) based on dielectric data[28] from the literature yielded 2.9 × 10^{-19} J for HOPG.

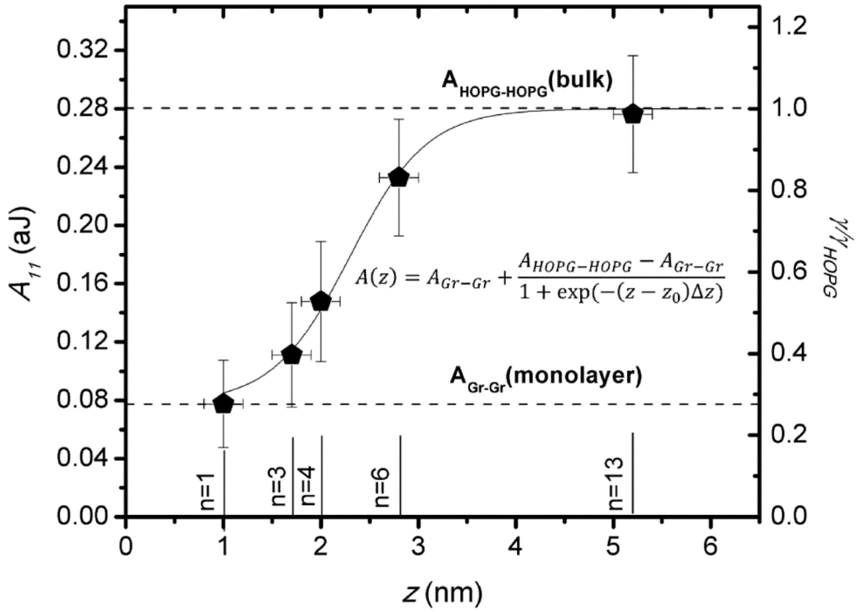

Figure 5.3: Dependence of the surface energy of graphene (normalized to bulk graphite) γ/γ_{HOPG} and the single component Hamaker constant A_{11} as function of the graphene thickness z and layer number n with sigmoid fit curve parameters: $z_0 = 2.3$ nm and $\Delta z = 2.53$ nm^{-1}.

Figure 5.3 presents the single component Hamaker constants of graphene layers from the monolayer to the multilayer onset of HOPG utilizing the data from Figure 5.2(d) and Equation (5.4). In accordance that the surface energy can be expressed as one half of the interfacial energy W at the contact distance D_o, which in turn is related to the Hamaker constant via the right-hand side of the following expression for planar geometry, [29]

$$\gamma = \frac{1}{2}W(D_o) = \frac{A_{11}}{24\pi D_o^2} \qquad 5.5$$

we can directly deduce the relative, (HOPG normalized) surface energy γ/γ_{HOPG} from the Hamaker constant. Thereby, we made the sensitive assumption that the contact distance is independent of the layer number. We included the results of the relative surface energy in Figure 5.3. The following has to be noted for the derivation of the normalized surface energy of graphene: (1) We assumed a constant interlayer distance, and with it a constant contact distance D_o, regardless of the layer numbers, which is in accordance to our data above, and calculations in the literature that find insignificant distance variations of less than 0.03 Å.[36-38] (2) The contact distance D_o is an effective cut off distance between two planar interacting continuous surfaces. It is not congruent to the interlayer distance, as it does not consider distance variations that are apparent on the atomic scale.

As with the Hamaker constants, a striking dependence on the number of graphene layers ensues, with a predicted surface energy for graphene that is only about a quarter (27.9 % to be precise) of that of bulk graphite. The surface energy of graphite has been determined by multiple groups ranging from 54.8 mJ/m^2,[18] to 125 mJ/m^2. The latter value was found in a recent study that recognized rapid contamination of HOPG under ambient conditions.[39] Considering these values and the results presented in Figure 5.3, the surface energy of monolayer graphene can be expected to be between 15 and 35 mJ/m^2. Employing Eq. 5.5 and the energy values provided above, a continuum theory based effective contact distance D_o in the range of 1.7 to 2.6 Å can be deduced.

Referring to a related study, in which the surface energy was probed indirectly via the growth of gold and silver nanoparticles,[40,41] our finding is in line with the strong dependence of the growth diameter on the graphene layer number,[40,41] which was found for gold to be reduced by about 50% for monolayer graphene compared to a three-layer graphene substrate. It is important to note that the metal particle growth study also showed no difference between free-standing graphene monolayer substrates and SiO_2 supported substrates.[41] In other words, the silicon support in our study is not affecting the Hamaker constant measurements.

Returning to the calculations of the Hamaker constant via the Lifshitz theory, we note that Equation 5.2 treated HOPG as an isotropic Drude conductor. However, the layered structure of HOPG produces an anisotropic dielectric tensor composed of frequency-dependent in plane $\varepsilon_{1\parallel}$ (parallel to graphene sheets) and out of plane $\varepsilon_{1\perp}$ (perpendicular to graphene sheets) components containing both Drude (free charge) and Lorentz (bound charge) contributions.[28] More rigorously, the non-retarded Hamaker constant A_{11} between two such identical face-to-face anisotropic media (1) across vacuum (v) can be computed by way of the Lifshitz theory as[42]

$$\begin{aligned} A_{11} &= \frac{3k_BT}{2} \sum_{n=0}^{\infty}{}' \sum_{j=1}^{\infty} \frac{\left(\Delta_{1v}(i\zeta_n)^2\right)^j}{j^3} \\ \textit{with } \Delta_{1v} &= \frac{\sqrt{\mathrm{Re}(\varepsilon_1\| (i\zeta_n)) \times \mathrm{Re}(\varepsilon_{1\perp}(i\zeta_n)) - 1}}{\sqrt{\mathrm{Re}(\varepsilon_1\| (i\zeta_n))} \times \mathrm{Re}(\varepsilon_{1\perp}(i\zeta_n)) + 1} \\ \textit{and } \zeta_n &= \frac{(2\ \pi)^2 nk_BT}{h} \end{aligned} \qquad 5.6$$

where T is the absolute temperature (300 K), k_B is the Boltzmann constant, h is the Planck constant, i is the imaginary unit, ζ_n respresents the angular Matsubara frequencies, Re designates the real component of the complex dielectric function, and the prime in the summation denotes that the first term carries a factor of ½. For convergence, the double summation in Equation 5.6 was truncated at $n = 500$ and $j = 30$. Translation of the EEL spectrum to $\varepsilon(i\zeta_n)$ was performed with a cut-off energy of 40 eV. The universal sheet conductance of graphene,[24,25] $\sigma_{sheet} = e^2/4\hbar$ was translated to the in plane dielectric function as $\varepsilon_{\parallel}(\omega) = i\sigma_{sheet}/\varepsilon_0\omega x$ [26], with frequency ω, vacuum permitivity ε_0, imaginary unit i, and sheet thickness x= 0.34 nm.

We applied the above equation to bulk graphite using a frequency ω dependent Drude-Lorentz model fitted to experimental data in the literature of the form,[28]

$$\varepsilon(\omega) = 1 - \frac{\Omega_p^2}{\omega(\omega + i\Gamma_0)} - \sum_{j=1}^{7} \frac{F_j}{(\omega^2 - \omega_j^2) + i\omega\Gamma'_j} \tag{5.7}$$

using the fit parameters $(\Omega_p,\Gamma_0,\Gamma_j',F_j,\omega_j)$ determined from optical data for $\varepsilon_1\perp$ and those determined from electron energy loss spectoscopy (EELS) data for $\varepsilon_{1\parallel}$(c.f. Appendix B) [28], this analysis yielded a non-retarded Hamaker constant for HOPG $A_{HOPG\text{-}HOPG}$ of 2.9×10^{-19} J. Our calculation is in good agreement with the experimental IFA value above of 2.8×10^{-19}J.

Next we determined numerically the Hamaker constant for graphene based on EELS data of graphene and graphite.[24] To employ Equation (5.6), we translated the loss function $Im(\varepsilon^{-1})$ obtained from the EELS experiments to $\varepsilon(i\zeta_n)$ following a numerical analysis described in the literature [35]. As the dielectric response below 3 eV in EELS experiments is concealed by the subtraction of the zero loss peak,[24,25] rendering the the loss function in this regime unreliable, we used the experimentally-fitted dielectric model described by Equation (5.7) for graphite, and modeled graphene using its established universal sheet conductance.[43,44] Furthermore, as the loss function is presented in arbitrary units, requiring normalization for translation to $\varepsilon(i\zeta_n)$, we matched the data to the IFA results of 2.8×10^{-19} J for graphite, yielding a normalization factor of 1.145. Our IFA normalized numerical analysis resulted in a single-component Hamaker constant for monolayer graphene $A_{Gr\text{-}Gr}$ of 0.5×10^{-19} J. This result is in agreement with the IFA observed prominent decrease in the Hamaker constant for graphene compared to graphite. The deviation from the IFA value of 0.78×10^{-19} J can be attrributed to the rudimentary normalization procedure that was based solely on a single data point, as well as underestimation due to use of a finite cut-off energy of the dielectric spectrum.

5.4 Conclusions

In conclusion, the surface energy dependence on the layer number of graphene was experimentally determined from the local Hamaker constant, which was found to decrease by almost three quarters from HOPG to monolayer graphene, over approximately eight layers (2.7 nm). Considering the wide thickness dispersion in graphene fabricated by chemical routes, these results are of significant importance, and explain shortcomings in graphene applications, such as difficulty dispersing monolayer graphene sheets in solvents,[45] and poor adhesion to pristine monolayer graphene electrodes.[10] Under the assumption of pure graphene sheets, the energetic data presented are of wide use in applications from graphene electrode enhanced solar cells, [3,10] nanolithography involving block copolymers on graphene,[15] nanocomposite dispersions containing graphene sheets,[4] to graphene-mediated capacitive deionization.[11] For chemically modified graphene sheets, intended or unintended via the chosen chemical fabrication route, the surface energy would have to be reevaluated.

This study was made possible by IFA, a lateral force AFM methodology for energetic mode analysis, which was introduced here for the first time as a nanoscale surface analytical tool towards the direct investigation of the Hamaker constant. We find also that the IFA results agree with computational predictions based on EELS spectroscopic data, demonstrating IFA to be a complementary tool to spectroscopy for investigation of dielectric properties. Moving forward, the success of IFA in interrogating van der Waals interactions of atomic layered materials such as graphite opens possibilities for future work in evaluating surface energetics of a multitude of layered materials concerning the preparation method, chemical modification, and surface modification.

5.5 References

(1) Singh, V.; Joung, D.; Zhai, L.; Das, S.; Khondaker, S. I.; Seal, S. *Progress in Materials Science* **2011**, *56*, 1178-1271.
(2) Kim, H.; Abdala, A. A.; Macosko, C. W. *Macromolecules* **2010**, *43*, 6515-6530.
(3) Lee, W. H.; Park, J.; Sim, S. H.; Lim, S.; Kim, K. S.; Hong, B. H.; Cho, K. *J. Am. Chem. Soc.* **2011**, *133*, 4447-4454.
(4) Ramanathan, T.; Abdala, A. A.; Stankovich, S.; Dikin, D. A.; Herrera-Alonso, M.; Piner, R. D.; Adamson, D. H.; Schniepp, H. C.; Chen, X.; Ruoff, R. S.; Nguyen, S. T.; Aksay, I. A.; Prud'Homme, R. K.; Brinson, L. C. *Nature Nanotechnology* **2008**, *327-331*.
(5) Zhang, Y.-L.; Chen, Q.-D.; Jin, Z.; Kim, E.; Sum, H.-B. *Nanoscale* **2012**, *4*, 4858.
(6) Kuilla, T.; Bhadra, S.; Yao, D.; Kim, N. H.; Bose, S.; Lee, J. H. *Progress in Polymer Science* **2010**, *35*, 1350-1375.
(7) Lin, Y.; Ehlert, G. J.; Bukowsky, C.; Sodano, H. A. *ACS Appl. Mater. Interfaces* **2011**, *3*, 2200-2203.
(8) Wang, Y.; Tong, S. W.; Xu, X. F.; Oxyilmax, B.; Loh, K. P. *Adv. Mater.* **2011**, *23*, 1514-1518.
(9) Yuan, L.; Dai, J.; Fan, X.; Song, T.; Tao, Y. T.; Wang, K.; Xu, Z.; Zhang, J.; Bai, X.; Lu, P.; Chen, J.; Zhou, J.; Wang, Z. L. *ACS Nano* **2011**, *5*, 4007-4013.
(10) Rowehl, H. P. J. A.; Kim, K. K.; Bulovic, V.; Kong, J. *Nanotechnology* **2010**, *21*, 505204.
(11) Jia, B.; Zou, L. *Chemical Physics Letters* **2012**, *548*, 23-28.
(12) Rafiee, J.; Rafiee, M. A.; Yu, Z.-Z.; Koratkar, N. *Adv. Mater.* **2010**, *22*, 2151-2154.
(13) Shin, Y. J.; Wang, Y. Y.; Huang, H.; Kalon, G.; Wee, A. T. S.; Shen, Z. X.; Bhatia, C. S.; Yang, H. *Langmuir* **2010**, *26*, 3798-3802.
(14) Zhang, X.; Wan, S.; Pu, J.; Wang, L.; Liu, X. *J. Mater. Chem.* **2011**, *21*, 12251-12258.
(15) Kim, B. H.; Kim, J. Y.; Jeong, S.-J.; hwang, J. O.; Lee, D. H.; Shin, D. O.; Choi, S.-Y.; Kim, S. O. *ACS Nano* **2010**, *4*, 5464-5470.
(16) Dong, J.; Yao, Z.; Yang, T.; Jiang, L.; Shen, C. *Scientific Reports* **2013**, *3*.
(17) Taherian, F.; Marcon, V.; van der Vegt, N. F. A.; Leroy, F. *Langmuir* **2013**, *29*, 1457-1465.
(18) Wang, S. R.; Zhang, Y.; Abidi, N.; Cabrales, L. *Langmuir* **2009**, *25*, 11078-11081.
(19) Jr., D. B. K.; Gray, T. O.; Overney, R. M. *Ultramicroscopy* **2009**, *109*, 991-1000.
(20) Jr., D. B. K.; Widjaja, P.; Acton, O.; Overney, R. M. *J. Chem. Phys.* **2011**, *134*, 104502.
(21) Sills, S.; Overney, R. M. *Phys. Rev. Lett.* **2003**, *91*, 095501.
(22) Novoselov, K. S.; Jiang, D.; Schedin, F.; Booth, T. J.; Khotkevich, V. V.; Morozov, S. V.; Geim, A. K. *PNAS* **2005**, *102*, 10451-10453.
(23) Tasker, P. W. *J. Phys. C* **1979**, *12*, 4977-4984.
(24) Eberlein, T.; Bangert, U.; Nair, R. R.; Jones, R.; Gass, M.; Bleloch, A. L.; Novoselov, K. S.; Geim, A.; Briddon, P. R. *Phys. Rev. B* **2008**, *77*, 233406.
(25) Jovanovic, V. B.; Radovic, I.; Borka, D. *Phys. Rev. B* **2011**, *84*, 155416.

(26) Dressel, M.; Gruner, G. *Electrodynamics of solids: optical properties of electrons in matter*; Cambridge University Press: Cambridge, UK, 2002.
(27) Lipkin, D. M.; Israelachvili, J. N.; Clarke, D. R. *Philosophical Magazine a-Physics of Condensed Matter Structure Defects and Mechanical Properties* **1997**, *76*, 715-728.
(28) Djurisic, A. B.; Li, E. H. *J. Appl. Phys.* **1999**, *85*, 7404-7410.
(29) Israelachvili, J. N. *Intermolecular and Surface Forces*; 3rd ed.; Academic Press, 2011.
(30) Bergstrom, L. *Advances in Colloid and Interface Science* **1997**, *70*, 125-169.
(31) Li, Q.; Lee, C.; Carpick, R. W.; Hone, J. *Phys. Status Solidi B* **2009**, *247*, 086102.
(32) Filleter, T.; McChesney, J. L.; Bostwick, A.; Rotenberg, E.; Emstev, K. V.; Seyller, T.; Horn, K.; Bennewitz, R. *Phys. Rev. Lett.* **2009**, *102*.
(33) Novoselov, K. S.; Geim, A. K.; Morozov, S. V.; Jiang, D.; Zhang, Y.; Dubonos, S. V.; Grigorieva, I. V.; Firsov, A. A. *Science* **2004**, *306*.
(34) Cheon, S.; Kihm, K. D.; Park, J. S.; Lee, J. S.; Lee, B. J.; Kim, H.; Hong, B. H. *Optics Letters* **2012**, *37*, 3765.
(35) Dagastine, R. R.; Prieve, D. C.; White, L. R. *Journal of Colloid and Interface Science* **2002**, *249*, 78-83.
(36) Lam, K. T.; Liang, G. C. *Applied Physics Letters* **2008**, *92*.
(37) Lima, M. P.; Fazzio, A.; da Silva, A. J. R. *Physical Review B* **2009**, *79*.
(38) Gould, T.; Lebeque, S.; Dobson, J. F. *J. Phys.: Condens. Matter* **2013**, *25*, 445010.
(39) Li, Z.; Wang, Y.; Kozbial, A.; Shenoy, G.; Zhou, F.; McGinley, R.; Ireland, P.; Morganstein, B.; Kunkel, A.; Kunkel, A.; Surwade, S. P.; Li, L.; Liu, H. *Nature Materials* **2013**, *12*, 925.
(40) Zhou, H.; Qiu, C.; Liu, Z.; Yang, H.; Hu, L.; Liu, J.; Yang, h.; Gu, C.; Sun, L. *J. Am. Chem. Soc.* **2010**, *132*, 944-946.
(41) Huang, C.-w.; Lin, H.-Y.; Huang, C.-h.; Shiu, R.-J.; Wang, W.-H.; Liu, C.-Y.; Chui, H.-C. *Nanoscale Research Letters* **2012**, *7*, 618.
(42) Parsegian, V. A. *Van der Waals Forces*; Cambridge University Press, 2006.
(43) Drosdoff, D.; Woods, L. M. *Phys. Rev. A* **2011**, *84*, 062501.
(44) Mak, K. F.; Sfeir, M. Y.; Misewich, J. A.; Heinz, t. F. *PNAS* **2010**, *107*.
(45) Hernandez, Y.; Lotya, M.; Rickard, D.; Bergin, S. D.; Coleman, J. N. *Langmuir* **2009**, *26*, 3208-3213.

Chapter 6

Experimental Techniques

A range of experimental techniques have been employed in characterizing the transport and interfacial properties of organic and inorganic materials, both on macro and nanoscales. In the present work we have employed scanning probe microscopy (SPM) based techniques, namely intrinsic friction analysis (IFA) and shear modulation force microscopy (SMFM) to gain insights into the molecular mobilities and conformations in constrained organic and inorganic phase materials. Specifically IFA is employed to probe the molecular mobilities of PTMSP and the dipolar fluctuations of the van der Waals interactions in graphene layers. Shear modulation force microscopy (SMFM) is employed to investigate the thermal transition properties of zwitterionic polymeric brushes. We begin this chapter with a brief overview of scanning probe microscopic techniques in Section 6.1. The theoretical and experimental details of IFA will be discussed in Section 6.2. A brief discussion on SMFM technique is presented in Section 6.3. The gas permeability measurements through the ultra-thin and hybrid PTMSP and PEO membranes were performed using conventional techniques like constant pressure-variable volume method and constant volume-variable pressure method, which will be discussed in Section 6.4.

6.1. Overview of Scanning Probe Microscopy

The invention of Scanning Tunneling Microscopy (STM) by Binning and Rohrer in 1986,[1] pioneered the development of several scanning probe techniques. One of the widely used tools in this family is the scanning force microscope (SFM) which is commonly referred to as atomic force microscope (AFM). The AFM consists of a nanoscale tip (~10 nm) at the end of a cantilever which rasters across the surface of the sample, controlled by the piezoelectric actuators in the x, y and z directions. The cantilever deflection is monitored by means of a laser which reflects off the surface of the cantilever on to a photodiode (Figure 6.1). The force exerted by the tip (F_a) on the sample depends on the cantilever spring constant (C_N) and the deflection of the cantilever (Δz), thus $F_a = C_N \Delta z$. The topographical information of a sample is obtained from the voltage applied to the z-piezoelectric actuator to maintain a constant cantilever deflection. AFM can be operated in two primary modes: Contact mode and non-contact mode. In the contact mode the force exerted by the cantilever on the sample is kept constant as it rasters along the surface, while maintaining a constant contact with the sample. The deflection from the photodiode serves as a feedback signal to control the voltage applied to the z-piezo to maintain a constant force, and this z-piezo voltage translates into the topographical map. In the non-contact mode, the cantilever is oscillated normally at a frequency close to the resonance frequency of the cantilever. As the cantilever is brought closer to the sample, the surface interactions cause a dampening of the modulation. The deviation from the set-point amplitude serves as the feed-back to control the modulation amplitude. The tip to sample distance controlled by the voltage applied to the cantilever translates to the topographical map.

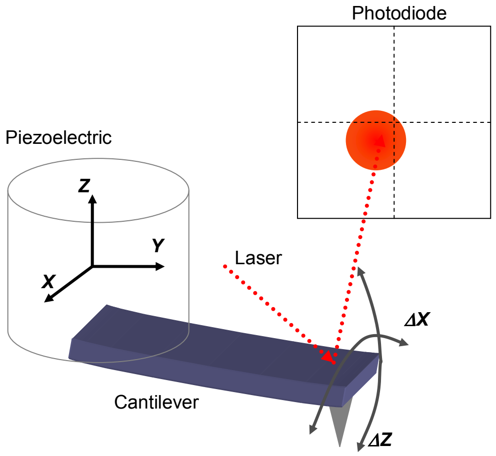

Figure 6.1: Schematic of the working principle of the scanning force microscope (SFM)

6.2. Intrinsic Friction Analysis (IFA)

Intrinsic friction analysis originally formulated by Scott Sills and Overney, is based on the well-established lateral force microscopy.[2,3] Thereby, IFA provides molecular descriptions of relaxation processes that are associated with various modes of molecular/sub-molecular modes of activation.[4,5] As the AFM tips scans on the sample surface it perturbs the system transferring kinetic energy very specifically to internal modes on a molecular or even sub-molecular level, as shown by activating side chain rotations in glassy polystyrene[6,7] and backbone translational motions[6] in polymer melts. The nanoscale friction forces are revealed by the lateral deflection of the cantilever between the forward and reverse scans. These friction signals are obtained at various scanning velocities and temperatures, treated based on the theory of time-temperature equivalence[8,9] to obtain the apparent activation energy. Friction-velocity isotherms, F_F(v), are equivalent to segments of a single master curve[10] that describe the relaxation landscape of a material. Thus the friction force (F_F) measured in IFA is analogous to the dielectric loss, ε*"*, of dielectric spectroscopy and the loss modulus, *G*", in dynamic mechanical analysis. Depending on the dynamic velocity window and temperature range, the isotherms are observed as log-linear curves if far away from the material intrinsic dissipative resonance peak, or curved, if the external disturbance (i.e., sliding velocity) is comparable with the material intrinsic relaxation time. This is illustrated in Figure 6.2 (a) and (b), where the friction-velocity data are log-linear or curved, respectively. To form a single master curve, the data is shifted horizontally with respect to an arbitrarily chosen reference temperature, e.g. T_1.

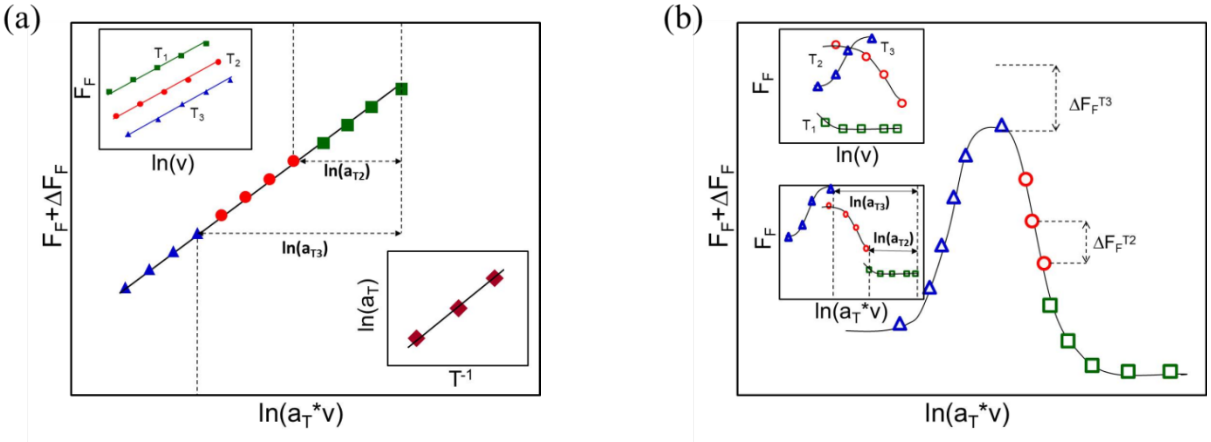

Figure 6.2: Generic $F_F(V)_T$ shifting process based on the time-temperature superposition principle. (a) Relaxation process ($T_1 < T_2 < T_3$) outside the observation window when horizontally shifted form log-linear master line: (*Top Left*) unshifted data, (*Bottom Right*) plot of ln(a_T) vs T^{-1} the slope of which is the apparent 'Arrhenius activation energy'. (b) Slow relaxation process within the experimental scan velocity window: *Left:* (*Top*) Unshifted $F_F(V)_T$ data ($T_1 < T_2 < T_3$), (*Bottom*) Horizontally shifted data. Arrows indicate a_T shifts. *Right:* Bell-shaped master curve after additional vertical ΔF_F shifts.[6]

In the case of fast intrinsic processes that cannot be reached by any rate of the disturbance, the master curve represents a log-linear line, Figure 6.2(a). On the other hand, if the disturbance can match the material (or process) intrinsic relaxation time, the master curve reflects the characteristic relaxation peak, Figure 6.2(b). It is important to note that the current discussion relates only to the enthalpic contribution, i.e., the master curve is obtained by horizontal shifting only. Vertical shifting (Figure 6.2(b) inset) of the friction force by ΔF_F may also be necessary due to the entropic cooperative molecular mobilities in the system.[11] Utilizing the time-temperature equivalence, the set of horizontal shifts, a_T, also referred to as thermal shift factors, are plotted against inverse temperature ($1/T$) to determine the apparent activation energy, E_a, if the process behaves in an Arrhenius manner, (Figure 6.2(a) lower inset). This is formally expressed as

$$E_a = -R\left[\frac{\partial(\ln a_T)}{\partial(1/T)}\right]_P \qquad 6.1$$

It is to be noted that in PTMSP, since we always operate at temperatures below its glass transition temperature, IFA is sensitive to only the enthalpic relaxations and hence we obtain log-linear master curves similar to that shown in Figure 6.2(a), without any significant entropic contributions.[12]

IFA-Experimental Procedure: The experimental set up for IFA is shown in Figure 6.3 and includes a SFM (Topometrix Explorer, Veeco, CA) employing a contact mode lever (PPP-CONT, Nanosensors, nominal and lateral spring constants of ~0.2 N/m and 80 N/m, respectively). The temperature is controlled by a programmable temperature controller. The friction force between the tip and the sample is proportional to the half amplitude of the square wave of the lateral photodiode signal obtained from the sample surface scanning. An oscilloscope is employed to obtain friction data. All measurements were performed at ambient pressure under a dry nitrogen atmosphere with a relative humidity below 10% to avoid water capillary formation.[13]

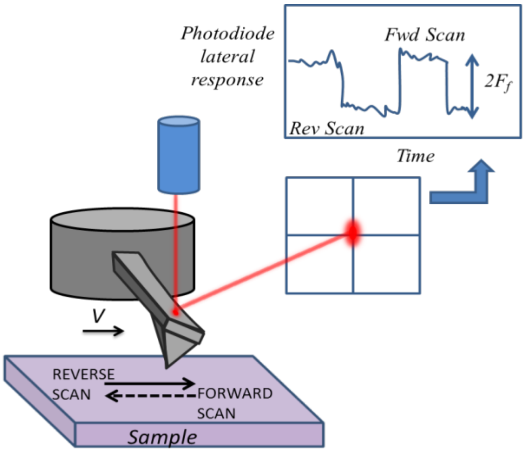

Figure 6.3: Schematic of the intrinsic friction analysis experimental set-up

Calibration of the tip was performed according to a well-established blind calibration technique.[14] For this calibration, the tips are initially conditioned by scanning on silicon wafers described as follows: silicon wafers are initially cleaned by sonicating in acetone (10 minutes) and in methanol (40 minutes) followed by a 20 minute UV treatment. The wafers are then dried in a vacuum oven for 1 hour at 120°C before calibration measurements began. Prior to friction measurements, the out of contact normal cantilever resonance frequency, *f*c (in Hz), was obtained to calculate the cantilever thickness, *t.*

$$t = 0.000723 L^2 f_c \qquad 6.2$$

The cantilever spring constant C_N, was then obtained from the cantilever length (L=[m]), width (W) and elastic modulus (E) according to the following equation:[14]

$$C_N = \frac{E t^3 W}{4L^3} \qquad 6.3$$

The total normal force, F_N, can be calculated for a given applied load, F_{app} (the set point applied) as follows:

$$F_N = \frac{C_N}{S}\left(F_{app} + F_{adh} - F_{T-B}\right) \qquad 6.4$$

where *S* is the apparent contact stiffness i.e., the slope of the photodiode signal (in nN) versus the piezo displacement in nanometers (in nm) during tip-sample contact, F_{adh} is the adhesion force measured by force-distance curves and the F_{T-B} is the out-of-contact top-bottom photodiode signal. Friction was then measured for various values of F_{app}, resulting in a linear plot of the uncalibrated oscilloscope friction signal, F_{Fo} (in mV), and the total normal force, F_N (in nN) with constant slope, μ^* (in mV/nN). Given that the friction coefficient between the SiO_x tip and SiO_x sample is known ($\mu = 0.18$), a calibration coefficient, Γ(nN/mV), was obtained as:

$$\Gamma = \frac{\mu}{\mu^*} = \frac{\mu F_N}{F_{Fo}} \qquad 6.5$$

The calibration of the tip on silicon sample also accomplishes its conditioning, which is critical in getting rid of any sharp asperities present on a new tip. Furthermore the tip is scanned on the sample of interest at temperatures greater than the room temperature (usually around the glass transition temperatures for polymers) to passivate the tip surface which in turn prevents any pick up of organic material by the tip. Once the tip was calibrated and conditioned, the sample was electrically grounded to the AFM. Grounding was performed by connecting a small wire from the sample to a common contact point (in our case the steel SFM stand) via silver paint (Ted Pella, Inc.). Care was taken such that the grounding wire still allowed the sample to sit flat on the heating stage. The scanning plane was leveled horizontally to within 100 nm vertical displacement over a 100 µm horizontal scan.

We have performed IFA on PTMSP films of varying thickness, to probe the thermally active molecular modes (Chapter 2). Activation energies around 4.5-7.9 kcal/mol were obtained (discussed in Chapter 2). In order to identify the appropriate rotational modes corresponding to the measured range of activation energies, the conformational energies for rotations about the **1** trimethyl–silyl backbone bond, the **2** methyl–backbone bond, and **3** the backbone single bond [12] are calculated (Figure 6.4 (a)). These molecular conformational calculations, revealed for bond rotations **1, 2**, and **3** rotational activation energies of ~13 kcal/mol, 5 kcal/mol, and >100 kcal/mol respectively (Figure 6.4 (b)). Hence, in light of the IFA and conformational calculations, the experimentally observed thermally active relaxation modes can be attributed to **2**, i.e., backbone methyl-group rotations.[12] IFA was also employed to study the van der waals interaction potential between the AFM tip and graphene layers as discussed in Chapter 5.

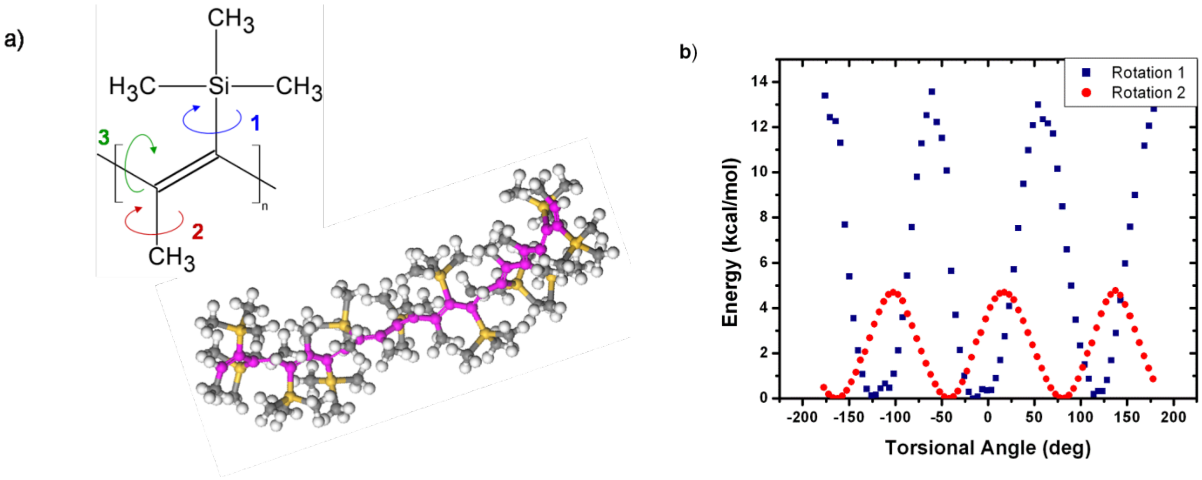

Figure 6.4: (a) The various rotational sub-molecular relaxation modes in PTMSP studied (b) The activation energies associated with the rotational modes **1** and **2** shown in part (a) which correspond to the rotation energies of silicon atom and the methyl side group respectively.

6.3. Shear modulation force microscopy (SM-FM)

SM-FM[15-17] provides critical temperature values that are indicative of possible phase changes or more subtle mobilities within the material phase. In polymers, critical temperature values pinpoint to transitions caused, for instance, by side-chain relaxations or backbone relaxations (glass transition). This technique probes the viscoelastic properties of the sample such as the modulus by examining the mechanical response of the material to the external shear force modulations at varying temperatures. The lateral force dF acting on the sample of area $A=\pi a^2$ results in a lateral stress $d\tau$. The shear stress is related to the shear modulus (G) using the Hooke's law as follows:

$$d\tau = Gd\gamma \qquad 6.6$$

where $d\gamma$ is the shear strain in the material. For small lateral no-slip disturbances, the contact area can be assumed to be unaffected, and thus, the shear force is proportional to the product of modulus and strain. The effective spring constant, k_{eff}, is proportional to the product of the contact modulus and contact radius. The total lateral displacement, *dx*, combines both the sample deformation, *du*, and the spring deformation in the lateral direction . If the force is solely related to the sample deformation, the spring constant is referred to as the contact stiffness k_c. Contact stiffness and effective spring constant are related to each other via the cantilever lateral spring constant k_x as shown below:[16]

$$k_{eff} = \left(\frac{1}{k_c} + \frac{1}{k_x} \right)^{-1} \qquad 6.7$$

The lateral spring constant of the cantilever is determined from the blind calibration method as described above. For a sphere-plane geometry, the contact stiffness is given as

$$k_c = 8G^* a \qquad 6.8$$

where G^* represents the contact modulus given by

$$G^* = \left[\frac{(2 - \nu_{tip})}{G_{tip}} + \frac{(2 - \upsilon_{sample})}{G_{sample}} \right]^{-1} \qquad 6.9$$

Where G_{tip} and G_{sample} represent the shear moduli and v_{tip} , v_{sample} represent the poission ratio of the tip and sample respectively.

SMFM-Experimental Procedure: A nanometer sharp SFM (Explorer, Veeco Instrument Inc) cantilever tip is brought into contact with the sample surface, while a constant load is applied, and the probing tip is laterally modulated (typical input modulation 0.1 V at 1500 Hz) with a "no-slip" nanometer amplitude generated by the frequency generator (DS345 30MHz Synthesized Function Generator, Stanford Research System) . The modulation response is analyzed using a two-channel lock-in amplifier (7280 DSP Lock-In Amplifier, Perkin Elmer Instrument), comparing the response signal to the input signal. The modulation response is a measure of the contact stiffness. Thermally activated transitions in the material, such as the glass transition, melting transitions or changes in the molecular conformations, are determined from changes in the response curve as typically shown in Figure 6.5.[18] Conceptually, SM-FM is a nanoscopic analogue to dynamic mechanical analysis (DMA), however, because of its small probing volume, SM-FM is probing very close to the material's unperturbed state.[17]

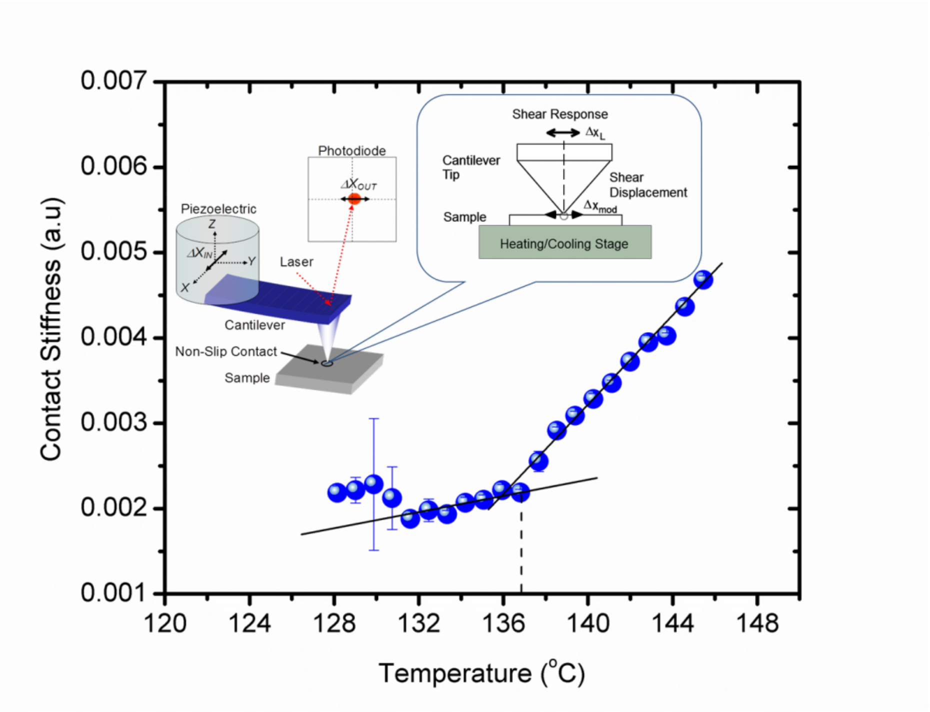

Figure 6.5: A typical SM-FM analysis of a nonlinear optical (NLO) material.[18] Schematic of SM-FM experimental principle in the inset

6.4. Permeability Measurement

There are two primary methods of measuring single gas permeability of polymer membranes, isobaric (constant pressure variable volume), and isochoric (constant volume variable pressure). The isobaric method is relatively simple, without the requirement of vacuum pressure. However it is well suited only to high gas flux measurements (> ~0.5 cc/min). At low fluxes, measurement of downstream gas flow rates become increasingly difficult, giving benefit to the constant volume variable pressure method.

6.4.1. *Isobaric Permeability Measurement*

In the isobaric system, gas is fed to the upstream side of the membrane, and the outflow of gas is measured directly using a precision flow measuring device. The basic schematic is shown in Figure 6.6. The membrane is housed in a 25mm stainless steel Pall Filter holder. Upstream pressure is regulated and downstream pressure is atmospheric. The purge valve is used to ensure that no contaminant gases are present in the line. After waiting for equilibrium, the downstream permeating gas flow rate is determined using a bubble flow meter for a given upstream gas pressure. Two different size flow meters (0.5 ml and 10 ml graduated volume) were used depending on the downstream flow rate.

The gas permeability, P (1 Barrer = 10^{-10} (cm^3(STP) cm)/cm^2 s cmHg) was determined from the flux, J (cm^3(STP)/cm^2·s), the membrane cross-sectional area, A (cm^2), the thickness, l (cm), and the externally controlled differential pressure, Δp ($\Delta p = p_2 - p_1$), (cm Hg) as:

$$P = \left(\frac{Jl}{\Delta p} \right) \qquad 6.10$$

Flux was obtained from the following expression[19]

$$J = \left(\frac{273.15 p_{atm}}{76T} \right) \frac{1}{A} \frac{dV}{dt} \qquad 6.11$$

where p_{atm} is the atmospheric pressure in cm Hg, T is the temperature of the gas in Kelvin, (dV/dt) is the gas flow rate in cm^3/s. Membrane thicknesses were measured by contact mode scanning force microscopy (SFM) (*Easy Scan 2*, Nanosurf GmbH) of a scratch made on the surface of the polymer penetrating the thickness of the film avoiding perturbing/damaging the supporting substrates after the gas permeabilities had been measured.

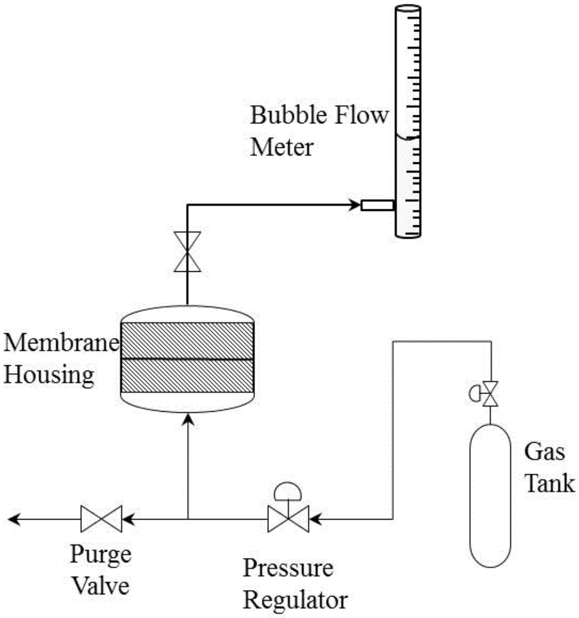

Figure 6.6: Schematic of a constant pressure variable volume method based gas permeability measurement set-up

Gas permeabilities through thin films of PTMSP were measured by this technique. By the way of illustration, the gas flow rate of CO_2 and helium through a neat AAO membrane and ~200 nm PTMSP film spin casted on AAO as a function of differential pressure (Δp) are contrasted in Figure 6.7(a) & (b).[12] The gas flow rate, $q \equiv dV/dt$, was substituted in Eq(6.11) to obtain the gas flux which was further utilized to obtain the gas permeabilities through the membranes from Eq(6.10).

The gas flux of helium is ~ 3 times higher than that of CO_2 through the neat AAO membrane indicative of diffusion dominated size selective permeation behavior (Figure 6.7(a)), while the thin PTMSP films spin casted on AAO exhibit preferential CO_2 selectivity over helium[12] (Figure 6.7(b)) owing to the sorption dominated solution diffusion mechanism, commonly observed in dense glassy polymeric membranes.

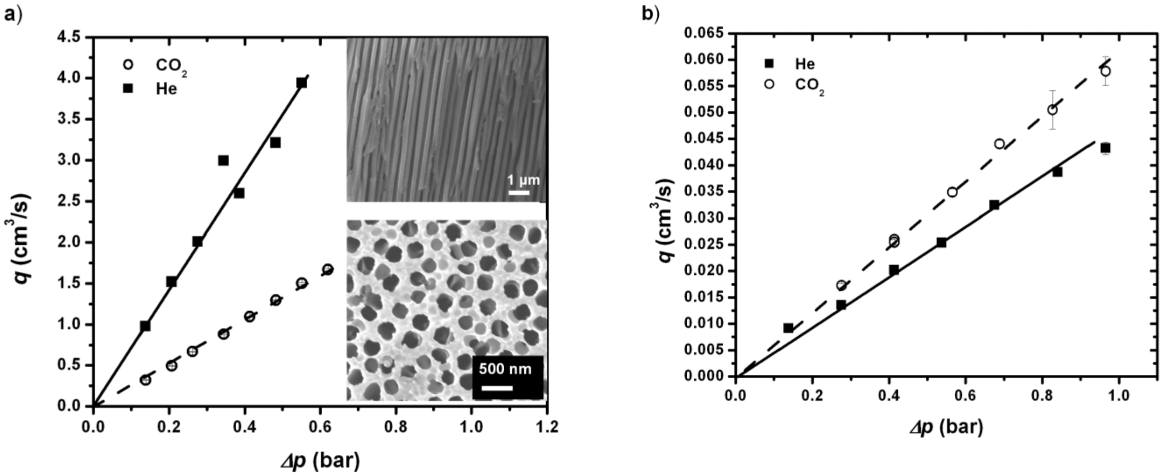

Figure 6.7: The gas flux of helium and CO_2 through (a) a neat AAO membrane and (b) 200 nm PTMSP film supported on AAO membrane.[12] The insets in (a) represent the cross section(top) and top views of AAO membranes (bottom) respectively.

6.4.2. Isochoric Permeability Measurement

The isochoric permeability measurement *i.e.* the constant volume variable pressure (CVVP) set-up was utilized to measure the permeabilities of AAO confined hybrid PEO and PTMSP membranes. Permeabilities of AAO supported thick PTMSP and PEO membranes (> 3 µm) were also measured by the CVVP technique. In this set-up a 25mm stainless steel Pall Filter holder is used to house the polymeric membranes. Vacuum pressure in the set-up is measured by means of Dwyer pressure transducer and the current signal (in mA) from the transducer is recorded with a Dwyer USB port connected in the line. This current vs. time data is converted to the pressure change rate in the chamber by utilizing the calibration curves of the transducer. In the isochoric measurement, initially the membrane housing and the downstream gas chamber are evacuated by applying vacuum suction by opening needle valves 2&3 (Figure 6.8).

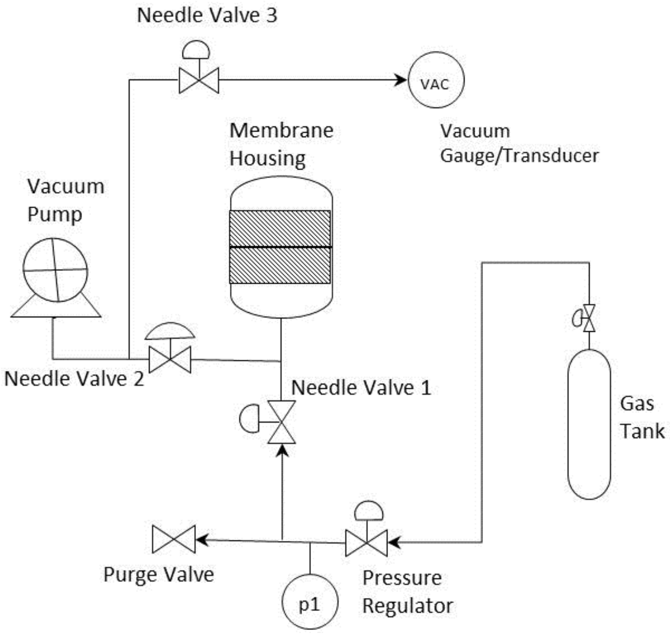

Figure 6.8: The schematic of the constant volume variable pressure (CVVP) set up.

The upstream needle valve 1 is closed during the evacuation. After closing the needle valves 2 and 3, the leak rate of air into the system ($(dp/dt)_{leak}$) is recorded from the slow increase in chamber pressure. In the next step, the membrane housing volume is re-evacuated, by opening valves 2 and 3, with the upstream gas valve 1 closed. Following the chamber evacuation, the valves 2 and 3 are closed and needle valve 1 is slowly opened, exposing the upstream side of the membrane to a specific gas pressure. The gas permeating through the membrane is measured by recording the increase in the gas pressure in the downstream membrane chamber as a function of time ($(dp/dt)_{SS}$). The gas permeability (cm^3 (STP) cm/cm^2.s. cm Hg) is determined from the steady state rate of pressure increase in the fixed downstream volume by:[20]

$$P = \frac{V_d l}{p_2 ART}\left[\left(\frac{dp_1}{dt}\right)_{SS} - \left(\frac{dp_1}{dt}\right)_{leak}\right] \qquad 6.12$$

Where V_d is the volume of the downstream chamber (cm^3), l is the membrane thickness (cm), p_2 is the upstream pressure (cm Hg), A is the membrane area (cm^2), R is the ideal gas constant, T is the absolute temperature (K), $(dp_1/dt)_{\mathrm{SS}}$ and $(dp_1/dt)_{\mathrm{leak}}$ are the steady state rate of pressure increase and the leak rate in the chamber respectively (cm Hg/s). For the current isochoric apparatus, the downstream volume was found to be 9.35 cm^3.

6.5. References

(1) Binnig, G.; Quate, C. F.; Gerber, C. *Physical Review Letters* 1986, *56*, 930-933.
(2) Overney, R. M., L. Guo, H. Totsuka, M. Rafailovich, J. Sokolov, and S. A.; Schwarz, S. A. *Material Research Society* 1997.
(3) R. M. Overney, H. T., M. Fujihira, W. Paulus, and H. Ringsdorf *Physical Review Letters* 1994, *72*, 3546.
(4) Knorr, D. B.; Widjaja, P.; Acton, O.; Overney, R. M. *J. Chem. Phys.* 2011, *134*.
(5) Knorr, D. B.; Zhou, X. H.; Shi, Z. W.; Luo, J. D.; Jang, S. H.; Jen, A. K. Y.; Overney, R. M. *Journal of Physical Chemistry B* 2009, *113*, 14180-14188.
(6) Knorr, D. B.; Gray, T. O.; Overney, R. M. *Ultramicroscopy* 2009, *109*, 991-1000.
(7) Sills, S.; Overney, R. M. *Physical Review Letters* 2003, *91*.
(8) Ward, I. M. *Mechanical Properties of Solid Polymers*; Wiley-Interscience, London, 1971.
(9) Ferry, J. D. *Viscoelastic Properties of Polymers*; John Wiley &Sons, 1980.
(10) Grosch, K. A. *Proceedings of the Royal Society of London Series a-Mathematical and Physical Sciences* 1963, *274*, 21-+.
(11) Knorr, D. B.; Gray, T. O.; Overney, R. M. *J. Chem. Phys.* 2008, *129*, 074504.
(12) Knorr, D. B., Jr.; Kocherlakota, L. S.; Overney, R. M. *Journal of Membrane Science* 2010, *346*, 302-309.
(13) He, M. Y.; Blum, A. S.; Overney, G.; Overney, R. M. *Physical Review Letters* 2002, *88*.
(14) C. K. Buenviaje, S. R. G., M. H. Rafailovich, and R. M. Overney In *Materials Research Society Symposium Proceedings*, 1998; Vol. 552, pp 187-192.
(15) Ge, S.; Pu, Y.; Zhang, W.; Rafailovich, M.; Sokolov, J.; Buenviaje, C.; Buckmaster, R.; Overney, R. M. *Physical Review Letters* 2000, *85*, 2340-2343.
(16) Gray, T.; Killgore, J.; Luo, J. D.; Jen, A. K. Y.; Overney, R. M. *Nanotechnology* 2007, *18*.
(17) Sills, S.; Overney, R. M.; Chau, W.; Lee, V. Y.; Miller, R. D.; Frommer, J. *J. Chem. Phys.* 2004, *120*, 5334-5338.
(18) Benight, S. J.; Knorr, D. B.; Johnson, L. E.; Sullivan, P. A.; Lao, D.; Sun, J. N.; Kocherlakota, L. S.; Elangovan, A.; Robinson, B. H.; Overney, R. M.; Dalton, L. R. *Advanced Materials* 2012, *24*, 3263-3268.
(19) Pinnau, I.; Toy, L. G. *Journal of Membrane Science* 1996, *116*, 199-209.
(20) Lin, H.; Freeman, B. D. *Journal of Membrane Science* 2004, *239*, 105-117.

Chapter 7

Closing Remarks and Future Outlook

In this work we have investigated the impact of nanoscale confinement on the interfacial and transport properties of organic and inorganic systems. Confinement effects on the gas transport properties of two reverse selective polymeric membranes viz. PTMSP and PEO were investigated. Specifically, enhanced gas permeabilities and bulk deviating reverse selectivities were observed in ultra-thin PTMSP membranes in the thickness regime of 400 to 800 nm. The molecular energetic mobility analysis (IFA) of the thermally active modes in PTMSP revealed enhanced methyl side groups mobilities indicating interfacially induced structural adaptations in PTMSP that led to an increase in free volume in the critical film thickness regime.[1] Inspite of their enhanced free volume configuration, aging analysis revealed that these "free-standing" ultra-thin membrane films physically age within hours due to the plasticizing effect of the sorbing gas component that causes a free-volume collapse.

Having identified the length scales in which the interfacial constraints positively impact the gas transport properties, we translated these confinement effects into hybrid AAO-PTMSP membranes. Thereby the constrained AAO impregnated PTMSP phase exhibited a four-fold permeability increase for CO_2, helium and nitrogen, and a 40% improvement of the reverse selectivity of CO_2 over non- sorbing gases (CO_2/He, CO_2/N_2) in comparison to bulk PTMSP membranes.[2] Furthermore, the temporal stability in AAO embedded PTMSP was found to be improved substantially by a factor of 20 over its thin-film counterparts. Constrained PEO polymeric phase has been shown in literature to exhibit significantly reduced crystallization temperature ($\Delta T_{bulk \rightarrow nanotube} = 50^{o}C$) as a consequence of the transition from a heterogeneous nucleation processes in bulk PEO to a surface nucleation process in PEO nanotubes.[3] Gas permeabilities of helium and CO_2 through PEO-AAO hybrid membranes were primarily influenced by the remnant top bulk PEO layer. However the permeability of CO_2 was found to increase from 12 Barrer in unimpregnated bulk PEO membranes to 17 Barrer in PEO-AAO nanocomposite membrane indicating that CO_2 sorption and surface diffusion through PEO nanotubes create additional permeation pathways leading to enhanced CO_2 separation capabilities in AAO confined PEO membranes.

The here found improvements in the gas permeabilities in ultra-thin PTMSP films indicate that imposing interfacial constraints on other novel glassy microporous polymeric systems with better temporal stability, could result in an enhancement of their gas transport properties, potentially matching the high permeation rates of PTMSP membranes. Novel glassy polymers with intrinsic microporosity (PIMs) are being synthesized with high gas permeabilities which would be potentially interesting candidates for the interfacial confinement studies.[4-6] Similarly in PEO based membranes blends of poly(ethylene oxide)-poly(butylene terephthalate) (PEO-PBT) copolymer and polyethylene glycol-dibutyl ether (PEG-DBE) were shown to exhibit outstanding CO_2 permeabilities of ~750 Barrer with CO_2/N_2 reverse selectivity of ~40,[7] placing it at the Robeson limit. The permeances were found to increase from 0.8 m^3(STP) m^{-2} h^{-1} bar^{-1} to 5 m^3(STP) m^{-2} h^{-1} bar^{-1}, as the film thickness reduced from 170 nm to 45 nm, the highest permeance values for CO_2 through PEO based polymers. The CO_2/N_2 selectivity in the ultra-thin films (~45 nm) was found to be 60. Yave et al. proposed that interfacial confinement of the polymer could be causing altered molecular relaxations/mobilities, which influence the transport properties of the polymer.[8] Transposing the beneficial interfacial properties found in the above mentioned polymeric systems *viz*. PEO-PBT copolymers and PIMs into an external membrane confined nanocomposite membrane will result in development of stable and scaled up reverse-selective polymeric membrane systems. While PEO-PBT requires a dimensional confinement on the sub-150 nm scale, PTMSP, because of its backbone rigidity, reveals optimum transport properties in the confinement regime of 0.1 to 1 μm. Though AAO membranes are a good confining template owing to their uniform porous structure, their mechanical strength is rather limited. So utilizing other porous "substrates", namely, polycarbonate (PC) with its small pores for PEO-PBT, and the two ultrafiltration (UF) membranes, poly(vinylidene fluoride (PVDF) and polyacrylonitrile (PAN) membranes for confining PTMSP, would result in fabrication of 'inverse nanocomposite' membranes which increase the polymer free-volume, as found in ultrathin films, confined in a mechanically free-volume stabilizing environment, as discussed above for PTMSP and PEO, to provide both increased permeation for the carrier gas, and an enhanced CO_2 sorption activity.

The interfacial energy between the surface and water is found to be critical in conferring non-fouling properties to the surface.[9] Polyzwitterionic brushes are shown to bind water very strongly due to electrostatically induced hydration which forms a physical and energetic barrier to prevent protein adsorption on the surface. Optimum film thickness of 62 and 20 nm of pSB and pCB respectively resulted in minimum protein adsorption from 100% blood serum.[10,11] Physico-chemical properties of these materials like molecular weight, surface chemistry and their surface packing, i.e film thickness, packing density [12] and chain conformations. In this work the thermal transitions of pSBMA, pCBAA and pEGMA brushes are investigated to gain insights into their molecular conformations. pSBMA brushes showed a critical transition temperature of 60-75°C in 27 and 16 nm films respectively analogous to the critical solution temperature behavior of the sulfobetaines while no changes were observed the in molecular conformations of pCBAA films in the same temperature regime, indicating that pCBAA is stable over this temperature range. Systematic investigation of pSBMA films as a function of packing density will provide insights into the molecular conformations/interactions of these brushes thus enabling rational design of non-fouling surfaces.

IFA, a lateral force AFM methodology for energetic mode analysis, was utilized as a nanoscale surface analytical tool towards the direct investigation of the Hamaker constant in graphene layers.[13] The surface energy dependence on the layer number of graphene was experimentally determined from the local Hamaker constant, which was found to decrease by almost three quarters from HOPG to monolayer graphene, over approximately eight layers (2.7 nm). The success of IFA in interrogating van der Waals interactions of atomic layered materials such as graphite opens possibilities for future work in evaluating surface energetics of a multitude of layered materials concerning the preparation method, chemical modification, and surface functionalization.

References

(1) Kocherlakota, L. S.; Knorr, D. B., Jr.; Foster, L.; Overney, R. M. *Polymer* **2012**, *53*, 2394-2401.
(2) Kocherlakota, L.S.; Pham, T.; René M. Overney *Polymer* **2013**, *54*, 5986-5992.
(3) Maiz, J.; Martin, J.; Mijangos, C. *Langmuir* **2012**, *28*, 12296-12303.
(4) Budd, P. M.; Msayib, K. J.; Tattershall, C. E.; Ghanem, B. S.; Reynolds, K. J.; McKeown, N. B.; Fritsch, D. *Journal of Membrane Science* **2005**, *251*, 263-269.
(5) Du, N.; Dal-Cin, M. M.; Pinnau, I.; Nicalek, A.; Robertson, G. P.; Guiver, M. D. *Macromolecular Rapid Communications* **2011**, *32*, 631-636.
(6) Du, N.; Robertson, G. P.; Song, J.; Pinnau, I.; Thomas, S.; Guiver, M. D. *Macromolecules* **2008**, *41*, 9656-9662.
(7) Yave, W.; Car, A.; Funari, S. S.; Nunes, S. P.; Peinemann, K. V. *Macromolecules* **2010**, *43*, 326-333.
(8) Yave, W.; Car, A.; Wind, J.; Peinemann, K. V. *Nanotechnology* **2010**, *21*.
(9) Krishnan, S.; Weinman, C. J.; Ober, C. K. *Journal of Materials Chemistry* **2008**, *18*, 3405-3413.
(10) Zhang, Z.; Chen, S. F.; Chang, Y.; Jiang, S. Y. *Journal of Physical Chemistry B* **2006**, *110*, 10799-10804.

(11) Cheng, G.; Li, G.; Xue, H.; Chen, S.; Bryers, J. D.; Jiang, S. *Biomaterials* **2009**, *30*, 5234-5240.

(12) Huang, C. J.; Li, Y. T.; Krause, J. B.; Brault, N. D.; Jiang, S. Y. *Macromolecular Rapid Communications* **2012**, *33*, 1003-1007.

(13) Kocherlakota, L.S.; B. A. K., and René M. Overney *Advanced Materials Interfaces* (Submitted) .

Appendix A

Fundamentals of Gas/Vapor Separation Membranes

Dense non-porous polymers including both glassy and rubbery materials have been employed as membrane materials for gas or vapor separation.[1-4] Gas transport through dense non-porous membranes is commonly described using solution diffusion theory. According to this theory gas transport occurs by sorption of gas on the upstream side of the membrane surface followed by the molecular diffusion through the polymeric matrix and subsequent desorption from the downstream surface. Thermodynamic factors like condensability of the gas and its interaction with the polymer segments along with kinetic factors governed by the size of the penetrant, polymer segmental mobility and packing, or free volume influence the overall gas permeation through a given polymeric membrane.[4,5] In rubbery polymers the penetrant diffusion rate is higher with lower sensitivity to the penetrant size. On the other hand, in glassy polymers the penetrant diffusion rates are lower and are critically dependent on the penetrant size.

The sorption of simple gases in rubbery polymers follows the Henry's law, where a linear relation exists between the equilibrium concentration of gas dissolved in polymer (C) and the partial pressure in the gas phase (p).

$$C = Sp \tag{A.1}$$

where S is the solubility coefficient. Steady-state diffusion process is described by the Fick's law as shown below

$$N_i = \frac{D_i \Delta C_i}{L} = \frac{D_i S_i \Delta p}{L} = \frac{P_i \Delta p}{L} \qquad \text{A.2}$$

Where P_i is the permeability coefficient of gas *'i'*, $\Delta p=(p_2-p_1)$ is the pressure drop across the membrane, p_2 is the upstream pressure and p_1 is the downstream pressure, N_i is the gas flux, D_i is the diffusion coefficient and L is the thickness of the membrane. The permeability coefficient P_i in this case is given by

$$P_i = D_i S_i \qquad \text{A.3}$$

Glassy polymers exist in a state of non-equilibrium where the polymeric segmental mobility is restricted and as a consequence possess excess volume relative to the equilibrium state, termed as excess free volume.[4] Unlike the rubbery polymers the sorption of gases in the glassy is well described by the dual mode sorption model [6,7] where the sorption occurs through a combination of (i) Henry's law mode (ii) Langmuir type of sorption sites. The latter arise due to the presence of holes or micro-voids present in glassy polymers owing to their non-equilibrium state

$$C = k_D p + \frac{C'_H b p}{1 + bp} \qquad \text{A.4}$$

Where k_D is the Henry's law coefficient, b and $C_H{}'$ are the Langmuir hole affinity parameter and the capacity parameter respectively. In general the gas solubility is higher in glassy polymers than rubbery polymers which is attributed to the presence of micro-voids which provide additional sorption sites.[8] Subsequently the gas permeability through glassy polymers can be obtained from Eq.(A.) as follows:

$$P = k_D D_D + \frac{C'_H b D_H}{1 + bp_2} \qquad \text{A.5}$$

where D_D and D_H are the diffusion coefficients of gas sorbed through the Henry's mode and the Langmuir mode respectively. The dual mode sorption model predicts that gas permeability decreases with upstream gas pressure in the high pressure regime.[4] The diffusion coefficient of penetrant gases through glassy polymers is well-represented by

$$D = A \exp\left(\frac{-B}{FFV} \right) \qquad \text{A.6}$$

where A is the pre-exponential factor and B is a penetrant gas size dependent parameter. The permselectivity of gas A over B can be obtained from Eq.(A.3) as shown below:

$$\alpha_{A/B} = \frac{P_A}{P_B} = \left(\frac{D_A}{D_B} \right) \left(\frac{S_A}{S_B} \right) \qquad \text{A.7}$$

It can be seen that the permselectivity of a membrane depends on the diffusivity selectivity (D_A/D_B) and solubility selectivity (S_A/S_B). The diffusion coefficient decreases as the penetrant molecule size increases while the solubility coefficient increases as the condensability of the gas increases. The critical temperature and boiling point of the penetrant gases are the critical parameters that influence the condensability of gases.

In case of glassy polymers the diffusion selectivity favors the smaller penetrant gases such that $D_A/D_B>>1$, where gas molecule A is the smaller than B. On the other hand the sorption selectivity will be opposite, $S_A/S_B<1$, since the larger gas molecules are usually more condensable than the smaller one. So the combined effect usually results in a size based permselectivity in most of the glassy polymers ($P_A/P_B>1$). But in reverse selective polymers like PTMSP, the diffusivity selectivity may be greater than unity but not only slightly so, and the solubility selectivity $S_A/S_B<<1$, such that $P_A/P_B<1$. Thus larger molecules permeate faster than the smaller molecules through these polymers.

References

(1) Shao, L.; Low, B. T.; Chung, T. S.; Greenberg, A. R. *Journal of Membrane Science* **2009**, *327*, 18-31.

(2) Baker, R. W. *Industrial & Engineering Chemistry Research* **2002**, *41*, 1393-1411.

(3) Lin, H. Q.; Freeman, B. D. *Journal of Molecular Structure* **2005**, *739*, 57-74.

(4) Lau, C. H.; Li, P.; Li, F. Y.; Chung, T. S.; Paul, D. R. *Prog. Polym. Sci.* **2013**, *38*, 740-766.

(5) Wijmans, J. G.; Baker, R. W. *Journal of Membrane Science* **1995**, *107*, 1-21.

(6) Koros, W. J.; Chan, A. H.; Paul, D. R. *Journal of Membrane Science* **1977**, *2*, 165-190.

(7) Koros, W. J.; Paul, D. R. *Journal of Polymer Science Part B-Polymer Physics* **1978**, *16*, 1947-1963.

(8) Kanehashi, S.; Nagai, K. *Journal of Membrane Science* **2005**, *253*, 117-138.

Appendix B

Local Energetic Analysis of the Surface Energies for Graphene from the Single Layer to Bulk HOPG

Raman Spectroscopy of Graphene

Micro-Raman spectroscopy and optical microscopy, **Figure B1,** were performed on the region identified as monolayer graphene and bulk HOPG using a Reinshaw inVia Raman microscope (514 nm laser) equipped with a Leica DMIRBE inverted optical microscope to confirm the unique electronic structure of graphene The optical microscope image reveals the well-known thickness-dependent color contrast of graphite nanofilms against a SiO_2 coated (300 nm) Si substrate, with graphene appearing as faint lavender and successively thicker graphite films appearing as dark blue, and eventually whitish-blue.[1]

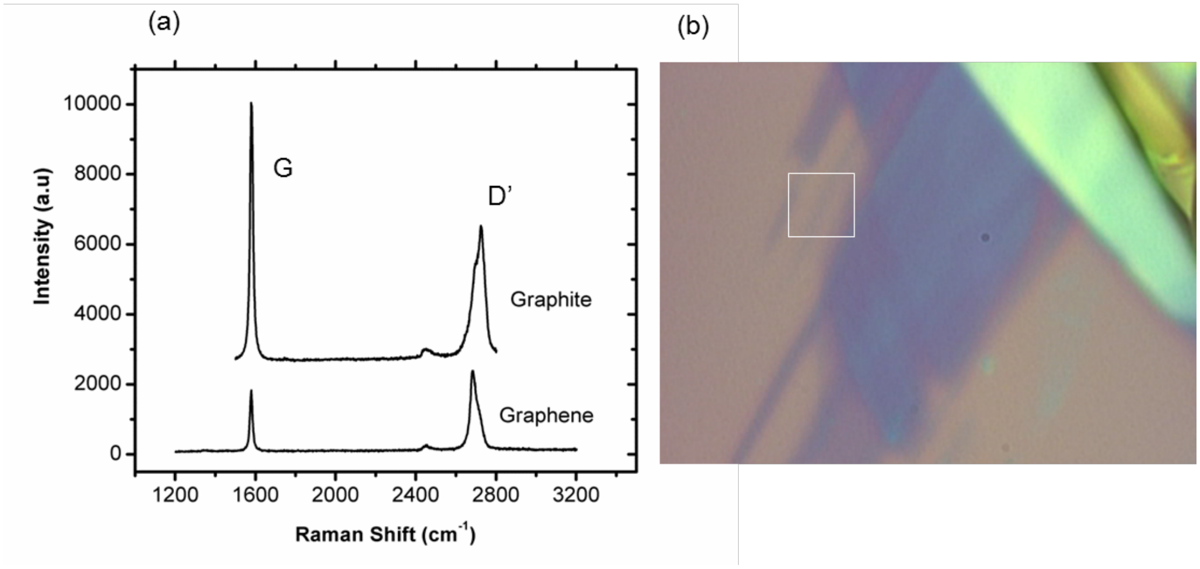

Figure B.1 (a) Raman spectroscopy of bulk graphite and monolayer graphene. (b) Optical microscope image of graphene/graphite films, with the 5 μm region on which Raman was performed containing monolayer graphene indicated by the white square.

The Raman spectrum of graphene is distinguished from that of bulk graphite by two peaks: the D' peak near ~2700 cm^{-1} and the G peak near ~1600 cm^{-1}.[2] In our experiments, the graphene D' peak is substantially red-shifted relative to that of bulk graphite down to 2680 cm^{-1}, which agrees closely with the literature value for monolayer graphene of 2678.8 ± 1.0 cm^{-1}.[2] Note that the D' peak of bilayer graphene is known to consist of curves with peak positions of 2683 ±1.5 cm^{-1} and 2701.8 ± 1.0 cm^{-1}, with thicker films exhibiting further blue-shifting relative to that of monolayer graphene up to the bulk peak position of about 2730 cm^{-1}.[2] Thus, the peak position in our experiments more closely agrees with that of monolayer graphene than that of bilayer or thicker multilayer graphene. In addition, the substantial decrease in intensity of the G peak relative to that of the D' in the graphene film relative to that of graphite appears characteristic of the transition to monolayer graphene from bulk graphite.[2] It should be mentioned that the graphene D' peak appears to possess an asymmetry that is not characteristic of pure monolayer graphene, with a small "bump" appearing above 2700 cm^{-1}. This can be attributed to the fact that the Raman spectroscopy was performed on a 5 μm domain containing also thicker films (as confirmed by AFM), thereby introducing additional blue-shifted peaks into the spectrum.

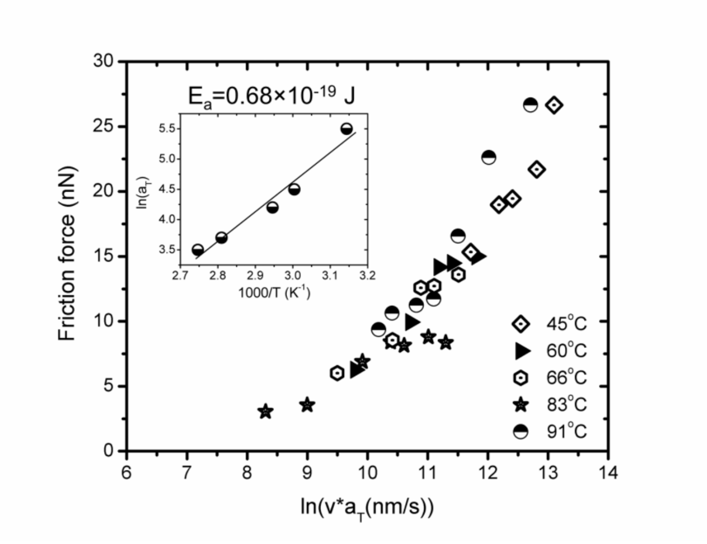

Figure B.2: Friction-velocity master curve of SiO_2 AFM tip on CaF_2. Inset: Arrhenius analysis of thermal shift factors.

IFA on CaF_2

Figure B2 provides the results of IFA on CaF_2, revealing an IFA activation energy 0.68 ± .09 × 10^{-19} J, consistent with the literature value of the Hamaker constant between CaF_2 and SiO_2 of 0.67 × 10^{-19} J.[3] To further confirm the applicability of the Lifshitz theory for comparison to IFA Hamaker constants, we consider the following simplified Lifshitz expression for the non-retarded Hamaker constant A_{12} between two dielectric materials (1,2) across a medium (3), with dielectric constants ε_k, refractive indices n_k , and $\nu_e = 3.5 \times 10^{15}\ \mathrm{s}^{-1}$

$$A_{12} \approx \frac{3}{4}kT\left(\frac{\varepsilon_1-\varepsilon_3}{\varepsilon_1+\varepsilon_3}\right)\left(\frac{\varepsilon_2-\varepsilon_3}{\varepsilon_2+\varepsilon_3}\right)+\frac{3h\upsilon_e}{8\sqrt{2}}\frac{\left(n_1^2-n_3^2\right)\left(n_2^2-n_3^2\right)}{\sqrt{\left(n_1^2+n_3^2\right)}\sqrt{\left(n_2^2+n_3^2\right)}\left\{\sqrt{\left(n_1^2+n_3^2\right)}+\sqrt{\left(n_2^2+n_3^2\right)}\right\}} \qquad \text{B1}$$

Using the dielectric and optical data provided in **Table B1**, the above expression predicts at T= 300 K a non-retarded Hamaker constant for CaF_2 interacting with SiO_2 across air $A_{CaF2\text{-}SiO2}$ of 0.67 × 10^{-19} J, which is in excellent agreement with the IFA value, further confirming the correspondence between IFA Hamaker constants and the Lifshitz theory.

Material	**Dielectric Constants**		**Refractive Indices**	
CaF_2	ε_1	7.4[4]	n_1	1.427[4]
SiO_2	ε_2	3.8[4]	n_2	1.448[4]
Air	ε_3	1[4]	n_3	1[4]

Table B-1: Dielectric and optical data for CaF_2, SiO_2, and air.

Dielectric Model of Graphite

Table B2 provides the fit parameters developed in the literature from optical reflectance and EELS data for the HOPG dielectric functions[5], $\varepsilon_\parallel$ and $\varepsilon_\perp$, described Equation 5.7

Parameter	$\varepsilon_\parallel$	$\varepsilon_\perp$	**Parameter**	$\varepsilon_\parallel$	$\varepsilon_\perp$
α_1	0.505	0.138	Γ_0(eV)	6.365	0.091
α_2	7.079	29.728	Γ_1(eV)	4.102	2.096
α_3	0.362	0.516	Γ_2(eV)	7.328	3.492
α_4	7.426	1.783	Γ_3(eV)	1.414	2.442
α_5	3.823	1.018	Γ_4(eV)	0.046	2.529
α_6	1.387	1.18	Γ_5(eV)	1.862	6.829
α_7	28.963	9.388	Γ_6(eV)	11.922	14.541
Ω_p(eV)	3.195	3.415	Γ_7(eV)	39.091	20.314
$F_1(eV^2)$	53.217	12.274	ω_1(eV)	0.275	11.418
$F_2(eV^2)$	40.824	1.083	ω_2(eV)	3.508	4.095
$F_3(eV^2)$	50.301	28.158	ω_3(eV)	4.451	10.003
$F_4(eV^2)$	3.645	47.291	ω_4(eV)	13.591	14.991
$F_5(eV^2)$	190.998	101.08	ω_5(eV)	14.226	17.516

F_6(eV^2)	335.34	308.65	ω_6(eV)	15.55	30.712
F_7(eV^2)	145.8	350.82	ω_7(eV)	32.011	46.004

Table B-2: Fit parameters for HOPG in plane $\varepsilon_{\|}$ and out of plane $\varepsilon_{\perp}$ dielectric functions.

The fit parameters Γ_j' appearing in Equation 7 are frequency-dependent parameters given as

$$\Gamma_j' = \Gamma_j \exp\left[-\alpha_j\left(\frac{\omega-\omega_j}{\Gamma_j}\right)^2\right] \qquad \text{B2}$$

Calculation of Hamaker Constants from Electron Energy Loss Spectroscopy (EELS) Studies

The following numerical procedure, which has been used elsewhere,[6] was applied to transform the anisotropic electron energy loss (EEL) function, determined by Eberlein *et al.*,[7] to the anisotropic dielectric function for calculation of the Hamaker constant via Equation 5.6 (Chapter 5). First, the frequency ω dependent EEL function is proportional to –Im(ε^{-1}), i.e.

$$EEL(\omega) = (c)(-\operatorname{Im}(\varepsilon^{-1}(\omega))) \qquad \text{B3}$$

where c is a positive normalization constant to be determined. The normalization constant for transforming the loss function to –Im(ε^{-1}) was determined as that which reproduced the known IFA-determined Hamaker constant for HOPG of 2.8×10^{-19} J, i.e. $c = 1.142$. With knowledge of this normalization constant, Im(ε^{-1}) can be determined and subsequently transformed to Re(ε^{-1}) via a Kramers-Kronig relation,

$$\operatorname{Re}(\varepsilon^{-1}(\omega)) = 1 + \frac{2}{\pi} P\int_0^{\infty} \frac{x \operatorname{Im}(\varepsilon^{-1}(\omega))}{x^2-\omega^2}dx \qquad \text{B4}$$

where P denotes the Cauchy principal value of the integral. Knoweledge of the real and imaginary parts of the inverse dielectric function enables the imaginary component of the dielectric function to be computed as

$$\mathrm{Im}(\varepsilon(\omega)) = \frac{-\mathrm{Im}(\varepsilon^{-1}(\omega))}{\mathrm{Re}(\varepsilon^{-1}(\omega))^2 + \mathrm{Im}(\varepsilon^{-1}(\omega))^2} \qquad \text{B5}$$

Finally, the imaginary component of the dielectric function can be transformed to the dielectric function evaluated at imaginary frequencies that appears in Equation 5.6 (Chapter 5),

$$\varepsilon(i\xi) = 1 + \frac{2}{\pi}\int_0^\infty \frac{\omega \mathrm{Im}(\varepsilon(\omega))}{\omega^2 + \xi^2} d\omega \qquad \text{B6}$$

It must be noted that the EEL spectrum generated from TEM experiments at frequencies below 3 eV conceals the material response, due to the presence of a zero loss peak, rendering the loss function in this regime unreliable.[7] Thus, below 3 eV, the dielectric function of graphite was modelled using the empirical fits developed by Djurisic described above, and the in plane dielectric function of graphene was modelled using its established universal optical conductance.[8,9]

References

(1) Novoselov, K. S.; Geim, A. K.; Morozov, S. V.; Jiang, D.; Zhang, Y.; Dubonos, S. V.; Grigorieva, I. V.; Firsov, A. A. *Science* **2004**, *306*.

(2) Graf, D.; Molitor, F.; Ensslin, K.; Stampfer, C.; Jungen, A.; Hierold, C.; Wirtz, L. *Nano Letters* **2007**, *7*, 238-242.

(3) Bergstrom, L. *Advances in Colloid and Interface Science* **1997**, *70*, 125-169.

(4) Israelachvili, J. N. *Intermolecular and Surface Forces*; 3rd ed.; Academic Press, 2011.

(5) Djurisic, A. B.; Li, E. H. *J. Appl. Phys.* **1999**, *85*.

(6) Dagastine, R. R.; Prieve, D. C.; White, L. R. *Journal of Colloid and Interface Science* **2002**, *249*, 78-83.

(7) Eberlein, T.; Bangert, U.; Nair, R. R.; Jones, R.; Gass, M.; Bleloch, A. L.; Novoselov, K. S.; Geim, A.; Briddon, P. R. *Phys. Rev. B* **2008**, *77*, 233406.

(8) Drosdoff, D.; Woods, L. M. *Phys. Rev. A* **2011**, *84*, 062501.

(9) Mak, K. F.; Sfeir, M. Y.; Misewich, J. A.; Heinz, t. F. *PNAS* **2010**, *107*.

Bibliography

1 Azzaroni, O., Brown, A. A. & Huck, W. T. S. UCST wetting transitions of polyzwitterionic brushes driven by self-association. Angewandte Chemie-International Edition 45, 1770-1774 (2006).

2 Baker, R. W. Future directions of membrane gas separation technology. Industrial & Engineering Chemistry Research 41, 1393-1411 (2002).

3 Bansal, A. et al. Quantitative equivalence between polymer nanocomposites and thin polymer films. Nature Materials 4, 693-698 (2005).

4 Baschetti, M. G. et al. Effects on sorption and diffusion in PTMSP and TMSP/TMSE copolymers of free volume changes due to polymer ageing. Journal of Molecular Structure 739, 75-86 (2005).

5 Benight, S. J. et al. Nano-Engineering Lattice Dimensionality for a Soft Matter Organic Functional Material. Advanced Materials 24, 3263-3268 (2012).

6 Bergstrom, L. Hamaker constants of inorganic materials. Advances in Colloid and Interface Science 70, 125-169 (1997).

7 Bernardo, P., Drioli, E. & Golemme, G. Membrane Gas Separation: A Review/State of the Art. Industrial & Engineering Chemistry Research 48, 4638-4663 (2009).

8 Bhargava, R. N., Gallagher, D., Hong, X. & Nurmikko, A. OPTICAL-PROPERTIES OF MANGANESE-DOPED NANOCRYSTALS OF ZNS. Physical Review Letters 72, 416-419 (1994).

9 Binnig, G., Quate, C. F. & Gerber, C. ATOMIC FORCE MICROSCOPE. Physical Review Letters 56, 930-933 (1986).

10 Bondar, V. I., Freeman, B. D. & Pinnau, I. Gas sorption and characterization of poly(ether-b-amide) segmented block copolymers. Journal of Polymer Science Part B-Polymer Physics 37, 2463-2475 (1999).

11 Bondar, V. I., Freeman, B. D. & Pinnau, I. Gas transport properties of poly(ether-b-amide) segmented block copolymers. Journal of Polymer Science Part B-Polymer Physics 38, 2051-2062 (2000).

12 Bos, A., Punt, I. G. M., Wessling, M. & Strathmann, H. Suppression of CO2-plasticization by semiinterpenetrating polymer network formation. Journal of Polymer Science Part B-Polymer Physics 36, 1547-1556 (1998).

13 Brault, N. D. et al. Dry Film Refractive Index as an Important Parameter for Ultra-Low Fouling Surface Coatings. Biomacromolecules 13, 589-593 (2012).

14 Bredas, J. L., Chance, R. R. & Silbey, R. HEAD HEAD INTERACTIONS IN ZWITTERIONIC ASSOCIATING POLYMERS. Macromolecules 21, 1633-1639 (1988).

15 Brunetti, A., Scura, F., Barbieri, G. & Drioli, E. Membrane technologies for CO2 separation. Journal of Membrane Science 359, 115-125.

16 Budd, P. M. et al. Gas separation membranes from polymers of intrinsic microporosity. Journal of Membrane Science 251, 263-269 (2005).

17 Buenviaje, C. et al. Confined flow in polymer films at interfaces. Langmuir 15, 6446-6450 (1999).

18 C. K. Buenviaje, S. R. G., M. H. Rafailovich, and R. M. Overney. in Materials Research Society Symposium Proceedings 187-92 (1998).

19 Callow, J. A. & Callow, M. E. Trends in the development of environmentally friendly fouling-resistant marine coatings. Nature Communications 2 (2011).

20 Campoy-Quiles, M., Sims, M., Etchegoin, P. G. & Bradley, D. D. C. Thickness-dependent thermal transition temperatures in thin conjugated polymer films. Macromolecules 39, 7673-7680 (2006).

21 Chang, Y., Chen, S. F., Zhang, Z. & Jiang, S. Y. Highly protein-resistant coatings from well-defined diblock copolymers containing sulfobetaines. Langmuir 22, 2222-2226 (2006).

22 Chen, S. & Jiang, S. A new avenue to nonfouling materials. Advanced Materials 20, 335-+ (2008).

23 Chen, S. F., Zheng, J., Li, L. Y. & Jiang, S. Y. Strong resistance of phosphorylcholine self-assembled monolayers to protein adsorption: Insights into nonfouling properties of zwitterionic materials. Journal of the American Chemical Society 127, 14473-14478 (2005).

24 Chen, S., Li, L., Zhao, C. & Zheng, J. Surface hydration: Principles and applications toward low-fouling/nonfouling biomaterials. Polymer 51, 5283-5293 (2010).

25 Chen, Y. & Thayumanavan, S. Amphiphilicity in Homopolymer Surfaces Reduces Nonspecific Protein Adsorption. Langmuir 25, 13795-13799 (2009).

26 Cheng, G. et al. Zwitterionic carboxybetaine polymer surfaces and their resistance to long-term biofilm formation. Biomaterials 30, 5234-5240 (2009).

27 Cheng, N., Brown, A. A., Azzaroni, O. & Huck, W. T. S. Thickness-dependent properties of polyzwitterionic brushes. Macromolecules 41, 6317-6321 (2008).

28 Cheon, S. et al. How to optically count graphene layers. Optics Letters 37, 3765 (2012).

29 Chung, T. S., Jiang, L. Y., Li, Y. & Kulprathipanja, S. Mixed matrix membranes (MMMs) comprising organic polymers with dispersed inorganic fillers for gas separation. Progress in Polymer Science 32, 483-507 (2007).

30 Consolati, G., Genco, I., Pegoraro, M. & Zanderighi, L. Positron annihilation lifetime (PAL) in poly 1-(trimethylsilyl)propine (PTMSP): Free volume determination and time dependence of permeability. Journal of Polymer Science Part B-Polymer Physics 34, 357-367 (1996).

31 D.Liu, Z. W., Q.Jiang. Surface Energy and Site Dependent Cohesive Energy of Ag Clusters. Current Nanoscience 7, 463-470 (2011).

32 Dagastine, R. R., Prieve, D. C. & White, L. R. Calculations of van der Waals Fores in 2-Dimensionally anisotropic Materials and Its Application to Carbon Black Journal of Colloid and Interface Science 249, 78-83 (2002).

33 Dagastine, R. R., Prieve, D. C. & White, L. R. Calculations of van der Waals Fores in 2-Dimensionally anisotropic Materials and Its Application to Carbon Black. Journal of Colloid and Interface Science 249, 78-83 (2002).

34 De Sitter, K. et al. Silica filled poly(1-trimethylsilyl-1-propyne) nanocomposite membranes: Relation between the transport of gases and structural characteristics. Journal of Membrane Science 278, 83-91 (2006).

35 De Sitter, K. et al. Silica filled poly(4-methyl-2-pentyne) nanocomposite membranes: Similarities and differences with poly(1-trimethylsilyl-1-propyne)-silica systems. Journal of Membrane Science 321, 284-292 (2008).

36 Djurisic, A. B. & Li, E. H. Optical properties of graphite. J. Appl. Phys. 85, 7404-7410 (1999).

37 Djurisic, A. B. & Li, E. H. Optical properties of grpahite. J. Appl. Phys. 85 (1999).

38 Dong, J., Yao, Z., Yang, T., Jiang, L. & Shen, C. Control of Superhydrophilic and Superhydrophobic Graphene Interface. Scientific Reports 3 (2013).

39 Dorkenoo, K. D. & Pfromm, P. H. Accelerated physical aging of thin poly 1-(trimethylsilyl)-1-propyne films. Macromolecules 33, 3747-3751 (2000).

40 Dressel, M. & Gruner, G. Electrodynamics of solids: optical properties of electrons in matter (Cambridge University Press, Cambridge, UK, 2002).

41 Drosdoff, D. & Woods, L. M. Casimir interactiosn between graphene sheets and metamaterials. Phys. Rev. A 84, 062501 (2011).

42 Du, N. et al. Azide-based Cross-Linking of Polymers of Intrinsic Microporosity (PIMs) for Condensable Gas Separation. Macromolecular Rapid Communications 32, 631-636 (2011).

43 Du, N. et al. Polymers of Intrinsic Microporosity Containing Trifluoromethyl and Phenylsulfone Groups as Materials for Membrane Gas Separation. Macromolecules 41, 9656-9662 (2008).

44 Eberlein, T. et al. Plasmon spectroscopy of free-standing graphene films. Phys. Rev. B 77, 233406 (2008).

45 Feng, X. D. & Jin, Z. X. Spontaneous Formation of Nanoscale Polymer Spheres, Capsules, or Rods by Evaporation of Polymer Solutions in Cylindrical Alumina Nanopores. Macromolecules 42, 569-572 (2009).

46 Ferry, J. D. Viscoelastic Properties of Polymers (John Wiley &Sons, 1980).

47 Filleter, T. et al. Phys. Rev. Lett. 102 (2009).

48 Forrest, J. A. & Dalnoki-Veress, K. The glass transition in thin polymer films. Advances in Colloid and Interface Science 94, 167-196 (2001).

49 Freeman, B. & Pinnau, I. Separation of gases using solubility-selective polymers. Trends in Polymer Science 5, 167-173 (1997).

50 Galin, M., Chapoton, A. & Galin, J. C. DIELECTRIC INCREMENTS, INTERCHARGE DISTANCES AND CONFORMATION OF QUATERNARY AMMONIOALKYLSULFONATES AND ALKOXYDICYANOETHENOLATES IN AQUEOUS AND TRIFLUOROETHANOL SOLUTIONS. Journal of the Chemical Society-Perkin Transactions 2, 545-553 (1993).

51 Ge, S. et al. Shear modulation force microscopy study of near surface glass transition temperatures. Physical Review Letters 85, 2340-2343 (2000).

52 Gould, T., Lebeque, S. & Dobson, J. F. J. Phys.: Condens. Matter 25, 445010 (2013).

53 Graf, D. et al. Spatially Resolved Raman Spectroscopy of Single- and Few-Layer Graphene. Nano Letters 7, 238-242 (2007).

54 Gray, T., Killgore, J., Luo, J. D., Jen, A. K. Y. & Overney, R. M. Molecular mobility and transitions in complex organic systems studied by shear force microscopy. Nanotechnology 18 (2007).

55 Grosch, K. A. REALTION BETWEEN FRICTION AND VISCO-ELASTIC PROPERTIES OF RUBBER. Proceedings of the Royal Society of London Series a-Mathematical and Physical Sciences 274, 21-+ (1963).

56 Gudiksen, M. S., Wang, J. F. & Lieber, C. M. Size-dependent photoluminescence from single indium phosphide nanowires. Journal of Physical Chemistry B 106, 4036-4039 (2002).

57 He, M. Y., Blum, A. S., Overney, G. & Overney, R. M. Effect of interfacial liquid structuring on the coherence length in nanolubrication. Physical Review Letters 88 (2002).

58 He, Y. et al. Molecular simulation studies of protein interactions with zwitterionic phosphorylcholine self-assembled monolayers in the presence of water. Langmuir 24, 10358-10364 (2008).

59 He, Y. et al. Origin of repulsive force and structure/dynamics of interfacial water in OEG-protein interactions: a molecular simulation study. Physical Chemistry Chemical Physics 10, 5539-5544 (2008).

60 He, Z. J., Pinnau, I. & Morisato, A. Nanostructured poly(4-methyl-2-pentyne)/silica hybrid membranes for gas separation. Desalination 146, 11-15 (2002).

61 Hernandez, Y., Lotya, M., Rickard, D., Bergin, S. D. & Coleman, J. N. Measurement of Multicomponent Solubility Parameters for Graphene Facilitates Solvent Discovery. Langmuir 26, 3208-3213 (2009).

62 Hill, A. J., Freeman, B. D., Jaffe, M., Merkel, T. C. & Pinnau, I. Tailoring nanospace. Journal of Molecular Structure 739, 173-178 (2005).

63 Hofmann, D., Fritz, L., Ulbrich, J. & Paul, D. Molecular modelling of amorphous membrane polymers. Polymer 38, 6145-6155 (1997).

64 Horn, N. R. & Paul, D. R. Carbon dioxide plasticization and conditioning effects in thick vs. thin glassy polymer films. Polymer 52, 1619-1627 (2011).

65 Horn, N. R. & Paul, D. R. Carbon dioxide plasticization of thin glassy polymer films. Polymer 52, 5587-5594 (2011).

66 Huang, C. J., Brault, N. D., Li, Y. T., Yu, Q. M. & Jiang, S. Y. Controlled Hierarchical Architecture in Surface-initiated Zwitterionic Polymer Brushes with Structurally Regulated Functionalities. Advanced Materials 24, 1834-1837 (2012).

67 Huang, C. J., Li, Y. T. & Jiang, S. Y. Zwitterionic Polymer-Based Platform with Two-Layer Architecture for Ultra Low Fouling and High Protein Loading. Analytical Chemistry 84, 3440-3445 (2012).

68 Huang, C. J., Li, Y. T., Krause, J. B., Brault, N. D. & Jiang, S. Y. Internal Architecture of Zwitterionic Polymer Brushes Regulates Nonfouling Properties. Macromolecular Rapid Communications 33, 1003-1007 (2012).

69 Huang, C.-w. et al. Layer-dependent morphologies of silver on n-layer graphene. Nanoscale Research Letters 7, 618 (2012).

70 Huang, Y. & Paul, D. R. Physical aging of thin glassy polymer films monitored by gas permeability. Polymer 45, 8377-8393 (2004).

71 Ichiraku, Y., Stern, S. A. & Nakagawa, T. AN INVESTIGATION OF THE HIGH GAS-PERMEABILITY OF POLY (1-TRIMETHYLSILYL-1-PROPYNE). Journal of Membrane Science 34, 5-18 (1987).

72 Israelachvili, J. N. Intermolecular and Surface Forces (Academic Press, 2011).

73 Jia, B. & Zou, L. Wettability and its influence on graphene nanoscheets as electrode material for capacitive deionization. Chemical Physics Letters 548, 23-28 (2012).

74 Jiang, S. & Cao, Z. Ultralow-Fouling, Functionalizable, and Hydrolyzable Zwitterionic Materials and Their Derivatives for Biological Applications. Advanced Materials 22, 920-932 (2010).

75 Jovanovic, V. B., Radovic, I. & Borka, D. High-energy plasmon spectroscopy of freestanding multilayer graphene. Phys. Rev. B 84, 155416 (2011).

76 Jr., D. B. K., Gray, T. O. & Overney, R. M. Intrinsic friction analysis-Novel nanoscopic access to molecular mobility in constrained organic systems. Ultramicroscopy 109, 991-1000 (2009).

77 Jr., D. B. K., Widjaja, P., Acton, O. & Overney, R. M. Molecular dissipation and mode coupling in organic monolayers and polymer films. J. Chem. Phys. 134, 104502 (2011).

78 Kanaya, T. et al. Role of local dynamics in the gas permeability of glassy substituted polyacetylenes. A quasielastic neutron scattering study. Macromolecules 35, 5559-5564 (2002).

79 Kanehashi, S. & Nagai, K. Analysis of dual-mode model parameters for gas sorption in glassy polymers. Journal of Membrane Science 253, 117-138 (2005).

80 Kanehashi, S. et al. Effects of carbon dioxide-induced plasticization on the gas trans-port properties of glassy polyimide membranes. Journal of Membrane Science 298, 147-155 (2007).

81 Keddie, J. L., Jones, R. A. L. & Cory, R. A. Size-Dependent Depression of the Glass-Transition Temperature in Polymer-Films. Europhysics Letters 27, 59-64 (1994).

82 Killgore, J. P. & Overney, R. M. Interfacial mobility and bonding strength in nanocomposite thin film membranes. Langmuir 24, 3446-3451 (2008).

83 Killgore, J. P., Kocherlakota, L. S. & Overney, R. M. Enhanced Mobility and Increased Gas Sorption Capacity in Thin Film and Nanoconduit Confined Polymers. Journal of Polymer Science Part B-Polymer Physics 48, 434-441 (2010).

84 Kim, B. H. et al. Surface Energy Modification by Spin-Cast Large-Area Graphene Film for Block Copolymer Lithography. ACS Nano 4, 5464-5470 (2010).

85 Kim, H., Abdala, A. A. & Macosko, C. W. Graphene/Polymer Nanocomposites. Macromolecules 43, 6515-6530 (2010).

86 Kim, J. H. & Lee, Y. M. Gas permeation properties of poly(amide-6-b-ethylene oxide)-silica hybrid membranes. Journal of Membrane Science 193, 209-225 (2001).

87 Kim, J. H., Ha, S. Y. & Lee, Y. M. Gas permeation of poly(amide-6-b-ethylene oxide) copolymer. Journal of Membrane Science 190, 179-193 (2001).

88 Kimmerle, K., Hofmann, T. & Strathmann, H. ANALYSIS OF GAS PERMEATION THROUGH COMPOSITE MEMBRANES. Journal of Membrane Science 61, 1-17 (1991).

89 Knorr, D. B. et al. Molecular Mobility in Self-Assembled Dendritic Chromophore Glasses. Journal of Physical Chemistry B 113, 14180-14188 (2009).

90 Knorr, D. B., Gray, T. O. & Overney, R. M. Cooperative and submolecular dissipation mechanisms of sliding friction in complex organic systems. Journal of Chemical Physics 129, 074504 (2008).

91 Knorr, D. B., Gray, T. O. & Overney, R. M. Intrinsic friction analysis-Novel nanoscopic access to molecular mobility in constrained organic systems. Ultramicroscopy 109, 991-1000 (2009).

92 Knorr, D. B., Jr., Kocherlakota, L. S. & Overney, R. M. Insight into reverse selectivity and relaxation behavior of poly 1-(trimethylsilyl)-1-propyne by flux-lateral force and intrinsic friction microscopy. Journal of Membrane Science 346, 302-309 (2010).

93 Knorr, D. B., Widjaja, P., Acton, O. & Overney, R. M. Molecular friction dissipation and mode coupling in organic monolayers and polymer films. Journal of Chemical Physics 134 (2011).

94 Kocherlakota, L. S., Knorr, D. B., Jr., Foster, L. & Overney, R. M. Enhanced gas transport properties and molecular mobilities in nano-constrained poly 1-(trimethylsily1)-1-propyne membranes. Polymer 53, 2394-2401 (2012).

95 Kocherlakota, L.S.; B. A. K., and René M. Overney. Local Energetic Analysis of the Surface Energies for Graphene from the Single Layer to Graphite. (Submitted) Advanced Materials Interfaces.

96 Kocherlakota,L.S.; T. P., René M. Overney. Transport and stability enhancement in interfacially and dimensionally constrained CO2 selective polymers embedded in nanoporous sieve membranes. Polymer 54, 5986-5992 (2013).

97 Koros, W. J. & Paul, D. R. CO2 SORPTION IN POLY(ETHYLENE-TEREPHTHALATE) ABOVE AND BELOW GLASS-TRANSITION. Journal of Polymer Science Part B-Polymer Physics 16, 1947-1963 (1978).

98 Koros, W. J., Chan, A. H. & Paul, D. R. SORPTION AND TRANSPORT OF VARIOUS GASES IN POLYCARBONATE. Journal of Membrane Science 2, 165-190 (1977).

99 Krishnan, S., Weinman, C. J. & Ober, C. K. Advances in polymers for anti-biofouling surfaces. Journal of Materials Chemistry 18, 3405-3413 (2008).

100 Ku, A. Y., Ruud, J. A., Early, T. A. & Corderman, R. R. Evidence of ion transport through surface conduction in alkylsilane-functionalized nanoporous ceramic membranes. Langmuir 22, 8277-8280 (2006).

101 Kuilla, T. et al. Recent advances in graphene based polymer composites. Progress in Polymer Science 35, 1350-1375 (2010).

102 Ladenheim, H. & Morawetz, H. A NEW TYPE OF POLYAMPHOLYTE - POLY(4-VINYL PYRIDINE BETAINE). Journal of Polymer Science 26, 251-254 (1957).

103 Lam, K. T. & Liang, G. C. An ab initio study on energy gap of bilayer graphene nanoribbons with armchair edges. Applied Physics Letters 92 (2008).

104 Langer, R. Perspectives: Drug delivery - Drugs on target. Science 293, 58-59 (2001).

105 Lau, C. H., Li, P., Li, F. Y., Chung, T. S. & Paul, D. R. Reverse-selective polymeric membranes for gas separations. Progress in Polymer Science 38, 740-766 (2013).

106 Law, M., Goldberger, J. & Yang, P. D. Semiconductor nanowires and nanotubes. Annual Review of Materials Research 34, 83-122 (2004).

107 Lee, W. H. et al. Surface-Directed Molecular Assembly of Pentacene on Monolayer Graphene for High-Performance Organic Transistors. J. Am. Chem. Soc. 133, 4447-4454 (2011).

108 Li, L. Y., Chen, S. F., Zheng, J., Ratner, B. D. & Jiang, S. Y. Protein adsorption on oligo(ethylene glycol)-terminated alkanethiolate self-assembled monolayers: The molecular basis for nonfouling behavior. Journal of Physical Chemistry B 109, 2934-2941 (2005).

109 Li, Q., Lee, C., Carpick, R. W. & Hone, J. Phys. Status Solidi B 247, 086102 (2009).

110 Li, Z. et al. Effects of airborne contaminants on the wettability of supported graphene and graphite. Nature Materials 12, 925 (2013).

111 Lima, M. P., Fazzio, A. & da Silva, A. J. R. Edge effects in bilayer graphene nanoribbons: Ab initio total-energy density functional theory calculations. Physical Review B 79 (2009).

112 Lin, H. & Freeman, B. D. Gas solubility, diffusivity and permeability in poly(ethylene oxide). Journal of Membrane Science 239, 105-117 (2004).

113 Lin, H. Q. & Freeman, B. D. Materials selection guidelines for membranes that remove CO2 from gas mixtures. Journal of Molecular Structure 739, 57-74 (2005).

114 Lin, Y., Ehlert, G. J., Bukowsky, C. & Sodano, H. A. Superhydrophobic Functionalized Graphene Aerogels. ACS Appl. Mater. Interfaces 3, 2200-2203 (2011).

115 Lipkin, D. M., Israelachvili, J. N. & Clarke, D. R. Estimating the metal-ceramic van der Waals adhesion energy. Philosophical Magazine a-Physics of Condensed Matter Structure Defects and Mechanical Properties 76, 715-728 (1997).

116 Liu, X., Yang, J. W. & Lynn, D. M. Addition of "Charge-Shifting" side chains to linear poly(ethyleneimine) enhances cell transfection efficiency. Biomacromolecules 9, 2063-2071 (2008).

117 Lutz, J. F. & Hoth, A. Preparation of ideal PEG analogues with a tunable thermosensitivity by controlled radical copolymerization of 2-(2-methoxyethoxy)ethyl methacrylate and oligo(ethylene glycol) methacrylate. Macromolecules 39, 893-896 (2006).

118 Ma, H. W., Li, D. J., Sheng, X., Zhao, B. & Chilkoti, A. Protein-resistant polymer coatings on silicon oxide by surface-initiated atom transfer radical polymerization. Langmuir 22, 3751-3756 (2006).

119 Maiz, J., Martin, J. & Mijangos, C. Confinement Effects on the Crystallization of Poly(ethylene oxide) Nanotubes. Langmuir 28, 12296-12303 (2012).

120 Mak, K. F., Sfeir, M. Y., Misewich, J. A. & Heinz, t. F. The evolution of electronic structure in few-layer graphene revealed by optical spectroscopy. PNAS 107 (2010).

121 Martin, J. & Mijangos, C. Tailored Polymer-Based Nanofibers and Nanotubes by Means of Different Infiltration Methods into Alumina Nanopores. Langmuir 25, 1181-1187 (2009).

122 Masuda, T., Isobe, E., Higashimura, T. & Takada, K. Poly 1-(Trimethylsilyl)-1-Propyne - a New High Polymer Synthesized with Transition-Metal Catalysts and Characterized by Extremely High Gas-Permeability. Journal of the American Chemical Society 105, 7473-7474 (1983).

123 Matteucci, S., Kusuma, V. A., Kelman, S. D. & Freeman, B. D. Gas transport properties of MgO filled poly (1-trimethylsilyl-1-propyne) nanocomposites. Polymer 49, 1659-1675 (2008).

124 Matteucci, S., Kusuma, V. A., Sanders, D., Swinnea, S. & Freeman, B. D. Gas transport in TiO2 nanoparticle-filled poly (1-trimethylsilyl-1-propyne). Journal of Membrane Science 307, 196-217 (2008).

125 McPherson, T., Kidane, A., Szleifer, I. & Park, K. Prevention of protein adsorption by tethered poly(ethylene oxide) layers: Experiments and single-chain mean-field analysis. Langmuir 14, 176-186 (1998).

126 Medasani, B., Park, Y. H. & Vasiliev, I. Theoretical study of the surface energy, stress, and lattice contraction of silver nanoparticles. Physical Review B 75 (2007).

127 Merkel, T. C. et al. Effect of nanoparticles on gas sorption and transport in poly(1-trimethylsilyl-1-propyne). Macromolecules 36, 6844-6855 (2003).

128 Merkel, T. C. et al. Ultrapermeable, reverse-selective nanocomposite membranes. Science 296, 519-522 (2002).

129 Merkel, T. C., Bondar, V., Nagai, K. & Freeman, B. D. Sorption and transport of hydrocarbon and perfluorocarbon gases in poly(1-trimethylsilyl-1-propyne). Journal of Polymer Science Part B-Polymer Physics 38, 273-296 (2000).

130 Michell, R. M., Blaszczyk-Lezak, I., Mijangos, C. & Muller, A. J. Confinement effects on polymer crystallization: From droplets to alumina nanopores. Polymer 54, 4059-4077 (2013).

131 Morisato, A. et al. Polymer characterization and gas permeability of poly(1-trimethylsilyl-1-propyne) PTMSP , poly(1-phenyl-1-propyne) PPP , and PTMSP/PPP blends. Journal of Polymer Science Part B-Polymer Physics 34, 2209-2222 (1996).

132 Nagai, K., Masuda, T., Nakagawa, T., Freeman, B. D. & Pinnau, I. Poly 1-(trimethylsilyl)-1-propyne and related polymers: synthesis, properties and functions. Progress in Polymer Science 26, 721-798 (2001).

133 Novoselov, K. S. et al. Electric Field Effect in Atomically Thin Carbon Films. Science 306 (2004).

134 Novoselov, K. S. et al. Two-dimensional atomic crystals. PNAS 102, 10451-10453 (2005).

135 Okamoto, K. et al. Gas Permeation Properties of Poly(Ether Imide) Segmented Copolymers. Macromolecules 28, 6950-6956 (1995).

136 Overney, R. M., Buenviaje, C., Luginbuhl, R. & Dinelli, F. Glass and structural transitions measured at polymer surfaces on the nanoscale. Journal of Thermal Analysis and Calorimetry 59, 205-225 (2000).

137 Overney, R. M., L. Guo, H. Totsuka, M. Rafailovich, J. Sokolov, and S. A. & Schwarz, S. A. Interfacially confined polymeric systems studied by atomic force microscopy. Material Research Society (1997).

138 Park, H., Rowehl, J. A., Kim, K. K., Bulovic, V. & Kong, J. Doped graphene electrodes for organic solar cells. Nanotechnology 21, 505204 (2010).

139 Parsegian, V. A. Van der Waals Forces (Cambridge University Press, 2006).

140 Pinnau, I. & Toy, L. G. Transport of organic vapors through poly(1-trimethylsilyl-1-propyne). Journal of Membrane Science 116, 199-209 (1996).

141 Pinnau, I., Wijmans, J. G., Blume, I., Kuroda, T. & Peinemann, K. V. GAS PERMEATION THROUGH COMPOSITE MEMBRANES. Journal of Membrane Science 37, 81-88 (1988).

142 Prime, K. L. & Whitesides, G. M. SELF-ASSEMBLED ORGANIC MONOLAYERS - MODEL SYSTEMS FOR STUDYING ADSORPTION OF PROTEINS AT SURFACES. Science 252, 1164-1167 (1991).

143 Puzder, A., Williamson, A. J., Reboredo, F. A. & Galli, G. Structural stability and optical properties of nanomaterials with reconstructed surfaces. Physical Review Letters 91 (2003).

144 Q. Jiang, L. H. L., and D. S. Zhao. Lattice Contraction and Surface Stress of fcc Nanocrystals. The Journal of Physical Chemistry B 105, 6275-6277 (2001).

145 R. M. Overney, H. T., M. Fujihira, W. Paulus, and H. Ringsdorf. Physical Review Letters 72, 3546 (1994).

146 Rafiee, J., Rafiee, M. A., Yu, Z.-Z. & Koratkar, N. Superhydrophobic to Superhydrophilic Wetting Control in Graphene Films. Adv. Mater. 22, 2151-2154 (2010).

147 Ramanathan, T. et al. Functionalized graphene sheets for polymer nanocomposites. Nature Nanotechnology 327-331 (2008).

148 Ratner, B. D. & Bryant, S. J. Biomaterials: Where we have been and where we are going. Annual Review of Biomedical Engineering 6, 41-75 (2004).

149 Reimann, S. M. & Manninen, M. Electronic structure of quantum dots. Reviews of Modern Physics 74, 1283-1342 (2002).

150 Robeson, L. M. The upper bound revisited. Journal of Membrane Science 320, 390-400 (2008).

151 Rowe, B. W., Freeman, B. D. & Paul, D. R. Physical aging of ultrathin glassy polymer films tracked by gas permeability. Polymer 50, 5565-5575 (2009).

152 Savoca, A. C., Surnamer, A. D. & Tien, C. F. Gas-Transport in Poly(Silylpropynes) - the Chemical-Structure Point-of-View. Macromolecules 26, 6211-6216 (1993).

153 Schulz, D. N. et al. PHASE-BEHAVIOR AND SOLUTION PROPERTIES OF SULFOBETAINE POLYMERS. Polymer 27, 1734-1742 (1986).

154 Sen, S. et al. Equivalence between polymer nanocomposites and thin polymer films: Effect of processing conditions and molecular origins of observed behavior. European Physical Journal-Special Topics 141, 161-165 (2007).

155 Shao, L., Low, B. T., Chung, T. S. & Greenberg, A. R. Polymeric membranes for the hydrogen economy: Contemporary approaches and prospects for the future. Journal of Membrane Science 327, 18-31 (2009).

156 Shenfu Chen , L. L., Chao Zhao , Jie Zheng. Surface hydration: Principles and applications toward low-fouling/nonfouling biomaterials. Polymer 51, 5283-5293 (2010).

157 Shin, K. et al. Enhanced mobility of confined polymers. Nature Materials 6, 961-965 (2007).

158 Shin, Y. J. et al. Surface-Energy Engineering of Graphene. Langmuir 26, 3798-3802 (2010).

159 Shuttleworth, R. THE SURFACE TENSION OF SOLIDS. Proceedings of the Physical Society of London Section A 63, 444-457 (1950).

160 Sills, S. & Overney, R. M. Creeping Friction Dynamics and Molecular Dissipation Mechanisms in Glass Polymers. Phys. Rev. Lett. 91, 095501 (2003).

161 Sills, S. & Overney, R. M. Creeping friction dynamics and molecular dissipation mechanisms in glassy polymers. Physical Review Letters 91 (2003).

162 Sills, S. et al. Interfacial glass transition profiles in ultrathin, spin cast polymer films. Journal of Chemical Physics 120, 5334-5338 (2004).

163 Sills, S., Gray, T. & Overney, R. M. Molecular dissipation phenomena of nanoscopic friction in the heterogeneous relaxation regime of a glass former. Journal of Chemical Physics 123 (2005).

164 Singh, V. et al. Graphene based materials: Past, present, and future. Progress in Materials Science 56, 1178-1271 (2011).

165 Smith, A. M. & Nie, S. M. Semiconductor Nanocrystals: Structure, Properties, and Band Gap Engineering. Accounts of Chemical Research 43, 190-200 (2010).

166 Srinivasan, R., Auvil, S. R. & Burban, P. M. Elucidating the Mechanism(S) of Gas-Transport in Poly 1-(Trimethylsilyl)-1-Propyne (Ptmsp) Membranes. Journal of Membrane Science 86, 67-86 (1994).

167 Steinhart, M. et al. Polymer nanotubes by wetting of ordered porous templates. Science 296, 1997-1997 (2002).

168 Taherian, F., Marcon, V., van der Vegt, N. F. A. & Leroy, F. What Is the Contact Angle of Water on Graphene? Langmuir 29, 1457-1465 (2013).

169 Tasker, P. W. The stability of ionic crystal surfaces. J. Phys. C 12, 4977-4984 (1979).

170 Tsai, W. B., Grunkemeier, J. M. & Horbett, T. A. Human plasma fibrinogen adsorption and platelet adhesion to polystyrene. Journal of Biomedical Materials Research 44, 130-139 (1999).

171 van der Lee, A., Hamon, L., Holl, Y. & Grohens, Y. Density profiles in thin PMMA supported films investigated by X-ray reflectometry. Langmuir 17, 7664-7669 (2001).

172 Vermaak, J. S., Mays, C. W. & Kuhlmann.D. ON SURFACE STRESS AND SURFACE TENSION .I. THEORETICAL CONSIDERATIONS. Surface Science 12, 128-& (1968).

173 Wang, S. R., Zhang, Y., Abidi, N. & Cabrales, L. Wettability and Surface Free Energy of Graphene Films. Langmuir 25, 11078-11081 (2009).

174 Wang, Y., Tong, S. W., Xu, X. F., Oxyilmax, B. & Loh, K. P. Interface Engineering of Layer-by-Layer Stacked Graphene Anodes for High-Performance Organic Solar Cells. Adv. Mater. 23, 1514-1518 (2011).

175 Ward, I. M. Mechanical Properties of Solid Polymers (Wiley-Interscience, London, 1971).

176 Wei, J. H., He, M. Y. & Overney, R. M. Direct measurement of nanofluxes and structural relaxations of perfluorinated ionomer membranes by scanning probe microscopy. Journal of Membrane Science 279, 608-614 (2006).

177 Wijmans, J. G. & Baker, R. W. The Solution-Diffusion Model - a Review. Journal of Membrane Science 107, 1-21 (1995).

178 Winberg, P. et al. Free volume and interstitial mesopores in silica filled poly(I-trimethylsilyl-l-propyne) nanocomposites. Macromolecules 38, 3776-3782 (2005).

179 Xia, J. Z., Chung, T. S., Li, P., Horn, N. R. & Paul, D. R. Aging and carbon dioxide plasticization of thin polyetherimide films. Polymer 53, 2099-2108 (2012).

180 Yang, W. et al. Film thickness dependence of protein adsorption from blood serum and plasma onto poly(sulfobetaine)-grafted surfaces. Langmuir 24, 9211-9214 (2008).

181 Yang, W., Xue, H., Li, W., Zhang, J. & Jiang, S. Pursuing "Zero" Protein Adsorption of Poly(carboxybetaine) from Undiluted Blood Serum and Plasma. Langmuir 25, 11911-11916 (2009).

182 Yang, W., Zhang, L., Wang, S., White, A. D. & Jiang, S. Functionalizable and ultra stable nanoparticles coated with zwitterionic poly(carboxybetaine) in undiluted blood serum. Biomaterials 30, 5617-5621 (2009).

183 Yave, W., Car, A., Funari, S. S., Nunes, S. P. & Peinemann, K. V. CO2-Philic Polymer Membrane with Extremely High Separation Performance. Macromolecules 43, 326-333 (2010).

184 Yave, W., Car, A., Wind, J. & Peinemann, K. V. Nanometric thin film membranes manufactured on square meter scale: ultra-thin films for CO2 capture. Nanotechnology 21 (2010).

185 Yu, H., Li, J. B., Loomis, R. A., Wang, L. W. & Buhro, W. E. Two- versus three-dimensional quantum confinement in indium phosphide wires and dots. Nature Materials 2, 517-520 (2003).

186 Yuan, L. et al. Self-Cleaning Flexible Infrared Nanosensor Based on Carbon Nanoparticles. ACS Nano 5, 4007-4013 (2011).

187 Zhang, M. F. et al. Wetting transition in cylindrical alumina nanopores with polymer melts. Nano Letters 6, 1075-1079 (2006).

188 Zhang, X. J., Shetty, A. S. & Jenekhe, S. A. Electroluminescence and photophysical properties of polyquinolines. Macromolecules 32, 7422-7429 (1999).

189 Zhang, X., Wan, S., Pu, J., Wang, L. & Liu, X. Highly hydrophobic and adhesive performance of graphene films. J. Mater. Chem. 21, 12251-12258 (2011).

190 Zhang, Y.-L., Chen, Q.-D., Jin, Z., Kim, E. & Sum, H.-B. Biomimetic graphene films and their properties. Nanoscale 4, 4858 (2012).

191 Zhang, Z., Chen, S. F., Chang, Y. & Jiang, S. Y. Surface grafted sulfobetaine polymers via atom transfer radical polymerization as superlow fouling coatings. Journal of Physical Chemistry B 110, 10799-10804 (2006).

192 Zheng, J. et al. Strong repulsive forces between protein and oligo (ethylene glycol) self-assembled monolayers: A molecular simulation study. Biophysical Journal 89, 158-166 (2005).

193 Zheng, J., Li, L. Y., Chen, S. F. & Jiang, S. Y. Molecular simulation study of water interactions with oligo (ethylene glycol)-terminated alkanethiol self-assembled monolayers. Langmuir 20, 8931-8938 (2004).

194 Zhou, H. et al. Thickness-Dependent Morphologies of Gold on N-Layer Graphene. J. Am. Chem. Soc. 132, 944-946 (2010).